

X-RAY DIFFRACTION STUDIES OF GaN AND InGaN
SEMICONDUCTOR HETEROSTRUCTURES

By

FRITZ FEDLER

Vordiplom

Universität Hannover

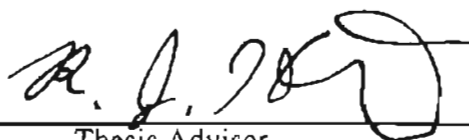
Hannover, Germany

1995

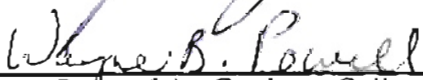
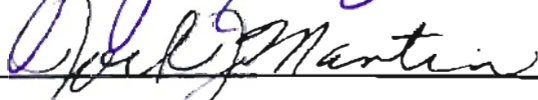
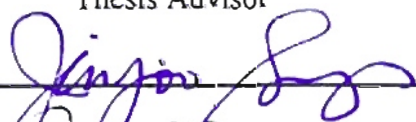
Submitted to the Faculty of the
Graduate College of the
Oklahoma State University
in partial fulfillment of
the requirements for
the Degree of
MASTER OF SCIENCE
December, 1998

X-RAY DIFFRACTION STUDIES OF GaN AND InGaN
SEMICONDUCTOR HETEROSTRUCTURES

Thesis Approved:



Thesis Advisor



Dean of the Graduate College

ACKNOWLEDGMENTS

In August 1996 I started my career as a graduate student in physics at the Oklahoma State University. Little did I know about what to expect from a new school in a different country. America was one great personal experiment about to begin. Soon I was welcomed by new friends, and the burden of the unknown loosened. Finally, I started to feel at home. I have to thank all the people I met here in Stillwater, especially those who became close friends, for providing a friendly atmosphere, and a spirited working environment that made it possible for me to produce this thesis.

My special thanks and appreciation goes to my advisor Dr. R. J. Hauenstein for guiding me through one and a half years of my University career. He showed me a direction I could follow without ever holding me back or pushing me where I would not want to go. His insight in the principles of physics is marvelous. I have profited a lot from his knowledge.

A very special thank you is reserved for my co-worker and friend M. L. O'Steen. I build upon his work, and could always count on his support, no matter how trivial the cause. He helped to translate this thesis from "Germenglish" to the final English version. This was no small effort.

On a professional level I have to thank again Dr. R. J. Hauenstein for his advising me, and M. L. O'Steen for his support. Next, Dr. Y. H. Cho deserves my special appreciation for his providing all MOCVD-grown samples I had the luck to be able to investigate. His insight in semiconductor structures helped me create a bigger picture, leaving the confined view defined by my experiment. People involved in the growth of the samples I studied are Dr. R. J. Hauenstein and M. L. O'Steen (MBE samples) at Oklahoma State University, Drs. S. Keller, U. K. Mishra, and S. P. DenBaars (MOCVD MQW-samples) at University of California Santa Barbara, and Dr. Z. C. Feng (MOCVD InGaN-samples) at Emcore Corporation. Prof. M. Johnson at Oklahoma University

took AFM pictures of one of the MBE samples. I have to thank all of the above for their engagement in semiconductor physics, which has made this thesis possible.

I thank Drs. R. J. Hauenstein, J. J. Song, and J. J. Martin for serving as members of my thesis committee and their investment of time and effort. The prospect of them reading this document was an inspiration for me, and helped me to grasp my own words with a different frame of mind.

Als letztes möchte ich mich bei meinen Eltern Fritz und Anita Fedler sowie meinem Bruder Claas bedanken für ihre vorbehaltlose Unterstützung meiner Ziele. Ich bedanke mich für unseren gemeinsamen Familienzusammenhalt, der auch über den trennenden Atlantik hinweg immer für mich zu spüren war.

Fritz Fedler

Stillwater, Oklahoma

September 1998

TABLE OF CONTENTS

Chapter	Page
1. INTRODUCTION	1
1.1. TECHNICAL AND SCIENTIFIC INTEREST IN GaN	1
1.1.1. CURRENT INTEREST	2
1.1.2. MATERIAL PROPERTIES	3
1.1.3. HISTORY OF NITRIDE RESEARCH	3
1.2. CONTRIBUTION OF THIS THESIS	4
1.3. ORGANIZATION OF THIS THESIS	5
2. THEORY OF X-RAY DIFFRACTION FROM CRYSTALS	7
2.1. OVERVIEW	7
2.2. PHYSICAL ORIGIN OF DIFFRACTION	9
2.3. KINEMATICAL THEORY	12
2.3.1. VON LAUE SCATTERING GEOMETRY	12
2.3.2. RECIPROCAL SPACE	13
2.3.3. DERIVATION OF BRAGG'S EQUATION	18
2.3.4. RELATIVE DIFFRACTED INTENSITY	18
2.4. DYNAMICAL THEORY	23
2.5. STRESS AND STRAIN	27
2.6. SUPERLATTICE ANALYSIS	30
2.6.1. QUALITATIVE VIEW	30
2.6.2. PEAK POSITIONS	31
2.6.3. PEAK WIDTH AND INTENSITY	34
2.7. COMPARISON OF KINEMATICAL AND DY- NAMICAL SIMULATION	37
2.8. SUMMARY	40
3. DESCRIPTION OF THE EXPERIMENTAL HRXRD SETUP	43
3.1. OVERVIEW	43
3.2. THE PHILIPS MRD SYSTEM	45
3.2.1. DEGREES OF FREEDOM	46
3.2.2. MRD OPTICS	49
3.3. THE EWALD CONSTRUCTION	52

Chapter	Page
3.4. BASIC SCAN TYPES	54
3.4.1. ω -SCAN	56
3.4.2. $\omega/2\theta$ -SCAN	58
3.4.3. ϕ -SCAN	59
3.5. RECIPROCAL SPACE MAPS	61
3.5.1. SINGLE LAYER RECIPROCAL SPACE MAP	61
3.5.2. SUPERLATTICE RECIPROCAL SPACE MAP	63
3.6. SUMMARY	67
4. HRXRD APPLIED TO THE STUDY OF GaN-BASED HET- EROSTRUCTURES	68
4.1. OVERVIEW	68
4.2. MBE-GROWN GaN ON Al ₂ O ₃	70
4.2.1. MBE GROWTH PROCESS	72
4.2.2. ROCKING CURVES	73
4.2.3. RECIPROCAL SPACE MAPS	74
4.2.4. GENERAL FINDINGS	76
4.2.5. SPECIFIC FINDINGS	78
4.3. MBE-GROWN GaN ON ZnO	83
4.3.1. GENERAL FINDINGS	83
4.3.2. SPECIFIC FINDINGS	85
4.4. MOCVD-GROWN InGaN ON Al ₂ O ₃	87
4.4.1. MOCVD-GROWTH PROCESS	89
4.4.2. GENERAL FINDINGS	89
4.5. MOCVD-GROWN GaN/InGaN SUPERLATTICES	91
4.5.1. Si-DOPING	92
4.5.2. KINEMATICAL SIMULATION	94
4.5.3. RECIPROCAL SPACE MAPS	96
4.6. MBE-GROWN GaN/InGaN SUPERLATTICES	98
4.6.1. GENERAL FINDINGS	99
4.6.2. SPECIFIC FINDINGS	101
4.7. SUMMARY	104
5. SUMMARY AND CONCLUSION	106
5.1. SUMMARY	106
5.2. CONCLUSION	109
BIBLIOGRAPHY	110

Chapter	Page
APPENDICES	114
APPENDIX A - HRXRD SIMULATION MANUAL	115
A.1. INTRODUCTION	115
A.1.1. ACKNOWLEDGMENTS	115
A.1.2. INTRODUCTION	115
A.1.3. WHAT THIS PROGRAM CAN DO	116
A.2. PROGRAM DETAILS	118
A.2.1. INSTALLATION	118
A.2.2. DATA FILES	118
A.2.2.1. THE 'INDATA' DIRECTORY	118
A.2.2.2. THE 'OUTDATA' DIRECTORY	122
A.2.2.3. THE 'XRDCANS' DIRECTORY	123
A.2.2.4. THE 'XVGR' DIRECTORY	123
A.3. USING THE X-WINDOWS INTERFACE	124
A.3.1. INTRODUCTION	124
A.3.2. MAIN MENU	124
A.3.2.1. CREATE NEW SAMPLE	124
A.3.2.2. ALTER SAMPLE	125
A.3.2.3. NEW MATERIAL ENTRY	125
A.3.2.4. SET SCAN PARAMETERS	125
A.3.2.5. LOOK AT SCANS	126
A.4. HRXRD SIMULATION PROGRAM CODE	128
A.4.1. MAIN CODE FILE	128
A.4.2. SCAN SETUP CODE	131
A.4.3. SIMULATION COMPUTATION CODE	142
APPENDIX B - SUPERLATTICE ANALYZER	157
B.1. USAGE DESCRIPTION	157
B.1.1. MANUAL PAGE	157
B.1.2. SYNOPSIS	157
B.1.3. DESCRIPTION	157
B.1.4. OPTIONS	158
B.1.5. REMARKS	159
B.2. SUPERLATTICE ANALYZER CODE	160
APPENDIX C - XRD SAMPLE CHARACTERIZATION PROCEDURE	184
C.1. INTRODUCTION	184
C.2. PREPARATION	185
C.2.1. START OF THE PHILIPS MRD SYSTEM	185
C.2.2. SHUT DOWN THE PHILIPS MRD SYSTEM	186
C.2.3. SAMPLE MOUNTING	187
C.3. SCANNING	188
C.3.1. BEAM ADJUSTMENT	188
C.3.2. FINDING THE PEAK	189
C.3.3. OPTIMIZING THE SIGNAL	190
C.3.3.1. BASIC OPTIMIZATION	190
C.3.3.2. OPTIMIZE FOR ABSOLUTE ANGLES	191

Chapter		Page
	C.3.4. BASIC SAMPLE CHARACTERIZATION SCANS	191
	C.3.4.1. WAFER MAP	191
	C.3.4.2. ω and $\omega/2\theta$ SCANS	192
	C.3.5. RECIPROCAL SPACE MAPS	192
	C.3.6. TILT MEASUREMENT	193
C.4.	PROCESSING SCAN DATA	194
	C.4.1. TWO DIMENSIONAL DATA	194
	C.4.2. THREE DIMENSIONAL DATA	194

LIST OF TABLES

Table	Page
2.1. Sample Data Used for Simulation Comparison	38
4.1. Sample Overview	71

LIST OF FIGURES

Figure	Page
2.1. Bragg Scattering Geometry	8
2.2. Effects Caused by X-Rays in a Crystal	10
2.3. Electronic Scattering Geometry	14
2.4. von Laue Scattering Geometry	15
2.5. Hexagonal Unit Cell	17
2.6. Atomic Form Factors for Ga, In, Al, and N	20
2.7. Bragg Scattering Geometry (Asymmetrical)	25
2.8. Stress and Strain	28
2.9. Superlattice Analysis: Peak-Order Linear Fit	33
2.10. Wurtzite and Zinc-Blende Lattice Structures	39
2.11. Comparison between Dynamical and Kinematical Simulations	41
3.1. Principal Experimental X-Ray Diffraction Geometries	44
3.2. Philips MRD Waferstage	47
3.3. Waferstage Degrees of Freedom	48
3.4. MRD Optics	51
3.5. Ewald Sphere and Instrumental Scan Limits	53
3.6. Reciprocal Space Sample Volume	55
3.7. ω and $\omega/2\theta$ Scan in Real Space	57
3.8. ω and $\omega/2\theta$ Scan in Reciprocal Space	60

Figure	Page
3.9. Reciprocal Space Map Scan	62
3.10. Strain in Reciprocal Space	64
3.11. Superlattice in Reciprocal Space	66
4.1. Structure of Samples Studied	69
4.2. GaN Rocking Curve	75
4.3. Reciprocal Space Maps of GaN Samples	77
4.4. Examples for Rocking Curve Correlation	79
4.5. AFM Micrograph of GaN Buffer Layer	82
4.6. GaN on ZnO Tilt Measurement	86
4.7. Single Layer Tilt	88
4.8. MOCVD-Grown Single InGa _N Thin Films	90
4.9. MOCVD Superlattice Dependence on Si Doping	93
4.10. MOCVD Superlattice $\omega/2\theta$ -Scan and Kinematical Simulation	95
4.11. MOCVD Superlattice Reciprocal Space Map	97
4.12. MBE Grown Superlattices	100
4.13. Superlattice Growth Analysis	102
A.1. HRXRD Simulation Startup Window	117
A.2. An example for a simulation presentation with xvgr	127

CHAPTER 1

INTRODUCTION

1.1 TECHNICAL AND SCIENTIFIC INTEREST IN GaN

The electronics revolution began with the invention of the transistor by J. Bardeen, W. Brattain and W. Shockley in 1947.¹ This Nobel-Prize-winning invention arguably has had a profound and transforming impact on our every-day lives, as reflected in the countless items of technology—cellular phones, wrist watches, computers, traffic lights, faxes, photocopiers, televisions, and even “smarter” washing machines and automobiles: the list is endless!—which we routinely take for granted. Indeed, had it not been for the advent of the transistor, and the electronics revolution which it spawned, our very way of life at the end of the 20th century would be difficult to imagine.

Technological advancement in the field of electronics is a never-ending process. The interplay between science and technology plays a crucial role in support of these improvements. The scientific community always looks for novel devices, new structures that might be put to use, and new materials with which to produce these new structures. The age of the transistor and its revolutionary applications have generated a growing interest in intensive semiconductor research. The search for the ideal semiconductor tailored to certain applications is far from over.

Today transistors are largely Si-based devices. Other semiconductor devices, such as light-emitting diodes (LED), laser diodes (LD), and electromagnetic radiation detectors, require different material properties. LEDs emitting in the visible range are made from AlGaAs (red), GaP (green), and SiC (blue). The efficiency of red diodes, about 15 %, yields a good brightness for the emitted light.² The conventional GaP and SiC solutions for green and blue light on the other hand, only yield efficiencies between 0.1 % and 0.2 %.² It is in this range of the visible spectrum, and up to the lower ultra

violet (UV) spectrum, where nitrides recommend themselves as a new resource for powerful light emitting structures. At this time, blue nitride-based LEDs are commercially available, and an increasing number of blue LDs are reported in several laboratories.³

1.1.1 CURRENT INTEREST

The interest in nitride semiconductor materials is fueled by the prospect of commercially viable products, which are sought for by the electronics industry. LEDs and LDs in the upper visible range and the UV spectrum are within reach of general commercial exploitation in full color displays (use of LEDs) and readout of high density optical storage media (use of short wavelength LDs).

InN, AlN, and GaN are direct band gap materials, which form a complete series of ternary alloys. The energy gaps of 1.9 eV (InN), 3.4 eV (GaN), and 6.2 eV (AlN) make it possible to span the entire visible spectrum and even extend well into the UV range with various alloy compositions of the three materials.² The emitted wavelengths of nitride devices are freely tunable by design from 200 nm up to 650 nm. A wide range of optoelectronic applications readily emerge, including visible light emitters in the formerly barely obtainable green and blue parts of the spectrum.⁴ Other applications include LDs⁵, solar-blind UV detectors⁶, and high-power high-temperature devices.^{7,8}

The availability of blue and green InGaN LEDs has already lead to the production of large outdoor full color displays, traffic lights, and full color scanners.^{3,9} Solar-blind UV photodetectors find applications in space exploration and monitoring of high temperature furnaces in production processes.¹⁰ Combined with an UV-LED, UV photodetectors enable lithography and pollution monitoring.²

Because of its large energy gap and thermal stability, GaN is suitable for high-frequency, high-power, and high-energy electronic applications. GaN based field effect transistors (FET) operate at temperatures up to 350 °C.² Such high temperature electronics certainly are asked for in the automobile and aerospace industry. The high breakdown voltage of the material invites high-power pulsed operation of GaN based devices, such as radar systems and microwave ovens.²

1.1.2 MATERIAL PROPERTIES

In the introductory remarks, already the bandgap properties of AlN, GaN, and InN have been mentioned. It is worthwhile to further explore the physical and chemical material properties of the three nitride materials under study.

The very small covalent radius of the N-atom (0.7 Å) compared to other group V elements (1.1 Å for P, 1.18 Å for As, and 1.36 Å for Sb) is the reason for the comparatively small lattice parameters of the nitrides.¹¹ These in turn, provide the large bond energies in the three compounds (2.28 eV for AlN, 1.93 eV for InN, and 2.2 eV for GaN), which explain the high melting points of the materials.¹² The high melting temperatures make it difficult to grow bulk crystals by the usual Czochralski method and its variations. Small hexagonal plates of GaN have been grown from a Ga solution in a high pressure N atmosphere, but are not commonly available.¹³ This is the reason for the use of sapphire as the substrate for epitaxial growth of GaN and its alloys. The resulting strain state of the epitaxial thin film complicates sample characterization and device production considerably. The thermodynamically stable lattice structure for all three nitrides is the wurtzite structure, although GaN has reportedly been grown epitaxially in a zinc blende structure as well.¹²

1.1.3 HISTORY OF NITRIDE RESEARCH

The beginnings of group III nitride research date back to about 1970. The first GaN growth experiments were done by halide vapor phase epitaxy (HVPE), a technique used for GaAs growth during the 1960s. Gallium chloride (GaCl_3) was used as a source for Ga and ammonia (NH_3) as a source for N. A fast growth rate allowed for films 100 μm thick or more, which was necessary to "grow out" the defective influence of a highly mismatched sapphire substrate.¹⁴

A problem of the early GaN material grown was the apparently inherent *n*-type doping the film underwent during growth. Even without any deliberate effort to introduce a dopant, *n*-type doping levels of 10^{18} - 10^{20} cm^{-3} were observed.² The cause for

growing *n*-type crystals was assumed to be N vacancies. New studies indicate that O and Si impurities may be responsible.¹⁵

Although basic characterizations of GaN and its alloys have been carried out during the 1970s, device fabrication was out of reach because of the inability to grow *p*-type material. All attempts using Mg, Be, Zn, and Cd acceptors failed. Only the arrival of novel growth techniques devised a solution. In the late 1980s metal organic vapor deposition (MOCVD) and molecular beam epitaxy (MBE) techniques were applied to group III nitride growth.

In order to overcome the misfit problems with the sapphire substrate, buffer layer growth between substrate and active GaN layer was introduced.^{16,17} Finally, *p*-type doping was achieved using MOCVD and Mg as the dopant, and after-growth expulsion of hydrogen, which is thought to form complexes with Mg and thereby neutralizing its acceptor capability.^{18,19} Using MBE, no after-growth processing is necessary since without the use of organic compounds no hydrogen is introduced into the growth process.²⁰

Today controlled *n*-doping is readily achieved by incorporating Si during MOCVD or MBE growth. This makes it possible to grow *p-n* junctions and take the next step towards device fabrication. As mentioned above, LEDs are already commercially available, and LDs on their way to reach the same perfection.

1.2 CONTRIBUTION OF THIS THESIS

This thesis has been written with two main goals in mind. First, a comprehensive summary of the theory of X-ray diffraction from an experimental point of view shall be given. This includes the connection of the theory with the experiment, and the description of the use of the experimental setup and its limitations. Secondly, the measurements performed on a variety of GaN and InGaN epitaxial thin film samples shall be presented and interpretations of the resulting scans shall be given.

Over the course of the following chapters it will become clear that X-ray diffraction is one of the most powerful tools for semiconductor crystal characterization in general, and for epitaxial thin films in particular. Information obtained includes film composition, uniformity, thickness, strain, and crystalline perfection.

With the instrument of X-ray diffraction at hand, a multitude of experimental results have been extracted from different sets of samples. The most striking findings concern a hardly ever observed asymmetry in the $\omega/2\theta$ -scan curves of good MBE-grown GaN thin films on sapphire, and the superlattice interface quality dependence on *n*-type Si doping in a MOCVD-grown InGaN/GaN/AlGaN multi quantum well (MQW) structure. The latter result will also be reported elsewhere.⁵⁷

Further observations include the verification of Vegard's law on MOCVD-grown InGaN thin films, and an investigation of vicinal tilt in GaN epitaxial film on ZnO substrate samples.

Computer programs have been devised to facilitate the simulation of X-ray diffraction curves, and to calculate material properties from peak positions of superlattice diffractions. The simulation program does not have a commercial equivalent since no commercial program concerns itself with the calculation of specifically hexagonal lattice structures, including off-axis reflections.

1.3 ORGANIZATION OF THIS THESIS

The organization of this thesis is straightforward. This introductory chapter is followed by Chap. 2, which will describe a number of aspects relevant to X-ray diffraction theory. Starting with Bragg's equation, the kinematical theory will be developed. Next, a brief overview over the dynamical approach to X-ray diffraction is given. Stress and strain are mentioned to the degree of usefulness to the experiment. A number of equations concerning the characterization of superlattice scans are derived. Finally, the kinematical theory is put to use in form of a computer simulation of a scan.

Chapter 3 introduces the experimental setup. It describes the Philips material research diffractometer (MRD), which has been used to obtain the data for this study. Experimental possibilities and limits are demonstrated, and a detailed description of the different scans and their respective interpretation is given.

In Chap. 4 the various sets of samples characterized and the according experimental results are presented. The sample sets include MBE-grown GaN on sapphire or

ZnO single layer samples, MOCVD-grown InGaN single layers on sapphire, MOCVD-grown InGaN/GaN/AlGaN MQW on sapphire samples, and InGaN/GaN superlattices grown by MBE on sapphire.

A summary of the presented information is given in Chap. 5. The appendices describe the software created necessary for data interpretation and X-ray diffraction simulation.

CHAPTER 2
THEORY OF X-RAY DIFFRACTION FROM
CRYSTALS

2.1 OVERVIEW

When an X-ray beam is incident upon a crystal, some portion of the incident radiation is scattered. This prediction made by M. von Laue led to the first recording of an X-ray pattern on a photographic plate by W. Friedrich and P. Knipping in 1912.²¹ When W. H. and W. L. Bragg did their first X-ray scattering experiments on crystals in 1913 they discovered characteristic scattering patterns. The explanation given, though unphysical even at the time*, proved very useful for the empirical study of crystals via X-ray diffraction.

Bragg's equation is derived from the assumption that the crystal can be seen as a set of specular, equidistant planes [Fig. 2.1. p.8]. Each plane reflects part of the incident X-ray beam. Constructive interference between electromagnetic waves of each reflection creates a reflected signal. For a large number of planes even a tiny change from this condition will yield no appreciable reflected signal. Therefore the condition for reflection is tied to the X-ray beam path difference, as seen in Fig. 2.1. The well known Bragg equation,

$$m\lambda = 2d \sin \theta_B, \quad (2.1)$$

states that an integral number of X-ray wavelengths λ has to equal the X-ray beam path difference $2d \sin \theta$, where d denotes the distance between specular planes, and θ defines the Bragg angle fulfilling the constructive interference condition.

*It had been widely accepted in 1913 that any material consists of atoms. No one ever advocated planes as the building material for matter.

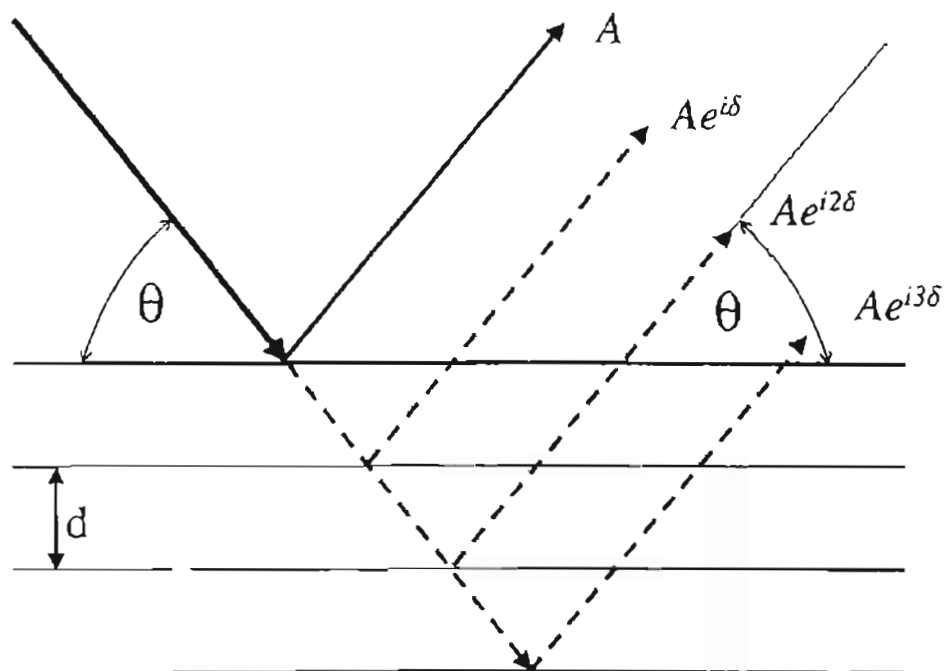


Figure 2.1. *Bragg Scattering Geometry*: The X-ray wave path difference between two planes a distance d apart must be an integer multiple of the X-ray wavelength. If so, specular reflection causes constructive interference: The incoming beam is reflected several times, and all reflected beams of amplitude A are in phase. The angle θ is the Bragg angle, and $\delta = n2\pi$ is an integral multiple of 2π .

Despite its simple derivation, Eq. (2.1) still is a comfortable starting point for more sophisticated approaches, namely the kinematical and the dynamical X-ray diffraction theories. After a brief discussion of physical effects within a crystal which make Bragg's simple specular plane picture work, the development and application of both kinematical and dynamical theories shall be undertaken in the remaining sections of this chapter. First the kinematical theories will be derived, then an introductory overview over the dynamical approach is given. Finally, a simulation comparison between the two theories will show the applicability of the kinematical theory for the samples studied in this work.

2.2 PHYSICAL ORIGIN OF DIFFRACTION

A number of competing effects occur, when X-rays enter matter [Fig.2.2, p. 10]. A monochromatic, narrow X-ray beam is transmitted, scattered, and absorbed all at the same time by a piece of matter in its path. In the case of a crystal, this matter is highly ordered, and coherent scattering patterns can be observed. Incoherent (diffuse) scattering produces background X-ray radiation. Absorption produces heat and loosely bound electrons.

X-rays passing through a crystal induce a dipole moment, inducing a nearby tightly bound electron to radiate a spherical electromagnetic wave of the same frequency as the incident X-ray beam. This is elastic or coherent scattering. Only coherent scattering produces diffraction patterns, since phase relations between scatterers and incident X-ray beam on the one hand, and phase relations between various scatterers within the crystal on the other hand are kept constant during the process.

The coherent diffraction pattern is influenced by inelastic, incoherent scattering effects. The Compton scattering process affects loosely bound electrons by transporting momentum from an X-ray photon to the electron. This collision leaves the X-ray photon with an arbitrary phase and a longer wavelength. Therefore constructive interference between these diffusely scattered X-ray photons does not take place. However, the more loosely the electrons of the crystal material are bound (or, following from that, the smaller the atoms of the elements in the crystal), the bigger the intensity loss for

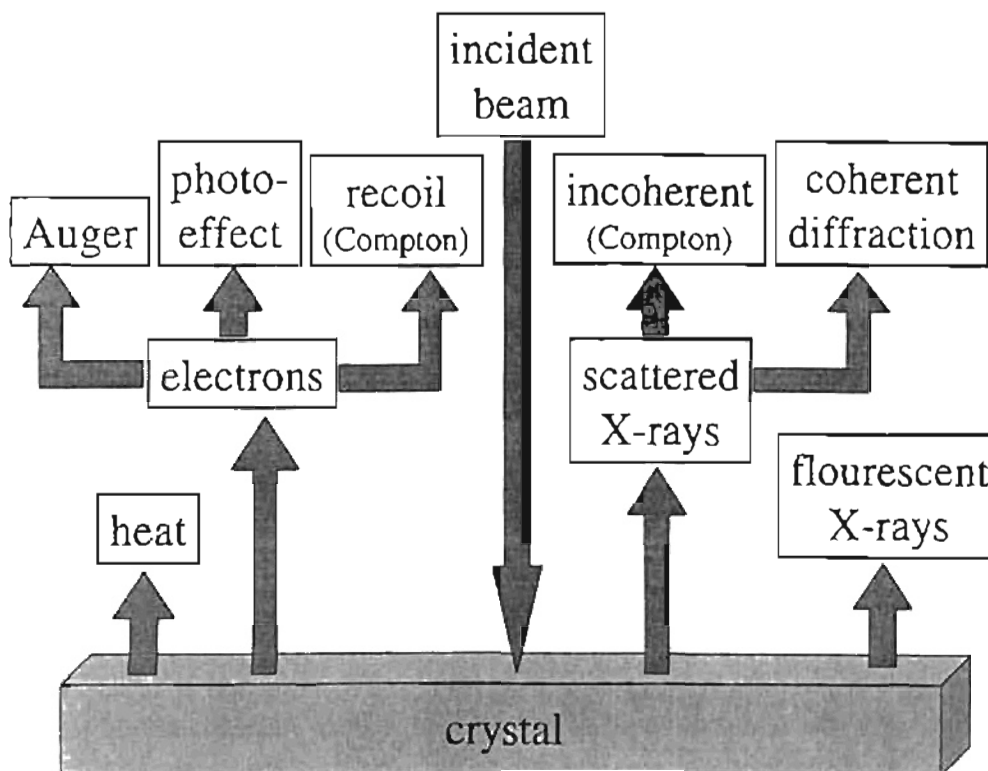


Figure 2.2. *Effects Caused by X-Rays in a Crystal:* Coherently scattered X-rays result in the characteristic diffraction pattern of the crystal. Incoherently scattered X-ray photons and recoiled electrons are due to the Compton effect. Additionally, X-ray absorption also results in the release of photoelectric and Auger electrons. The latter are ejected by characteristic X-ray radiation originating within the atoms of the crystal, which is provoked by the incoming X-ray beam. Phonon assisted processes cause heating. Fluorescence effects are present.

the diffraction pattern. The electron may or may not (phonon assisted Compton effect) leave the atom.

Another inelastic effect is photoelectric absorption. Electrons are excited from one atomic shell to another (K, L, M, ...), or ejected from the atom entirely, by an X-ray photon. Photoelectric absorption depends on the X-ray wavelength λ , becoming greater for higher incident X-ray energies. The minimal absorption condition is $\lambda \leq \lambda_{K\alpha}$, where $\lambda_{K\alpha}$ denotes a wavelength corresponding to a photon energy necessary to excite an electron from the innermost atomic shell K to the very next energy state on shell L (absorption edge). The magnitude of this effect depends on the number of inner electrons. Hence, heavier atoms are more affected than lighter ones. Again, intensity loss for the diffraction pattern follows. The electron may or may not leave the atom. The photoelectric effect may include the emission of fluorescent X-rays and the assistance of phonons.

So far, only electrons have been considered. Atomic nuclei do not scatter X-rays coherently. The X-ray energy is too low. However, since the nucleus is positively charged, a dipole moment is induced by passing X-rays. The mass of the nucleus prohibits appreciable contribution to the much bigger signal put out by the surrounding electrons.

Yet another, virtual particle species has to be considered. Phonons, which constitute normal modes of atomic motion within the crystal lattice, can scatter X-rays, when X-ray photons interact with individual nuclei. Like inelastic electron scattering, a collision between an X-ray photon and a lattice phonon results in momentum transfer. Unlike the limited number of states available for electrons within an atom, phonons have a quasi unlimited number of states to "choose" from. Phonon energies are comparatively small, so that only relatively small changes in wavelength are to be seen in the X-ray photons. If an X-ray photon is absorbed by the nucleus, fluorescent X-rays may be reemitted. In either case, the X-ray photon phase information is lost.

The Compton effect, photoelectric absorption, and phonon scattering, are diffuse scattering processes contributing to the material specific linear absorption coefficient μ of the crystal

$$\mu = \mu_{\text{Compton}} + \mu_{\text{photoeffect}} + \mu_{\text{phonon}}. \quad (2.2)$$

Without differentiating between the underlying effects, experiments show that the decrease in scattered X-ray intensity I is proportional to passed material thickness x ²⁶:

$$\frac{-dI}{I} = \mu dx \quad (2.3)$$

or

$$I_x = I_0 e^{-\mu x}. \quad (2.4)$$

The linear absorption coefficient μ^* is material specific. The penetration depth p is defined as the distance the X-ray beam has to travel within a crystal, after which the original intensity I_0 is reduced to $I_e = I_0/e$, or

$$I_e = I_0 e^{-\mu p} \implies p = \frac{1}{\mu}. \quad (2.5)$$

If constructive interference occurs between the elastic scatterers of the crystal, the penetration depth is limited by another process not taken into account in Eq. (2.5). Back-scattering from the oscillating electrons will interfere destructively with the incident X-ray beam, reducing the penetration depth given by Eq. (2.5) by an order of magnitude.²⁷ Nevertheless, Eq. (2.5) is a convenient way to include absorption in the kinematical theory, which otherwise neglects absorption effects completely.

2.3 KINEMATICAL THEORY

Let us leave the picture of specular planes presented in the introductory section of this chapter, and introduce the more physical kinematical approach to the problem of X-ray scattering. In kinematical theory only elastic scattering is considered. The other physical effects discussed in the previous section will be taken into account with the dynamical theory.

2.3.1 VON LAUE SCATTERING GEOMETRY

When an X-ray photon passes near an electron the electromagnetic wave $E_j = E_0 e^{i\vec{k} \cdot \vec{u}_i}$, corresponding to an X-ray photon with wave vector \vec{k} , it induces a dipole moment affecting the electron. The electron at position \vec{u}_i will oscillate and send out a

*The mass absorption coefficient μ/ρ is the one usually tabulated.³¹ ρ is the mass density of the material.

spherical, dissipative electromagnetic wave with wave vector \vec{k}' [Fig. 2.3, p. 14]. If measured at detector position \vec{R} , the amplitude of the scattered wave will be:

$$\epsilon_{e-} \propto E_j \frac{e^{i\vec{k}' \cdot (\vec{R} - \vec{u}_i)}}{|\vec{R} - \vec{u}_i|} . \quad (2.6)$$

This is the scattering amplitude produced by a single electron due to elastic scattering.²³ No absorption takes place and the energy is conserved within the scattering process. Let us consider two electrons at two lattice sites within a crystal. Two scattering sites constitute the simplest case of a von Laue scattering geometry. Figure 2.4 on p. 15 shows two point scatterers separated by a displacement \vec{d} . Bragg's constructive interference condition now can be rewritten as

$$m\lambda = |d| \cos \theta + |d| \cos \theta' , \quad (2.7)$$

where m is an integer. If vector notation is applied, the same equation transforms to

$$m\lambda = \vec{d} \cdot \left(\frac{\hat{n}}{|\vec{k}|} - \frac{\hat{n}'}{|\vec{k}'|} \right) , \quad (2.8)$$

where \hat{n} and \hat{n}' are unit vectors along \vec{k} and \vec{k}' , respectively. Because of energy conservation $|\vec{k}| = |\vec{k}'|$. Using this and the definition of the wave vectors, $|\vec{k}| = 2\pi/\lambda$, Eq. (2.8) becomes $\vec{d} \cdot (\vec{k} - \vec{k}') = 2m\pi$. Defining the scattering vector

$$\vec{K} = \vec{k} - \vec{k}' , \quad (2.9)$$

and applying the exponential function on either side of $\vec{d} \cdot (\vec{k} - \vec{k}') = 2m\pi$ yields

$$\exp(i\vec{K} \cdot \vec{d}) = 1 . \quad (2.10)$$

Eq. (2.10) is von Laue's diffraction condition. Before it can be applied to the summation of electronic scattering amplitudes, Eq. (2.6), the concept of reciprocal space has to be introduced.

2.3.2 RECIPROCAL SPACE

In order to develop the theory further it is necessary to introduce the concept of reciprocal space. An X-ray diffraction pattern maps out the Fourier transform of the real

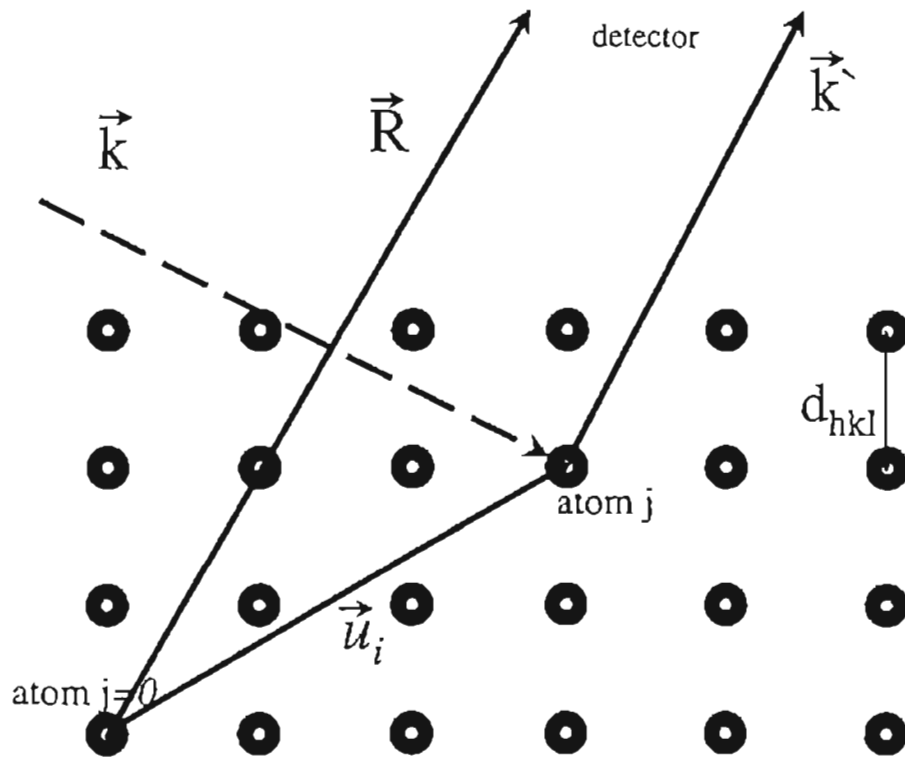


Figure 2.3. *Electronic Scattering Geometry*: An electron at \vec{u}_i within the electronic shell of atom j scatters the X-ray photon \vec{k} in direction of the detector at \vec{R} .

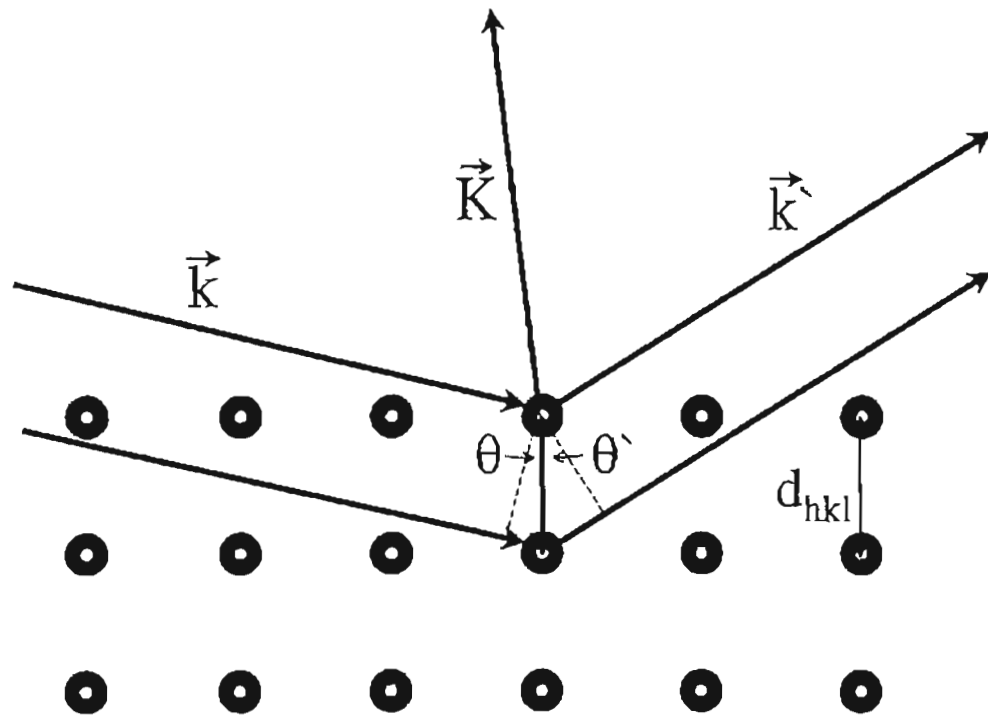


Figure 2.4. *von Laue Scattering Geometry*: Two point scatterers a distance d_{hkl} apart reflect the incoming X-ray \vec{k} in all directions. Because of interference between spherical waves originating at all point scatterers of the crystal, the only surviving direction is \vec{k}' . The scattering vector \vec{K} is defined as $\vec{K} = \vec{k}' - \vec{k}$.

space electron density.³⁰ The electron number density $n(\vec{r})$, depending on the real space vector \vec{r} , is periodic along each crystal axis:

$$n(\vec{r} + \vec{T}) = n(\vec{r}), \quad (2.11)$$

where the vector \vec{T} describes a translation from one real space lattice point to another. The Fourier transform of the electron number density may be written as

$$n(\vec{r}) = \sum_{\vec{G}} n_{(\vec{G})} \exp(i\vec{G} \cdot \vec{r}). \quad (2.12)$$

The electron number density is non-zero only at lattice points. The factors $n_{(\vec{G})}$ are the Fourier series coefficients. The vectors

$$\vec{G} = h \vec{b}_1 + k \vec{b}_2 + l \vec{b}_3 \quad (2.13)$$

define reciprocal lattice points. The integers h, k, l are referred to as Miller indices for sets of planes perpendicular to \vec{G} and planar distance $d = 2\pi/|\vec{G}_{hkl}|$.^{22,23} The vectors $\vec{b}_1, \vec{b}_2, \vec{b}_3$ are the reciprocal lattice basis vectors defined by

$$\vec{b}_i = \frac{2\pi}{V} (\vec{a}_j \times \vec{a}_k) \varepsilon_{ijk}, \quad (2.14)$$

with $\vec{a}_1, \vec{a}_2, \vec{a}_3$ representing the real space lattice basis vectors. $V = \vec{a}_1 \cdot (\vec{a}_2 \times \vec{a}_3)$ is the volume of a unit cell. Figure 2.5 on p. 17 shows real space and reciprocal space lattice vectors for the so defined hexagonal unit cell. Using Eq. (2.11) and Eq. (2.14) and the translation vector $\vec{T} = w_1 \vec{a}_1 + w_2 \vec{a}_2 + w_3 \vec{a}_3$, it is easily shown that the scattering vector \vec{K} defined in Eq. (2.9) can be replaced by the reciprocal lattice vector \vec{G} .

With the above and Eq. (2.12), Eq. (2.11) now may be rewritten as

$$n(\vec{r} + \vec{T}) = \sum_{\vec{G}} n_{(\vec{G})} \exp(i\vec{G} \cdot \vec{r}) \exp(i\vec{G} \cdot \vec{T}). \quad (2.15)$$

This is correct because $\vec{G} \cdot \vec{T} = 2\pi m$ and $\exp(i\vec{G} \cdot \vec{T}) = 1$ with m integer. The last expression, $\exp(i\vec{G} \cdot \vec{T}) = 1$, may be chosen as definition for reciprocal lattice vectors. Comparison with Eq. (2.10) reveals the identity $\vec{G} = \vec{K}$. It follows as a necessary condition that the scattering vector \vec{K} has to be a reciprocal space vector for the case of constructive interference.

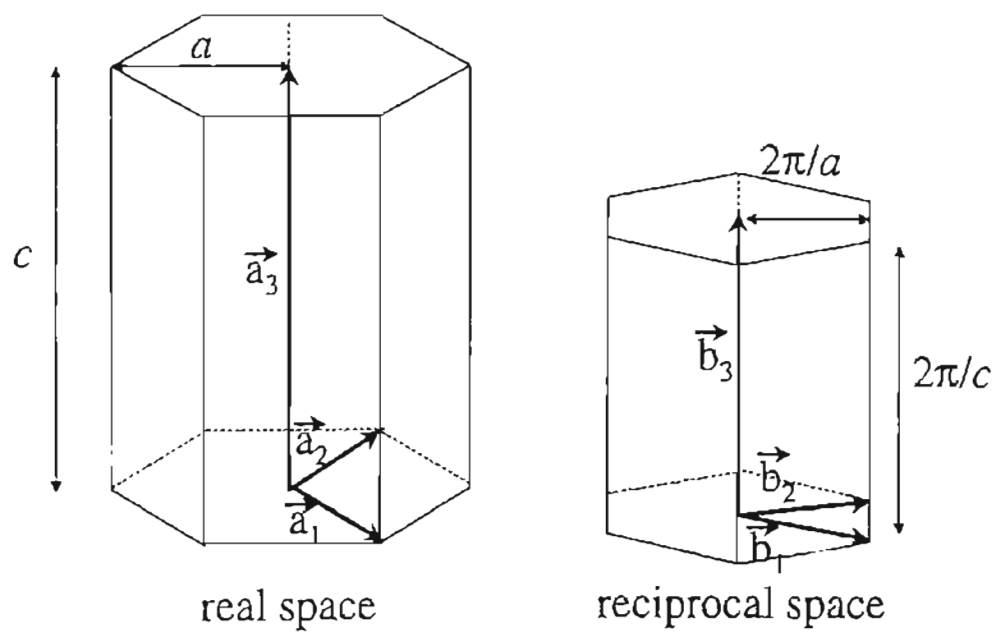


Figure 2.5. *Hexagonal Unit Cell*: The reciprocal space counterpart to the real space hexagonal unit cell is a hexagonal cell, too. Lengths in reciprocal space are given in reciprocal units. The factor 2π depends on the Fourier transformation.

2.3.3 DERIVATION OF BRAGG'S EQUATION

Another, simpler expression for the reflection condition than the one given with Eq. (2.10) can be found by applying reciprocal space results. We will derive Bragg's equation: if only elastic scattering is considered, the incoming and diffracted X-ray beams must have the same energy, $|k| = |k'|$. It has been shown in the previous section that the scattering vector is a reciprocal lattice vector. Using Eq. (2.9) gives $|\vec{k} + \vec{G}| = |\vec{k}'|$. Squaring this yields $2\vec{k} \cdot \vec{G} + |\vec{G}|^2 = 0$. If \vec{G} is a reciprocal lattice vector in an infinite crystal, $-\vec{G}$ is, too. An alternative expression for the diffraction condition then is

$$2\vec{k} \cdot \vec{G} = |\vec{G}|^2. \quad (2.16)$$

This equation can be rewritten by applying the planar distance $d = 2\pi/|\vec{G}_{hkl}|$, the definition of the X-ray wave vector $|k| = 2\pi/\lambda$, and inspection of Fig. 2.4 on p. 15, which shows the relation $\vec{k} \cdot \vec{G} = |k||G| \sin \theta$. Using these three relations Eq. (2.16) transforms itself into the earlier introduced Bragg equation, Eq. (2.1): $2(2\pi/\lambda) \sin \theta = 2\pi/d_{hkl}$, or simplified

$$2d \sin \theta = m\lambda.$$

The integer m may be inserted because h, k, l may contain a common integral factor m . The factor m accounts for path differences between incident and reflected X-ray beam equal to $m\lambda$. This is equivalent to having equidistant virtual planes in between reciprocal lattice planes.

It is necessary to calculate the planar spacing $d = 2\pi/|\vec{G}|$ of the hexagonal plane set (hkl) . A straightforward calculation using the definition for the reciprocal space basis vectors \vec{b}_i in Eq. (2.14), and the definition of the reciprocal space vector \vec{G} in Eq. (2.13), the result for d can be shown to be²⁶

$$\frac{1}{d^2} = \frac{4}{3a^2}(h^2 + hk + k^2) + \frac{l^2}{c^2}. \quad (2.17)$$

2.3.4 RELATIVE DIFFRACTED INTENSITY

For a geometry where the detector is far away from the sample, and covers only a small solid angle, the approximations $\vec{R} \parallel \vec{k}'$, and $|\vec{R} - \vec{u}_i| \approx R$ can be made [Fig. 2.3,

p. 14]. Eq. (2.6) then transforms into

$$\epsilon_{e^-} \propto E_j \left(\frac{1}{R} e^{i\vec{k}' \cdot \vec{R}} \right) e^{-i\vec{k}' \cdot \vec{u}_i}. \quad (2.18)$$

This is a plane wave, as can be seen by inserting $E_j = E_0 e^{i\vec{k} \cdot \vec{u}_i}$. Now the scattering vector $\vec{K} = \vec{k}' - \vec{k}$ [Eq. (2.9)] can be identified and introduced into the equation,

$$\epsilon_{e^-} \propto E_0 \left(\frac{1}{R} e^{i\vec{k}' \cdot \vec{R}} \right) e^{-i\vec{K} \cdot \vec{u}_i}. \quad (2.19)$$

If Z electrons, numbered by the index i , surround the nucleus of atom j , \vec{u}_i has to be replaced by $\vec{u}_i = \vec{r}_j + \vec{w}_{ji}$ where \vec{r}_j denotes the position of nucleus j and \vec{w}_{ji} holds the positions of the electrons i around nucleus j :

$$\epsilon_{atom j} \propto \sum_i^{(\text{electrons})} e^{-i\vec{K} \cdot (\vec{r}_j + \vec{w}_{ji})}. \quad (2.20)$$

Now a switch can be made from the sum over the electrons i within atom j , to a volume integral multiplied with the electron number density $n_j(\vec{r}_j + \vec{w}_{ij})$ of atom j :

$$\epsilon_{atom j} \propto \int_{\text{all space}} dV n_j(\vec{r}_j + \vec{w}_{ij}) e^{-i\vec{K} \cdot (\vec{r}_j + \vec{w}_{ij})}. \quad (2.21)$$

Eq. (2.21) defines the atomic form factor f_j of atom j :

$$f_j = \int_{\text{all space}} dV n_j(\vec{\rho}) e^{-i\vec{K} \cdot (\vec{\rho})}, \quad (2.22)$$

where $\vec{\rho}$ denotes a real space vector measured from a chosen origin ($n_j(\vec{\rho})$ certainly does not depend on a given coordinate system). The atomic form factors f_j of the atoms in the crystal lattice unit cell describe the relative contributions each atom makes to the reflected intensity. Interference within the atom defines the contributions made by different atomic species. For the simplest approximation of a spherical electron distribution around the nucleus the angular integration of the volume integral may be carried out²²:

$$f_j = 4\pi \int_0^\infty dr r^2 n_j(r) \frac{\sin Gr}{Gr} \quad (2.23)$$

This gives a hint at the general shape of form factor functions as seen in Fig. 2.6 on p. 20. Atomic form factors are usually given as functions dependent on the wavelength dependent argument $\sin \theta / \lambda$, which is proportional to the reciprocal lattice vector $|\vec{G}_{hkl}|$.

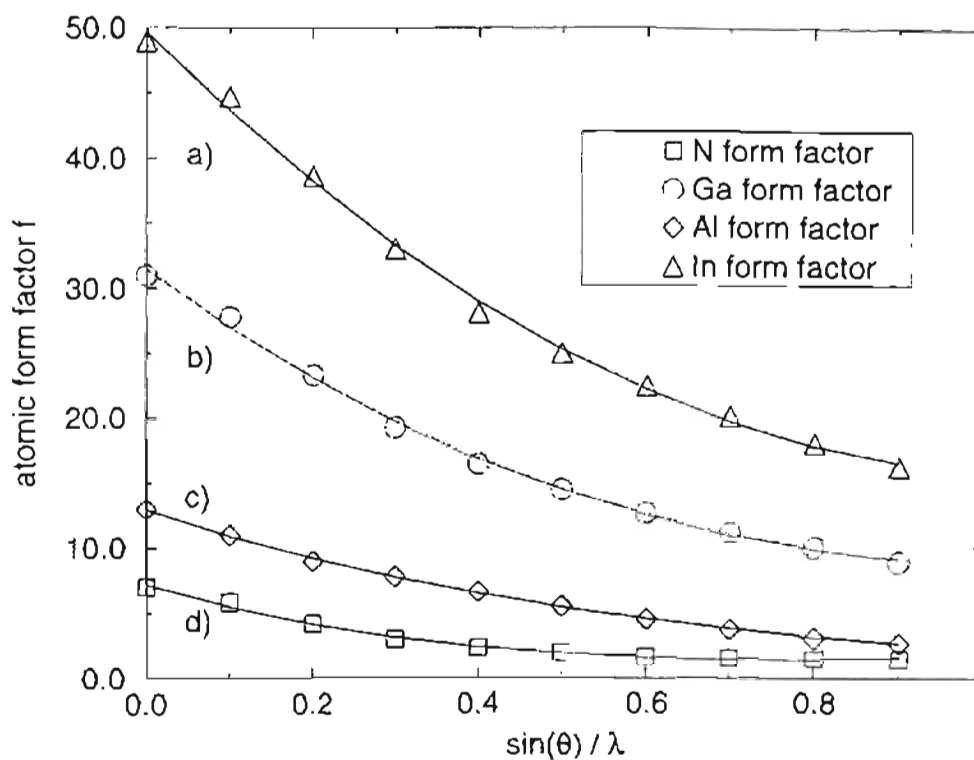


Figure 2.6. *Fitting Atomic Form Factors:* The kinematical computer simulation used in this study fits the atomic form factor with a third-degree polynomial by the method of least squares. a) In: $f_{In} = -1.85x^3 + 27.55x^2 - 63.12x + 49.69$, b) Ga: $f_{Ga} = -5.23x^3 + 29.97x^2 - 47.63x + 31.47$, c) Al: $f_{Al} = -5.13x^3 + 16.13x^2 - 21.89x + 12.97$, and d) N fit: $f_N = -6.90x^3 + 20.09x^2 - 18.84x + 7.18$.

The magnitude of f_j is proportional to the number of electrons in the respective atom. Forward scattering yields a maximum intensity since all electrons within the atom are oscillating in phase. As the angle increases, increasing path differences of the same order of magnitude as the diameter of the atom arise.

If a sum over the atoms of the crystallographic basis is introduced to Eq. (2.20), the result is the scattering amplitude of the basis

$$\epsilon_{\text{basis}} \propto \sum_j^{(\text{basis atoms})} e^{-i\vec{K}\cdot\vec{r}_j} \sum_1^Z e^{-i\vec{K}\cdot\vec{w}_{j1}}. \quad (2.24)$$

Switching to an integral again, the definition for the structure factor S comes out to be

$$S = \int_{\text{unit cell}} dV n(\vec{\rho}) e^{-i\vec{K}\cdot\vec{\rho}}, \quad (2.25)$$

where $n(\vec{\rho}) = \sum_j^{(\text{basis atoms})} n_j(\vec{\rho})$ is the electronic number density of the whole unit cell. Applying the expression for the form factor in Eq. (2.21) to the above, the definition of the structure factor $S(\vec{G})$, with $\vec{G} = \vec{K}$ as seen before, is given by^{22,23}

$$S_{\vec{G}} = \sum_j f_j \exp(-i\vec{G}_{hkl} \cdot \vec{r}_j). \quad (2.26)$$

The Miller indices in \vec{G}_{hkl} define the set of planes from which the beam is scattered. If the positions of the atoms in the unit cell $\vec{r}_j = x_j \vec{a}_1 + y_j \vec{a}_2 + z_j \vec{a}_3$ are known, the structure factor takes the form

$$S(hkl) = \sum_j f_j \exp[-i2\pi(hx_j + ky_j + lz_j)]. \quad (2.27)$$

Inspection of Eq. (2.27) reveals that, fulfilling Bragg's specular plane condition alone does not necessarily yield constructive interference. Only after the summation over all atoms of the basis is carried out, it can be seen, if or if not the plane set (hkl) will reflect X-rays. If the sum is zero, reflection from the plane set is forbidden.

Now, for a multilayer thin film epitaxial structure, the reflected amplitude A has to be calculated by first multiplying the basis structure factor $S(hkl)$ with the number of atomic layers (monolayers) N of the first epitaxial layer:

$$A_1 = \sum_{n=1}^N S(hkl) \exp(-i|\vec{k}|nd). \quad (2.28)$$

Then the scattering amplitude A_2 of the next epitaxial layer is calculated in the same way, except it is multiplied by a phase factor $\exp(i|\tilde{k}|Nd)$ to account for the X-ray beam phase after passing through the first epitaxial layer. For j layers of epitaxial thin film the total amplitude will be:

$$A_{layers} = A_1 + A_2 e^{-i|\tilde{k}|x_1} + A_3 e^{-i|\tilde{k}|(x_1+x_2)} + \dots + A_j e^{-i|\tilde{k}|(x_1+x_2+\dots+x_{j-1})}, \quad (2.29)$$

where the thicknesses x_i refer to the respective epitaxial film layers. The epitaxial layer amplitude A_{layers} in a last step needs to be combined with the reflected amplitude of the underlying substrate. The substrate material constitutes a film so thick, that absorption effects can be no longer ignored. To find the substrate amplitude A_s we have to combine Eq. (2.28) and Eq. (2.4),

$$A_s = \sum_{n=1}^{\infty} S(hkl) \exp(-i|\tilde{k}|n d - \mu n d). \quad (2.30)$$

Using the result of the infinite geometric series as well as $\mu = 1/p$ gives

$$A_s = S(hkl) \frac{1}{1 - \exp(-i|\tilde{k}|d - \frac{1}{p}d)}. \quad (2.31)$$

Finally the total scattered intensity I_{total} is given by the square of the amplitude:

$$I_{total} = (A_{layers} + A_s e^{-i|\tilde{k}|(x_1+x_2+\dots+x_j)})^2. \quad (2.32)$$

This result is proportional to the photon count rate given by the detector of the experimental setup.

2.4 DYNAMICAL THEORY

The more physically complete dynamical theory of X-ray scattering from a crystal yields more reliable results than the kinematical approach in every aspect of the simulation process. For the simulation of X-ray scattering of high quality crystals there is no alternative to this method.²⁷ Dynamical theory takes into account multiple scattering, the small deviation of the refractive index from unity, and the various absorption effects discussed earlier (Section 2.2).

The concept for the dynamical theory was originally developed by Darwin, Ewald and von Laue.³²⁻³⁴ Prins modified the formalism to include absorption effects.³⁵

The kinematical theory only considers the radiative response of each individual atom of the crystal to the primary, incident X-ray beam, and sums up the various responses. The dynamical theory describes the interaction of emitted electromagnetic waves from each atom not only with the incident beam, but also with electromagnetic fields created by all the other atoms in the lattice. The collective scattering of all atoms creates a wave field. This wave field then describes the scattering of the atoms, the multiwave scattering or secondary scattering between the atoms, and the interaction of the diffracted waves with the refracted incident beam.

In the original Darwin-Ewald-Laue formulation the exact solution of a wave field excited within the crystal is approached in a series of iterations. The incident wave is

$$\chi_i = \sum_{\vec{k}} c_{\vec{k}} \Psi_{\vec{k}}(\vec{r}), \quad (2.33)$$

where wavevector \vec{k} is slightly varied within the Bloch functions²²

$$\Psi_{\vec{k}}(\vec{r}) = u_{\vec{k}} \exp(i\vec{k} \cdot \vec{r}), \quad (2.34)$$

where $u_{\vec{k}}(\vec{r}) = u_{\vec{k}}(\vec{r} + \vec{T})$ has the period of the crystal lattice. The Bloch functions represent the solution to the Schrödinger equation within a periodic crystal.^{22,27} A sum of incident wave field χ_i and scattered wave field χ_{sc} with a slight amplitude and phase difference yields the resulting diffraction pattern*. The solution is self consistent.

*This is the Pendellösung: German for pendulum solution — in accordance with the phase modulation solution of two or more harmonic oscillators

Commercial scattering simulation software almost exclusively uses another dynamical theory formalism developed by Takagi and Taupin.^{36–38} To date, simulation software is only available for cubic crystal systems. The Takagi-Taupin formalism is equivalent to the Darwin-Prins formalism for continuous crystal media.³⁹

The simplest case of the dynamical Takagi-Taupin formalism is given with a two beam (incident and diffracted) approximation. The coefficients of the sum representing the excited wave field within the crystal, vary with depth z . The Takagi-Taupin equations governing the relation between incoming wave amplitude A_i and scattered wave amplitude A_{sc} are²⁷

$$\frac{i\lambda\gamma_s}{\pi} \frac{\partial A_{sc}}{dz} = -\frac{\lambda r_e S_{hkl}}{\pi V} A_{sc} + C \frac{\lambda r_e S_{hkl}}{\pi V} A_i + \frac{2\lambda(\theta - \theta_{hkl})}{d_{hkl}} A_{sc} \quad (2.35)$$

$$\frac{i\lambda\gamma_i}{\pi} \frac{\partial A_i}{dz} = -\frac{\lambda r_e S_{hkl}}{\pi V} A_i + C \frac{\lambda r_e S_{hkl}}{\pi V} A_{sc} \quad (2.36)$$

The following notations have been used: r_e is the classical electron radius, V is the volume of a unit cell, S_{hkl} is the structure factor of a unit cell. The value of C depends on the polarization of the incoming X-ray beam: $C = 1$ if the X-ray \vec{E} -field is polarized perpendicularly to the incident plane (σ -polarization); $C = |\cos 2\theta_{\text{Bragg}}|$ if the X-ray \vec{E} -field is polarized parallel to the incident plane (π -polarization). The incident plane is defined by the incident and reflected wave vectors \vec{k} and \vec{k}' . By choosing the waves A_i and A_{sc} along \vec{k} and \vec{k}' respectively, the reflecting set of planes (hkl) is defined.

Now define the complex variables X , η , and T with the direction cosines γ_i , γ_s as shown in Fig. 2.7 on p. 25²⁷:

$$X = \sqrt{\frac{S_{\bar{h}\bar{k}l} |\gamma_s|}{S_{hkl} |\gamma_i|}} \frac{A_{sc}}{A_i}, \quad (2.37)$$

$$\eta = \frac{-\gamma_i/\gamma_s (\theta - \theta_{hkl}) \sin 2\theta_{hkl} - \frac{1}{2}(r_e \lambda^2/\pi V) S_{000} (1 - \gamma_i/\gamma_s)}{\sqrt{|\gamma_i/\gamma_s|} C (r_e \lambda^2/\pi V) \sqrt{S_{hkl} S_{\bar{h}\bar{k}l}}}, \quad (2.38)$$

$$T = \frac{\pi C (r_e \lambda^2/\pi V) \sqrt{S_{hkl} S_{\bar{h}\bar{k}l}}}{\lambda \sqrt{|\gamma_i \gamma_s|}} x. \quad (2.39)$$

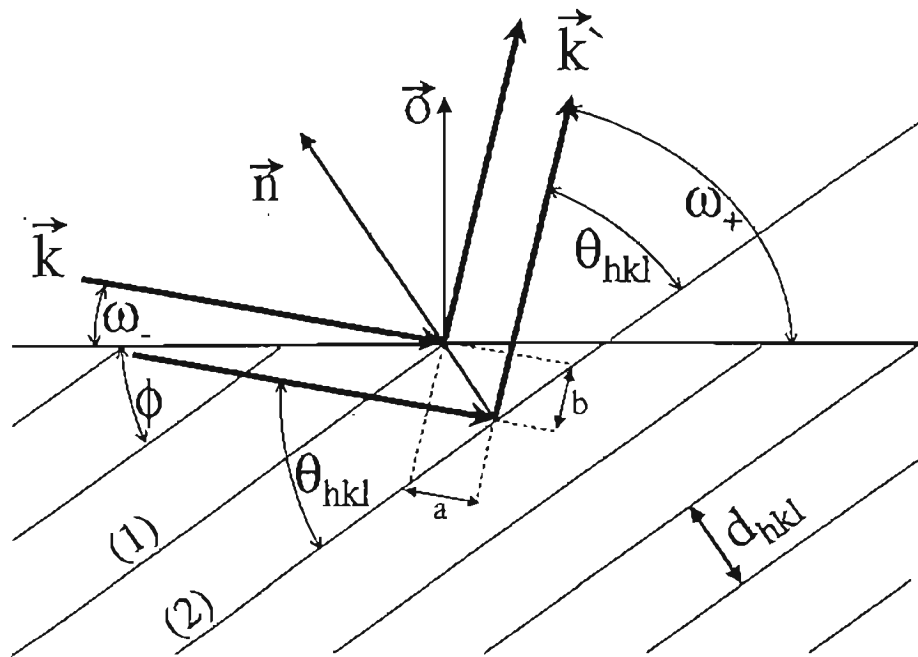


Figure 2.7. *Bragg scattering geometry (Asymmetrical)*: The distance $a + b$ is the X-ray wave path difference between two planes [(1)+(2)] a distance d_{hkl} apart. θ_{hkl} is the Bragg angle. The cosines of the angles ω_1 and ω_2 indicate the instrument orientation with respect to the Bragg planes. They define the direction cosines $\gamma_i = \frac{k_i}{|k|} \cos \omega_1$ and $\gamma_s = \frac{k'_s}{|k'|} \cos \omega_2$. ϕ denotes the angle between the set of planes (hkl) and the sample surface. The vectors \hat{n} and \hat{o} are the hkl plane and surface normals, respectively.

The angular dependence of the wave amplitude now is found within η . The deviation parameter η is given with respect to the Bragg position θ_{hkl} . S_{000} denotes the structure factor at the origin of reciprocal space. In the expression for T , which is a collection of various aspects of the scattering geometry, x stands for the thickness of a layer the scattering takes place in. Taking advantage of the above definitions a simpler differential equation, depending on the wave amplitude ratio A_{sc}/A_i as given in X [Eq. (2.37)] can be obtained²⁷:

$$-i \frac{dX}{dT} = X^2 - 2\eta X + 1. \quad (2.40)$$

The solution of (2.40) for finite crystal thickness x is²⁷

$$X_x = \eta + \sqrt{\eta^2 - 1} \frac{B_1 + B_2}{B_1 - B_2}, \quad (2.41)$$

with

$$B_{1,2} = (X_0 - \eta \pm \sqrt{\eta^2 - 1}) \exp(\mp iT \sqrt{\eta^2 - 1}). \quad (2.42)$$

This would be a sufficient result for one epitaxial, thin layer. In reality the substrate material and multiple layers would have to be considered. For $x \rightarrow \infty$ the solution becomes²⁷

$$X_\infty = \eta - \text{sign}(\text{Re}(\eta)) \sqrt{\eta^2 - 1}. \quad (2.43)$$

The final step is finding the reflected intensity depending on the Bragg parameter θ . For one layer the reflectivity R only depends on the incoming and diffracted waves and their respective direction cosines^{27,25}

$$R_{\text{single}} = \left| \frac{\gamma_s}{\gamma_i} \right| \cdot \left| \frac{A_{sc}}{A_i} \right|^2. \quad (2.44)$$

One can transform the above considering Eq. (2.37) and gets²⁷

$$R_{\text{single}} = \left| \frac{S_{hkl}}{S_{\overline{hkl}}} \right| \cdot |X|^2. \quad (2.45)$$

This result describes the reflectivity (normalized intensity) of an epitaxial thin film depending on the deviation parameter η , where η depends on the angular deviation from the Bragg angle [Eq. (2.38)].

The model for a complete multilayer heterostructure involves the introduction of boundary conditions for every interface, which makes the calculation a very elaborate exercise which will not be undertaken here.

2.5 STRESS AND STRAIN

Stress is a force per area causing strain in a solid body. The six independent stresses acting on a volume element are shown in Fig. 2.8 (a) on p. 28.²³ For sufficiently small stress and strain the relation between stress σ and strain ϵ is linear, and the proportionality factor C is the stiffness constant.²⁷ For hexagonal symmetry the relation between stress and stiffness is given by

$$\begin{pmatrix} \sigma_{xx} \\ \sigma_{yy} \\ \sigma_{zz} \\ \sigma_{yz} \\ \sigma_{zx} \\ \sigma_{xy} \end{pmatrix} = \begin{pmatrix} C_{11} & C_{12} & C_{13} & 0 & 0 & 0 \\ C_{12} & C_{11} & C_{13} & 0 & 0 & 0 \\ C_{13} & C_{13} & C_{33} & 0 & 0 & 0 \\ 0 & 0 & 0 & C_{44} & 0 & 0 \\ 0 & 0 & 0 & 0 & C_{44} & 0 \\ 0 & 0 & 0 & 0 & 0 & C_{66} \end{pmatrix} \cdot \begin{pmatrix} \epsilon_{xx} \\ \epsilon_{yy} \\ \epsilon_{zz} \\ \epsilon_{yz} \\ \epsilon_{zx} \\ \epsilon_{xy} \end{pmatrix} \quad (2.46)$$

For samples studied here, the applied stress will be biaxial, parallel to the sample surface, caused by a lattice mismatch between substrate and epitaxial layer. There is no stress in the growth direction:

$$\sigma_{zz} = C_{13} \epsilon_{xx} + C_{13} \epsilon_{yy} + C_{33} \epsilon_{zz} = 0. \quad (2.47)$$

Perpendicular to the growth direction (z -direction) the x and y directions are equivalent by symmetry:

$$\sigma_{xx} = \sigma_{yy} \Leftrightarrow C_{11} \epsilon_{xx} + C_{12} \epsilon_{yy} + C_{13} \epsilon_{zz} = C_{12} \epsilon_{xx} + C_{11} \epsilon_{yy} + C_{13} \epsilon_{zz}. \quad (2.48)$$

With no stress in z -direction and no preferred stress direction in-plane, there is no shear force acting on a unit volume, hence

$$\sigma_{yz} = \sigma_{zx} = \sigma_{xy} = \epsilon_{yx} = \epsilon_{xz} = \epsilon_{xy} = 0. \quad (2.49)$$

The definition of hexagonal epitaxial strain of a thin film grown on a substrate involves the in-plane lattice parameter a , and the growth direction lattice parameter c .²⁷ The substrate does not change its lattice parameters, whereas the film does, and thus the film experiences strain:

$$\epsilon_{xx} = \epsilon_{yy} = \frac{a_0^{\text{substrate}} - a_0^{\text{layer}}}{a_0^{\text{layer}}} \quad (2.50)$$

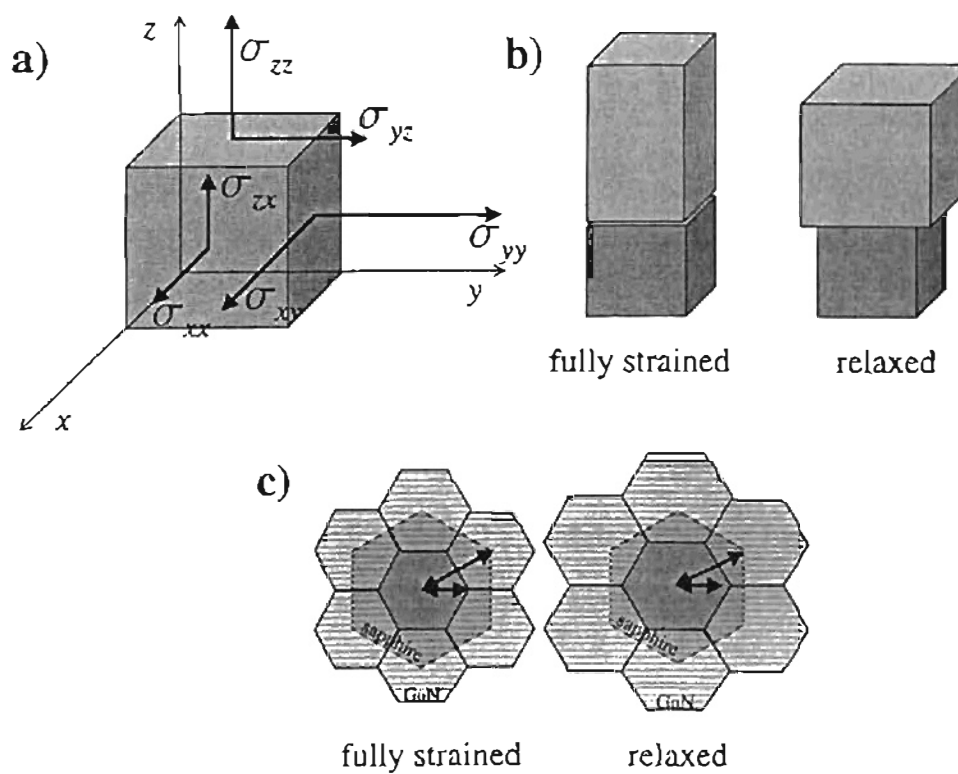


Figure 2.8. *Stress and Strain*: a) Stresses acting torque free on a unit volume defined as force per area, b) fully strained and relaxed epitaxial films in general, and c) for GaN on sapphire in particular.

and

$$\epsilon_{zz} = \frac{c_{\text{strained}}^{\text{layer}} - c_0^{\text{layer}}}{c_0^{\text{layer}}}, \quad (2.51)$$

where the index 0 denotes the fully relaxed value.

With the above equation it is now possible to calculate the changed lattice parameters of a fully strained thin film. While the in plane lattice parameter will take on the same value as the substrate parameter, the change in c^{layer} depends on the elastic stiffness constants of the film material. By means of straight forward algebra Eq. (2.47) and Eq. (2.48) yield the definition for the ‘‘tetragonal’’ distortion ϵ_t :

$$\epsilon_t = -\frac{\epsilon_{zz}}{\epsilon_{xx}} = \frac{2C_{13}}{C_{33}}. \quad (2.52)$$

With the definition for ϵ_{zz} , Eq. (2.51), the result for the distorted lattice parameter $c_{\text{strained}}^{\text{layer}}$ is

$$\begin{aligned} c_{\text{strained}}^{\text{layer}} &= c_0^{\text{layer}} (1 + \epsilon_{zz}) \\ &= c_0^{\text{layer}} \left(1 - \frac{2C_{13}}{C_{33}} \epsilon_{xx} \right) \\ &= c_0^{\text{layer}} \left(1 - \epsilon_t \frac{a_0^{\text{substrate}} - a_0^{\text{layer}}}{a_0^{\text{layer}}} \right). \end{aligned} \quad (2.53)$$

For most experimental purposes it is common practice to give strains in growth direction, ϵ_{\perp} , and in plane direction, ϵ_{\parallel} , relative to the relaxed substrate lattice parameters:

$$\epsilon_{\parallel} = \frac{a_0^{\text{layer}} - a_0^{\text{substrate}}}{a_0^{\text{substrate}}} \quad (2.54)$$

and

$$\epsilon_{\perp} = \frac{c_0^{\text{layer}} - c_{\text{strained}}^{\text{layer}}}{c_{\text{strained}}^{\text{layer}}}, \quad (2.55)$$

where ϵ_{\parallel} is referred to as biaxial strain. Relations between the two definitions follow immediately:

$$\epsilon_{xx} = (\epsilon_{\parallel} + 1) \frac{a_0^{\text{substrate}}}{a_0^{\text{layer}}} - 1 \quad (2.56)$$

and

$$\epsilon_{zz} = (\epsilon_{\perp} + 1) \frac{c_{\text{strained}}^{\text{layer}}}{c_0^{\text{layer}}} - 1. \quad (2.57)$$

2.6 SUPERLATTICE ANALYSIS

From superlattice diffraction patterns such as the one shown in Fig. 2.11 on p. 41, a wealth of information about the sample can be extracted. The positions of the various peaks, the full widths at half maximum (FWHM), and the relative intensities allow conclusions to be drawn about lattice constants, layer thicknesses, material composition and its variation, interface roughness and grading, interdiffusion, and strains within the layers.²⁷

2.6.1 QUALITATIVE VIEW

When an incident X-ray beam is scattered by a superlattice structure, the resulting diffraction pattern will be a convolution of several inherent diffraction patterns. Let us consider separately the effect on the diffraction pattern given by the length of one period L , the total thickness NL of a superlattice with N periods, the thicknesses L_A and L_B of the alternating layers A and B , and, finally, their respective planar spacings d_A and d_B .

The Fourier-transform of the electron density distribution within the superlattice maps out reciprocal space. The Fourier-transform of the real space superlattice arrangement as depicted above, will yield the diffraction pattern. Sublattices A and B have to be handled separately, if $d_A \neq d_B$. The planar distance d_A (d_B) determines the position of the zeroth order peak as defined by Bragg [Eq. (2.1)]. The Fourier transform of the layer thickness L_A (L_B) is a Gaussian of width $4\pi/L_A$ ($4\pi/L_B$). The Gaussian acts as an envelope for the superlattice satellite peaks. The satellite peaks themselves are caused by the fact that, the period containing layer A (B) is repeated N times. That allows interference between scattered waves, originated at every layer A (B). In analogy to the simpler case of diffraction on a grating, there are also $N - 2$ smaller intensity maxima between the satellite peaks. In the experiment, these will only be seen for high quality superlattices.

Every satellite peak needs to be convoluted with the Fourier-transform of the total superlattice thickness NL , which is a narrow Gaussian of width $4\pi/NL$. The latter Gaussian determines the width of the individual superlattice peaks.

In the case of a fully-strained superlattice d_A and d_B will average depending on the respective layer thicknesses L_A and L_B . Then only one superlattice diffraction pattern will be seen, centered around the average zeroth order peak. This is the case for the samples under study.

2.6.2 PEAK POSITIONS

In the following a two material (A,B) superlattice with N periods of length $L = L_A + L_B$ and, within the superlattice, strained plane spacing $d_{avg} = (d_A L_A + d_B L_B)/L(d_A + d_B)$, on a substrate with plane spacing d_{sub} is kept in mind as a basis for the analysis.

Bragg's equation, Eq. (2.1), can be applied to the superlattice period L ,

$$m\lambda = 2L \sin \theta_m . \quad (2.58)$$

where m is the Bragg index of the superlattice peak. If Eq. (2.58) is subtracted from the same expression for superlattice peak index $n = L/d_{avg}$, the result is

$$2L \sin \theta_n = \lambda(n - m) + 2L \sin \theta_m , \quad (2.59)$$

where n is the number of monolayers in one period. By virtue of invoking Bragg's equation once more in the form

$$\lambda = 2 \frac{L}{n} \sin \theta_n = 2d_{avg} \sin \theta_{d_{avg}} \quad (2.60)$$

Eq. (2.59) becomes

$$L \frac{\lambda}{d_{avg}} = (n - m)\lambda + 2L \sin \theta_m . \quad (2.61)$$

The superlattice equation is gained by dividing by λ and L :

$$\frac{2 \sin \theta_m}{\lambda} = \frac{1}{d_{avg}} + \frac{m - n}{L} . \quad (2.62)$$

The variables in Eq. (2.63) are the superlattice peak angle θ_m and the corresponding peak index m . By definition the position of the zeroth order superlattice peak is the one which coincides with the superlattice Bragg angle $\theta_{d_{avg}}$. In order to fulfill the definition, a renaming of the peaks has to be done. With $q = m - n$ the final expression for the superlattice equation is

$$\frac{2 \sin \theta_q}{\lambda} = \frac{1}{d_{avg}} + \frac{q}{L}. \quad (2.63)$$

If experimental superlattice peaks are considered, data points emerge which have to be assigned Bragg indices which may or may not coincide with the above definition for q . They lie on a straight line and can be numerically fitted by the general linear expression $y = sx + b$ with $y = 2 \sin \theta_q / \lambda$ and $x = q$. A difficulty arises due to the fact that the Bragg indices are not known beforehand. However, by inspecting the superlattice Eq. (2.63), it becomes clear that, for $\theta_q = 0$, the Bragg index $-q = -n$ becomes equal to the number of monolayers in a period, $n d_{avg} = L$. For $q = 0$ the Bragg angle $\theta_{d_{avg}}$ ensures the validity of Bragg's diffraction condition regarding the plane spacing d_{avg} .

By shifting the x -axis intercept as close as possible to the origin by means of adding an integer to the fitted line, the highest order reflection n is shifted to the $x = 0$ position. With this, the physical zeroth order superlattice peak shifts to $x = n$. Now shift the line fit to the left by subtracting n . The physical zeroth order peak will be at $x = 0$ and the usual satellite peak orders as seen in Fig. 2.11 on p. 41 are in the right position as well. Fig. 2.9 on p. 33 shows an example of this.

The slope $s = 1/L$ immediately gives the superlattice period. The y -axis intercept $1/d_{avg}$ gives the average plane spacing within the repeated layers. An error analysis can be done by simply entering the experimental resolution as an error bar for θ in above equations. This will yield error bars for L and d_{avg} in a straightforward manner.

Of course, the plane spacing d_{avg} could be obtained by considering the zeroth order peak alone. However, the superlattice equation is more precise, since it uses positions of all visible peaks, not only one.

By knowing d_{avg} it is possible to extract the value of the perpendicular strain ϵ_{zz} of the superlattice and, in case one layer of a period is an alloy containing the material of

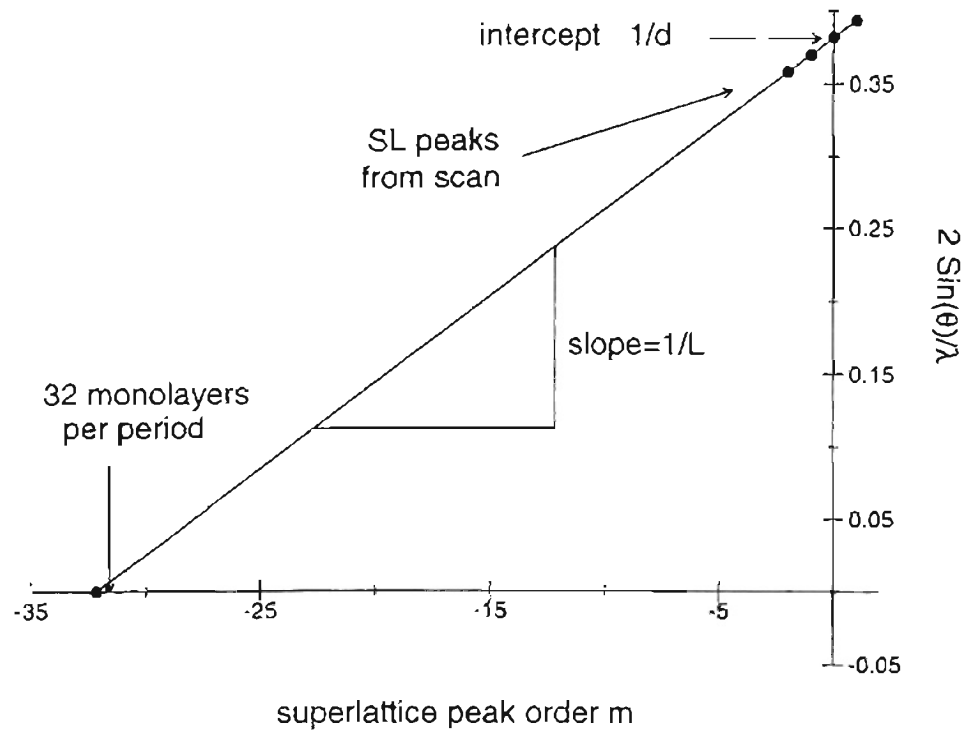


Figure 2.9. *Superlattice Analysis*: According to the superlattice equation [Eq. (2.63)] superlattice period $L = 84.25\text{\AA}$ and average plane spacing $d = 2.62\text{\AA}$ can be determined. The linear fit is $y = 0.01187x + 0.381885$.

the other layer, the composition coefficient x . In order to gain the perpendicular strain use Eq. (2.51):

$$\epsilon_{zz} = \frac{d_{avg}}{d_{sub}} - 1 \quad \text{and} \quad d\epsilon_{zz} = \sqrt{2} \frac{d(d_{avg})}{d_{avg}}. \quad (2.64)$$

The error $d\epsilon_{zz}$ depends on the error d_{avg} of the superlattice plane spacing. Let layer A be GaN and layer B be $\text{In}_x\text{Ga}_{1-x}\text{N}$. If the superlattice grows relaxed on a GaN substrate, the alloy composition is given approximately by Vegard's law:

$$x_{rel} = \frac{d_{avg} - d_{sub}}{d_{InN} - d_{sub}} = \frac{\epsilon_{zz}}{d_{InN}/d_{sub} - 1} \quad \text{and} \quad dx_{rel} = x \frac{d\epsilon_{zz}}{\epsilon_{zz}}. \quad (2.65)$$

This is a relation between the mixed planar spacing d_{avg} and the pure planar spacing d_{InN} of InN. The error is proportional to the variation in ϵ_{zz} . For a strained situation the tetragonal distortion has to be taken into account:

$$x_{str} = \frac{\epsilon_{zz}}{\left(\frac{d_{avg}}{d_{sub}} - 1\right) \epsilon_t} \quad \text{and} \quad dx_{str} = x \sqrt{\left(\frac{d\epsilon_{zz}}{\epsilon_{zz}}\right)^2 + \left(\frac{0.1}{\epsilon_t}\right)^2}. \quad (2.66)$$

All presented formulas are simple enough to be applied in a straight forward manner. A computer program has been written and applied to studied superlattice scans (SLAnalyzer, see Appendix).

2.6.3 PEAK WIDTH AND INTENSITY

For single epitaxial thin films, the FWHM of the diffraction peak of a 2θ -scan indicates the overall material quality of the layer. The FWHM is closely related to the coherence length in the direction specified by the scan taken. The coherence length describes a typical length within the crystal within which there are no lattice imperfections. This concept is refined by Scherrer's formula, which shall be derived now.

Let us assume one perfect epitaxial layer consisting of m parallel planes of spacing d parallel to the layer surface. The thickness of the layer then is $L = md$. The Bragg condition is fulfilled for an incident X-ray beam of wavelength λ for the Bragg angle θ_B :

$$\lambda = 2d \sin \theta_B. \quad (2.67)$$

Since this layer is of finite thickness, the diffracted intensity signal will be distributed like a Gaussian function centered at the Bragg angle. Let us approximate the Gaussian

with a triangle and call the reflection angles to the left and right of the Bragg angle, where no signal is received anymore, $2\theta_1$ and $2\theta_2$ respectively. Then the angular FWHM W for this peak is $W = \theta_2 - \theta_1$. The angles θ_1 and θ_2 are defined by a destructive interference condition. The following is valid:

$$(m + 1)\lambda = 2L \sin \theta_1 \quad \text{and} \quad (m - 1)\lambda = 2L \sin \theta_2. \quad (2.68)$$

Eq. (2.68) describes the Bragg condition for multiple wavelengths for the entire thickness of the epitaxial layer. If there is a pathdifference of one wavelength λ between the first and the last plane of the epitaxial layer, a plane halfway into the layer will have a pathdifference $\lambda/2$ with respect to the first plane. Destructive interference will cancel the two reflections from these planes. The same happens to all other planes. Every plane has a destructive interference “partner” a distance $L/2$ away. This is the destructive interference condition defining the angles θ_1 and θ_2 .

Now we can proceed similarly to the superlattice equation derivation. Subtracting the two equations given by Eq. (2.68) yields

$$\lambda = 2L \cos\left(\frac{\theta_1 + \theta_2}{2}\right) \sin\left(\frac{\theta_1 - \theta_2}{2}\right). \quad (2.69)$$

Using the approximations $\sin[(\theta_1 - \theta_2)/2] = (\theta_1 - \theta_2)/2$ and $\theta_1 + \theta_2 = \theta_B$ gives a first approximation to Scherrer's formula concerning the coherence length of the crystallographic direction defined by the set of planes with Bragg angle θ_B :

$$L = \frac{\lambda}{W \cos \theta_B}. \quad (2.70)$$

A more rigorous approach to the problem will give the result⁴⁹

$$L = \frac{0.94\lambda}{W \cos \theta_B}, \quad (2.71)$$

where L is the coherence length and W is the FWHM of a scan in radians dependent on 2θ . The Scherrer equation may be applied to any peak resulting from the diffraction of the atomic plane spacing, such as a single peak from a homogeneous layer, or the zeroth order peak of a superlattice.

For a single layer diffraction there is no way of distinguishing between plane spacing variations, interdiffusion, and grading. Interdiffusion occurs at layer interfaces and is

activated by high growth temperatures. The sharpness of the interface smears out. Grading means a gradual change in chemical composition from one period of the superlattice to another, as opposed to a perfectly even composition throughout the superlattice.

If grading occurs throughout a superlattice the effect will be seen in the fringes in between the superlattice peaks. Kervarac et al. have given an analytical description of the effect.⁴¹ Secondary superlattice peaks next to the primary superlattice peaks increase in intensity and, for large composition gradients, may reach the same order of magnitude as primary peaks. For low resolution-scans or poor material quality only uniform broadening may be observed.

In Fig 2.11 on p. 41, the scan data shows superlattice peak broadening with increasing superlattice peak order. None of the simulations show this effect. Fewster has shown that the FWHM of superlattice diffraction peaks can be used to estimate the period variation of a superlattice.⁴² Eq. (2.59) may be simplified using the relation

$$\begin{aligned}
 \sin \theta_n - \sin \theta_m &= \sin(\theta_0 + \Delta\theta_n) - \sin(\theta_0 + \Delta\theta_m) \\
 &= 2 \cos\left(\theta_0 + \frac{\Delta\theta_n + \Delta\theta_m}{2}\right) \sin\left(\frac{\Delta\theta_n - \Delta\theta_m}{2}\right) \\
 &\approx \cos \theta_{avg} (\Delta\theta_n - \Delta\theta_m) \\
 &\approx \Delta\theta \cos \theta_{avg}
 \end{aligned} \tag{2.72}$$

where θ_0 is the superlattice Bragg angle and $\Delta\theta = \Delta\theta_n - \Delta\theta_m$ is the angular distance between two superlattice peaks of order n and m . θ_{avg} is the average angle of peaks n and m . The approximation is valid if $\Delta\theta$ is small and peaks n and m are close to the zeroth order peak. Now equation (2.59) can be written as

$$L = \frac{(m - n) \lambda}{\Delta\theta 2 \cos \theta_{avg}} \tag{2.73}$$

This equation may be differentiated to yield the relationship between a period variation δL and the variation of the angular distance between superlattice peaks $\delta(\Delta\theta)$, which relates to the angular variation of any given superlattice peak and therefore constitutes a measure for peak broadening.

$$\delta L = \frac{(m - n) \lambda}{2 \cos \theta_{avg}} \frac{\delta(\Delta\theta)}{(\Delta\theta)^2} \tag{2.74}$$

Relative peak intensities of superlattice peaks of different order may be used to obtain insight about interfacial interdiffusion. No growth process is perfect, and thus

no layer interface is perfectly abrupt. Instead of a rectangular composition change the chemical modulation along the growth direction will be somewhat more sinusoidal. A Fourier series describes the chemical modulation:

$$c(z) = c_0 \left[1 + \sum_m Q_m \cos\left(\frac{2\pi m z}{L}\right) \right]; \quad (2.75)$$

where c denotes the composition, z is the spatial coordinate in growth direction and Q_m stands for the amplitude of the m th harmonic of the Fourier expansion. For the ideal case all Q for even m vanish. Starting with this relation it can be shown using kinematical theory and diffusion laws, that the intensity of the m th order satellite peak is directly correlated to the Fourier coefficient Q_m .⁴³ It follows that, the greater the interdiffusion, the faster higher order superlattice peaks will vanish.

The compositional modulation given by interfacial interdiffusion causes a modulation of structure factors, which in turn causes the impact on peak intensity. In addition, lattice parameters are modulated, contributing to overall broadening and intensity loss. The periodicity of the superlattice is not affected.

2.7 COMPARISON OF KINEMATICAL AND DYNAMICAL SIMULATION

In order to check the validity of the kinematical simulation used, a test against a commercial dynamical simulation program has been performed. Unfortunately, the available commercial program (Philips HRS) only supports cubic crystal structures.⁴⁰

The sample simulated is a MOCVD-grown GaN/InGaN superlattice on sapphire with a GaN buffer layer and an AlN capping layer (Table 2.1, p. 38). The actual structure is wurtzite (hexagonal). If only symmetrical scan simulations are necessary, the similarity of the wurtzite (based on the hexagonal closed packed structure (hcp)) and the Zinc-Blende (based on face centered cubic lattice structure (fcc)) makes it possible to use the cubic simulation [Fig. 2.10, p. 39]. The set of (002) planes of the two interpenetrating hcp lattices creating the wurtzite lattice structure, is equivalent to the set of (333) planes of the two interpenetrating fcc lattices creating the zinc-blende lattice structure. Only the atomic stacking differs (AB double-planes in wurtzite, ABC double-planes in zinc-blende, see Fig. 2.10, p. 39).

	dynamical simulation	kinematical simulation
capping layer	1000Å $\text{Al}_{0.05}\text{Ga}_{0.95}\text{N}$	1000Å $\text{Al}_{0.05}\text{Ga}_{0.95}\text{N}$
SL layer A	50Å GaN	50Å GaN
SL layer B	35Å $\text{In}_{0.2}\text{Ga}_{0.8}\text{N}$	35Å $\text{In}_{0.2}\text{Ga}_{0.8}\text{N}$
periods	12	12
substrate	GaN	GaN
fully strained SL	yes	yes
crystal structure	zinc-blende	wurtzite
set of planes hkl	$(111)_{\text{zinc-blende}}$	$(002)_{\text{wurtzite}}$
lattice constant	$a_{\text{zinc-blende}} = \frac{\sqrt{3}}{2}c_{\text{wurtzite}}$	c_{wurtzite}

TABLE 2.1. *Sample Data Used for Simulation Comparison:* The sample parameters given to the dynamical and kinematical simulation program vary only in the lattice parameter.

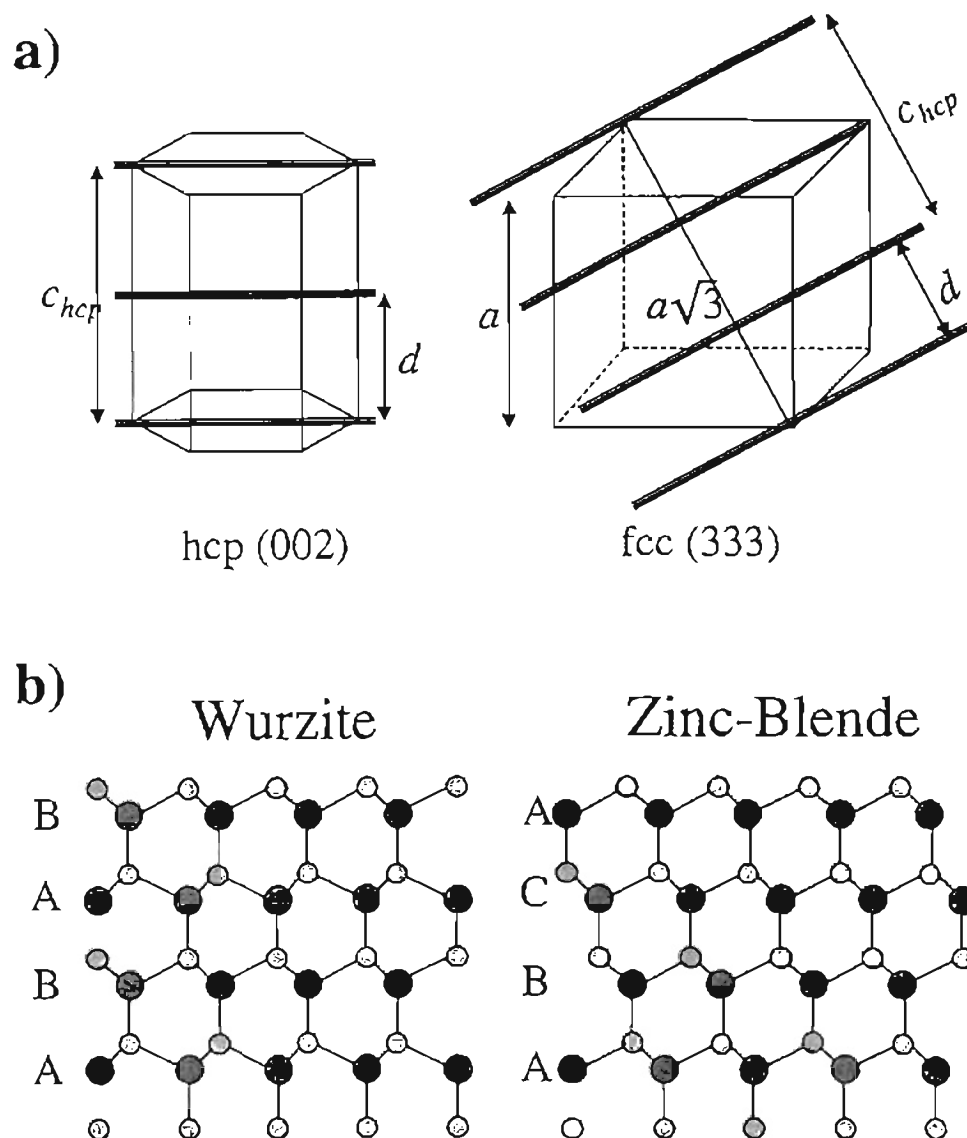


Figure 2.10. *Wurtzite and Zinc-Blende Lattice Structures:* a) In [001] direction the hcp unit cell contains 2 plane spacings, whereas the fcc unit cell contains 3 in [111] direction. To adjust for the different geometries a factor $3/2$ as well as the $\sqrt{3}$ from the cube diagonal have to be included. Hence $a_{\text{zinc-blende}} = (\sqrt{3}/2)c_{\text{wurtzite}}$ is the correct lattice parameter translation. b) ABC stacking for wurtzite double-planes in [001] direction and AB stacking for zinc-blende double-planes in [111] direction.

For a fully strained superlattice, where the planar spacing does not change within the superlattice, one zeroth order peak and a number of weaker satellite peaks are expected (Section 2.5). In addition, we should see signals from the substrate and the capping layer.

Figure 2.11 on p. 41 shows the simulation results. Both the kinematical and the dynamical calculation show the expected result: substrate and capping layer peaks as well as superlattice zeroth order and satellite peaks are displayed. There is virtually no difference in peak positions between the kinematical and the dynamical curve. A slight difference in peak shape is to be expected because secondary scattering, considered in the dynamical approach, will change the phase of reflected beams.

We see that, the higher the superlattice satellite peak order, the smaller the intensity of the peak, as expected. This intensity loss is strongest in the experimental scan, and weakest in the kinematical simulation curve. The experimental scan has a less-than-perfect superlattice structure. Interface roughness broadens higher order satellite peaks. The kinematical simulation assumes a perfect structure and again neglects secondary scattering and absorption effects in the superlattice layers.

The differences mentioned are negligible. Overall the agreement between both simulations is excellent, proving that the used kinematical simulation is adequate for the intended purpose of analyzing the given epitaxial thin film samples.

2.8 SUMMARY

The kinematical and dynamical approaches to the theory of X-ray diffraction from a crystal have been introduced. Additionally, such important concepts as the reciprocal space and stress and strain have been explained. Next, attention was turned to the specific problem of X-ray diffraction from a superlattice. Finally, the kinematical and dynamical theory has been applied to the superlattice in the form of two computer simulations.

For the further development of this thesis it is worthwhile to note a couple of points:

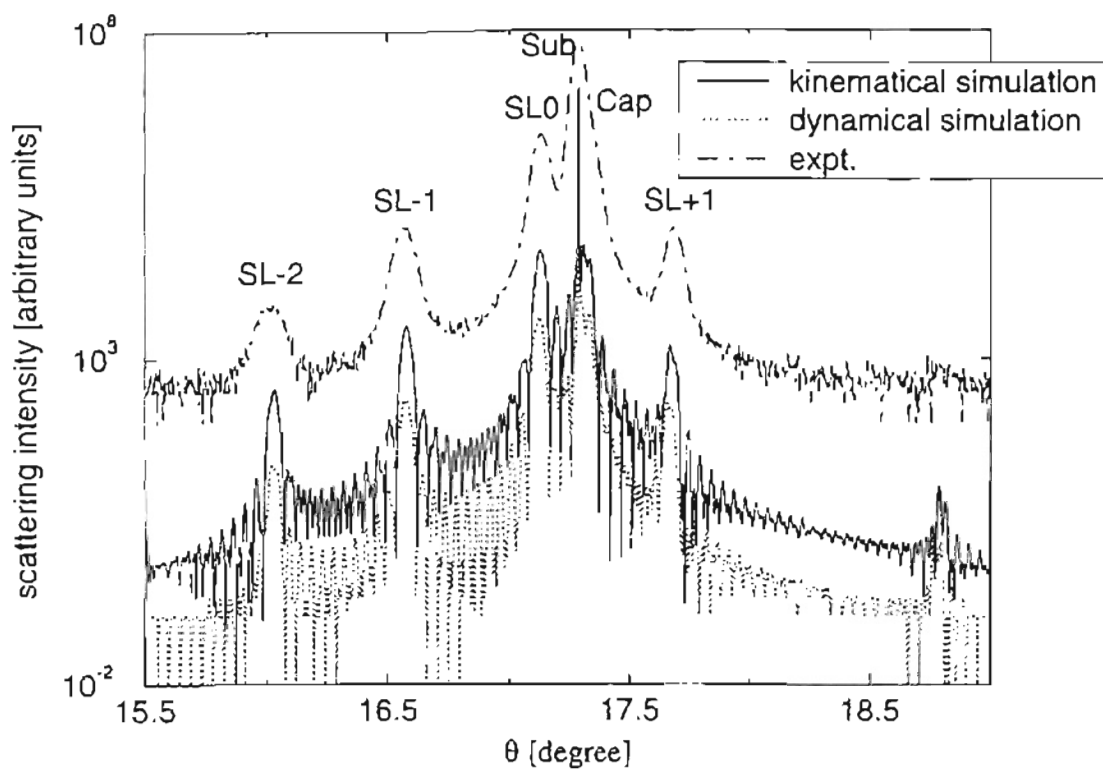


Figure 2.11. *Comparison between Dynamical and Kinematical Simulation:* An GaN/InGaN superlattice X-ray scattering scan and kinematical and dynamical simulations using identical simulation parameters (see table 2.1, p. 38). For clarity, arbitrary intensity offsets have been introduced.

- If the epitaxial layer thickness is small compared to the extinction length, absorption can be neglected and the amplitude of the scattered signal will be proportional to the layer thickness. This is the case for the samples considered in this study. The region of interest in the samples studied lies within $\approx 1\mu m$ from the surface.
- The samples studied in this work show a variety of imperfections. Within imperfect, low quality, crystal structures multiple scattering between Bragg planes is negligible. Constructive interference of such secondary scattered waves is suppressed by lattice irregularities.²⁷ For this reason, it is adequate to use the kinematical simulation, which neglects secondary scattering, for comparison with the experimental scan data.
- The experimental error introduced by crystal imperfections for lattice parameter measurements, exceeds the theoretical error introduced by assuming the vacuum X-ray wavelength within the material using kinematical theory. The index of refraction for X-rays differs for semiconductor materials from unity (vacuum) on the order of 10^{-6} to 10^{-5} .²⁹ Bragg's equation, Eq. (2.1), states that a lattice constant d is proportional to the X-ray wavelength λ . For samples studied here, lattice parameters are known at best to an accuracy of 10^{-3} .

The overall conclusion is that a Single-Scattering approach to model the samples under study is sufficient. Consequently, the kinematical theory has been applied to the X-ray diffraction simulation of the samples considered in this thesis.

CHAPTER 3

DESCRIPTION OF THE EXPERIMENTAL HRXRD SETUP

3.1 OVERVIEW

Experimental techniques for studies on X-ray diffraction have come to maturity at steady pace since their introduction in the second decade of this century. Three principal scattering geometries have been used from the earliest days of X-ray diffraction investigations on [Fig. 3.1, p. 44]. For the first observations in 1912, von Laue used the geometry named in his honor. The incident X-ray beam, a sample, and a photographic plate are lined up, so that diffraction patterns may be recorded on the photographic plate behind the sample.^{21,26} In 1916, Debye and Scherrer developed a cylindrically shaped camera. Placed in the center of the camera a crystal-powder scatters an incident X-ray beam.²⁶ The photographic film covers the full circle. The main feature of this method is that a complete diffraction pattern containing all scattering angles can be observed. As early as 1913 Bragg used a diffractometer setup.²⁶ Its geometry is similar to the Debye-Scherrer camera. A detector is moved on a circle to identify angles of diffraction. Due to the lack of sufficiently high quality detectors at the time, the diffractometer design became popular only much later. In the late 1940's, the first commercially available models became available. Since then, vast improvement of detector accuracy as well as mechanical accuracy have made the diffractometer the most valuable tool in X-ray diffraction research today.

The most widely used kind of diffractometer used today applies the double crystal diffraction (DCD) method invoked first in 1937 by DuMond.⁴⁵ Before the incident X-ray beam hits the sample, it is diffracted by a set of Bragg planes from a high purity Si or Ge crystal. If the system is used in a non-symmetric way, i.e. the two crystals

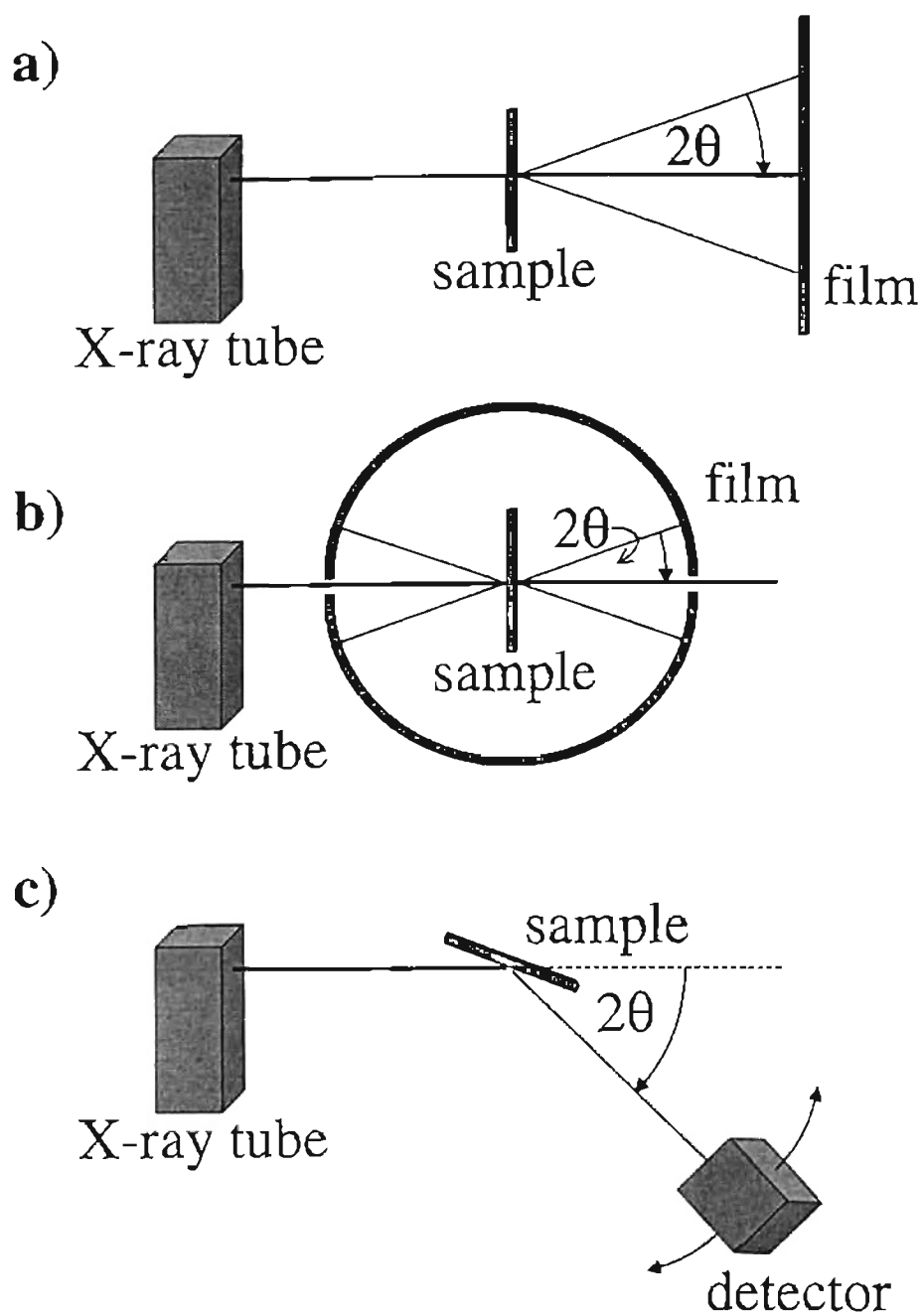


Figure 3.1. *Principal Experimental X-Ray Diffraction Geometries:* a) The von Laue geometry uses a flat photographic film for detection of diffracted X-rays. b) The Debye-Scherrer camera catches all diffraction directions at once. c) This is the basic diffractometer geometry introduced by Bragg.

are not of the same lattice constant and are not tuned for the same set of Bragg planes, different impinging wavelengths will be reflected in different directions. This effect will “filter” the X-ray beam and minimize the wavelength variation $\Delta\lambda$ within the beam. The angular dispersion of the incident beam on the sample can be reduced to have a FWHM of ≈ 10 arcsec for the $\text{CuK}_{\alpha 1}$ line.²⁷ Another, even more powerful device to yield a monochromatic incident beam is a four crystal monochromator first used in 1974 by Beaumont for synchrotron radiation studies.⁴⁶ It has been applied to X-ray diffraction by Bartels in 1983 and is therefore referred to as Bartels monochromator.²⁸ A detailed description is given later in this chapter (it is part of our own X-ray diffraction setup). Using the Bartels monochromator a FWHM of 5 arcsec for the incident beam can be achieved.

In this chapter the specific geometry of the Philips material research diffractometer (MRD), which has been used in this study, will be described. From the experimental setup various possibilities for sample investigations arise. The Ewald construction will aid the imaginative faculty necessary to picture the “mechanics” of reciprocal space. A number of different scans will be introduced, and an interpretation of the data obtained by each scan will be given. Finally, the most powerful experimental tool, as far as X-ray diffraction of epitaxial thin films is concerned, reciprocal space mapping, will be discussed in detail.

3.2 THE PHILIPS MRD SYSTEM

All results presented in this thesis have been obtained by examining data produced by scans done with a recent Philips materials research diffractometer as shown in Fig. 3.2 on p.47. The Philips MRD system consists of the incident beam optics (X-ray tube and monochromator), the waferstage and goniometer, the diffracted beam optics (analyzer and detector), a power supply with cooling unit for the X-ray tube (not shown), and an electronics box controlling the motors which move the waferstage and goniometer (not shown).^{44,48} A standard PC is connected to the system’s electronics. All motor movements, scan setups, and data recording is controlled with the program

PC-MRD provided by Philips.⁴⁴ The following subsections will describe the hardware in detail.

3.2.1 DEGREES OF FREEDOM

The Philips MRD system offers a broad variety of scans due to its flexible setup. There are 7 degrees of freedom when it comes to positioning a sample relative to the incident X-ray beam and the detector [Fig. 3.3, p. 48]. When mounted on the waferstage, the sample may be rotated about and translated along its in-plane axis x and y , and its surface normal, axis z . Additionally, the detector may be rotated according to Fig. 3.1 (c) on p. 44.

The zero position for all angles and axis is given, when the x -bar is oriented horizontally, the y -bar is oriented vertically and, by adjusting the z -axis micrometer screw, half of the incident beam is blocked by the sample surface along the x -axis. The waferstage is not tilted, $\psi = 0$, not rotated about the z -axis, $\phi = 0$, and not rotated about the y -axis, $\omega = 0$. If the detector is centered on the half blocked beam the detector is in zero position also ($2\theta = 0$).

The goniometer consists of the base plate of the system, the ω -drive which turns the waferstage, and the 2θ -drive which moves the 2θ -arm. The 2θ -arm holds the detector. The minimum step size of both drives is 0.0005 degrees (1.8 arcsec). The angular range for 2θ is about 170 degrees.

The waferstage accommodates four different movements. These are the ϕ -rotation about the sample surface normal (z -axis) with a range of ± 178 degrees and 0.01 degrees stepsize, the ψ -tilt with a range of ± 10 degrees and 0.0001 degrees stepsize, and the translations along the x and y bars with a range of ± 75 mm and 0.1 mm stepsize. The waferstage can be moved forward and backward as a whole along the z -axis with a micrometer screw.

All of these motions may be controlled independently, so that a variety of possible scans result, e.g. the ω and 2θ drives may be combined to assume an $\omega/2\theta$ scan, or a scan along a predetermined line in reciprocal space.

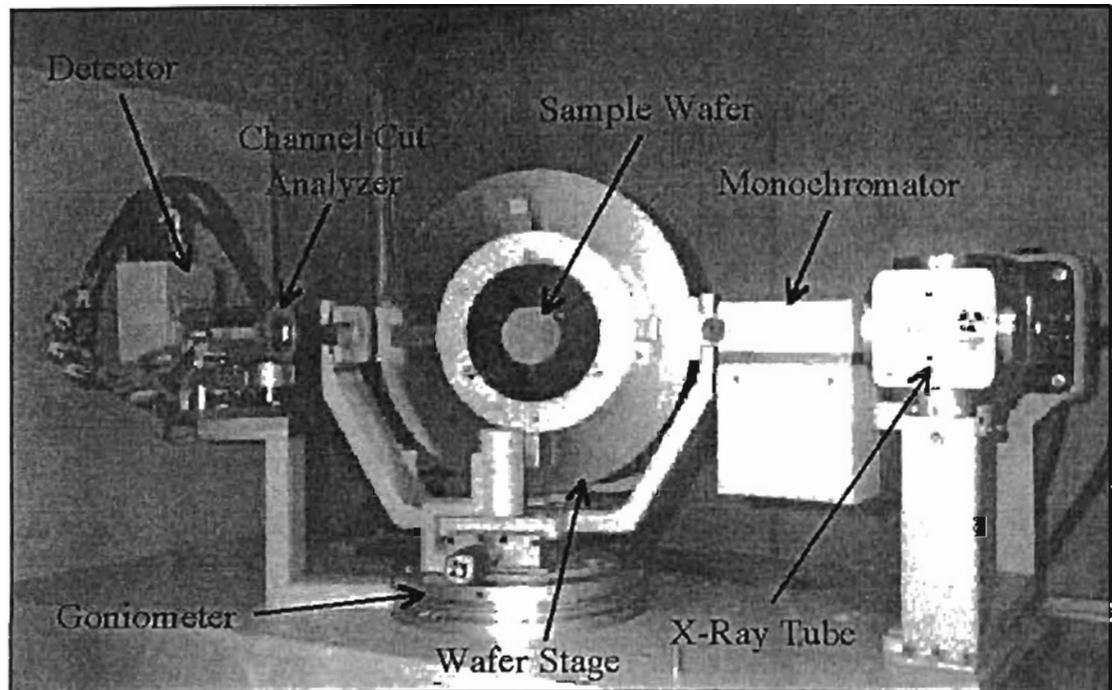


Figure 3.2. *Philips MRD Waferstage*: The goniometer contains the ω and 2θ drives. The waferstage holds motors for two translational and two rotational degrees of freedom. The incident X-ray beam is produced by a Cu X-ray tube. Within the monochromator the Ge crystal orientation may be changed from (220) planes to (440) planes with respect to the incident beam. In order to form a triple axis system, the three-bounce channel-cut Bense-Hart collimator may be positioned in the diffracted beam.

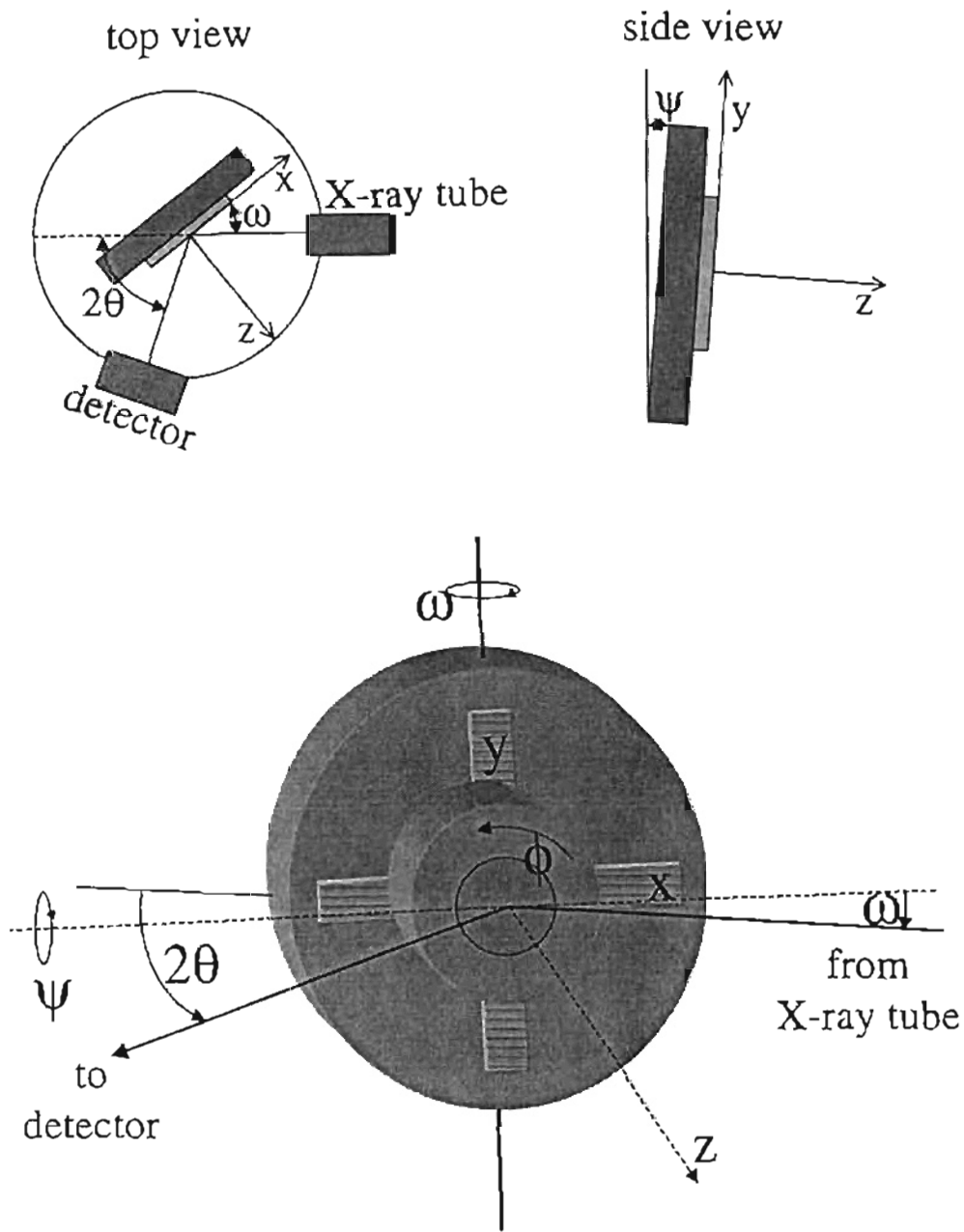


Figure 3.3. *Waferstage Degrees of Freedom*: When the sample is mounted on the waferstage motorized movement is available for two translational axis (x , y), and three rotational axis (ψ , ω , ϕ). The sample may also be moved perpendicular to its surface (z -direction) with a micrometer screw. The detector is positioned independently by changing 2θ .

In order to carry out a scan a sample has to be mounted on the waferstage. If it comes in the form of a wafer up to 5.5 inches in diameter, it can be put directly in place. It is held on the waferstage by three radially movable clamps 120 degrees apart. In case of an irregularly shaped sample, the sample has to be mounted to a circular 2.5 inch diameter metal plate with grease or adhesive tape. The metal plate then is put onto the waferstage as before. The latter mounting technique introduces a significant discrepancy concerning the sample's surface orientation. An additional issue is relaxation of the adhesive during long scans. See Appendix C about alignment procedures.

3.2.2 MRD OPTICS

The incident beam optics comprises the X-ray tube and the four crystal Bartels monochromator. The diffracted beam optics consists of the channel cut analyzer, a slit and the detector.^{44,48}

The X-ray tube is furnished with a Cu anode. The characteristic radiation with wavelength $\lambda = 1.540597\text{\AA}$ used corresponds to the anode's $\text{CuK}_{\alpha 1}$ absorption line. The maximum power setting is 2200 Watts. In order to extend the life of the equipment, all experiments are done at 700 Watts. The X-rays emerge through a 0.4×12 mm slit with an angular spread of 6 degrees. The X-ray bundle then is narrowed by the monochromator.

The Bartels monochromator housing contains two U-shaped Ge crystals. The two reflective shapes seen in Fig. 3.4 on p. 51 on the left within the housing of the Bartels monochromator, represent the top part of one U-shaped Ge crystal, and the two reflective shapes on the right represent the top part of the second Ge crystal. If the Bragg condition for an impinging X-ray wavelength λ is fulfilled on both crystals, the beam will pass the monochromator. For another beam of slightly different wavelength $\lambda + \Delta\lambda$ the deviation from its Bragg angle becomes bigger with every reflection from a set of crystal planes. After four reflections its intensity has diminished drastically. The surfaces of the crystals are cut perpendicular to the crystallographic $[110]$ direction. Rotation of both Ge crystals is motorized. This enables changing of the Bragg angle within the monochromator between the Ge (220) and Ge (440) diffractions for $\text{CuK}_{\alpha 1}$

X-rays. In the (440) setting the beam is almost completely σ -polarized.²⁷ The X-ray beam divergence is cut down to 12 arcsec for the (220) setting and 5 arcsec for the (440) setting. The relative intensity of the beam leaving the monochromator for the (220) setting compared to the (440) setting is 125:1. Considering the reduced initial beam intensity and the quality of Nitride thin films to date, the (220) setting has been used for this study.

The diffraction beam coming from the sample will reach the detector through a simple slit, or, in the triple axis setup*, through the channel cut three-bounce Bonse-Hart analyzer. The detector itself has a circular, 6 mm wide acceptance aperture. It is a proportional counter, proportional up to 500,000 counts per second. At 700 Watts the maximum count rate after passing the monochromator is 340,000 in the actual setup. For slit optics experiments a 0.5 mm slit has been used, corresponding to an acceptance angle of 0.17 degrees for 2θ . The slit cuts back background radiation and limits the sample region of the Ewald sphere (see below).

The analyzer is yet another U-shaped Ge crystal. Again, it is cut along the (110) planes and for the experiment the (220) reflection for $\text{CuK}\alpha_1$ radiation has been used to improve angular resolution. The FWHM of the diffracted beam after passing the three-bounce Bonse-Hart collimator is 12 arcsec.

Two distinct detector optics of the Philips MRD allow the experimenter to choose between high intensity and high accuracy results of a scan. In general, poor structural quality in an epitaxial layer will reduce the diffracted peak intensity and increase the broadness of the diffracted signal. Hence, if poor or mediocre material quality is expected, the slit optics shown in Fig.3.4(a) are chosen. For high quality samples the triple axis setup shown in Fig.3.4(b) will increase accuracy and yield better results. Depending on sample quality an intensity loss of 1-2 orders of magnitude is to be expected when using the three-bounce Bonse-Hart collimator compared to the slit optics.

*It is called triple axis setup because the X-ray beam is reflected three times — in the incident beam optics, at the sample, and in the diffracted beam optics.

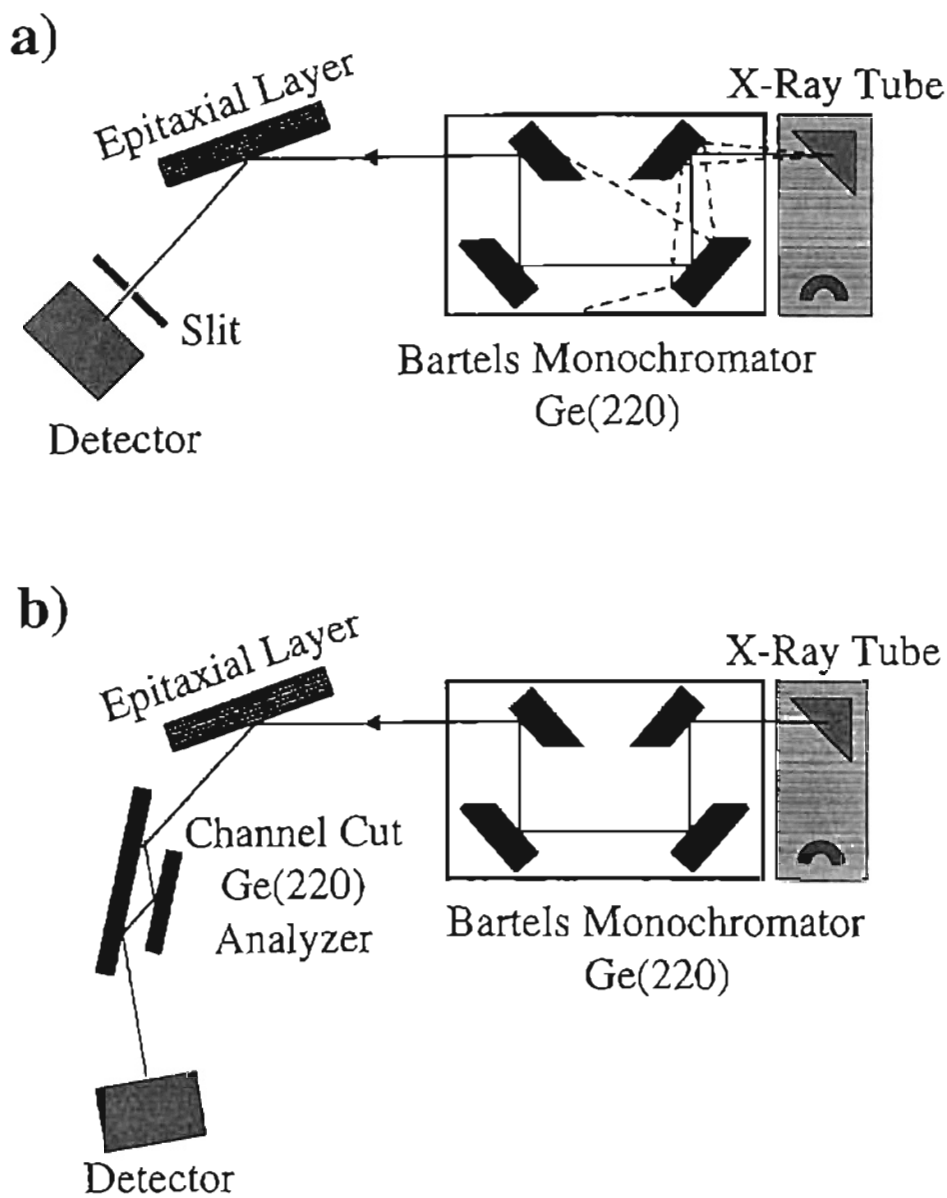


Figure 3.4. *MRD Optics*: a) The slit optics setup will yield high intensity diffracted beam data. b) The triple axis setup increases the angular resolution by inserting the three-bounce Bonse-Hart collimator into the diffracted beam resulting also in significant intensity loss.

3.3 THE EWALD CONSTRUCTION

In order to obtain a better qualitative view on what properties of a crystal are probed by which scan and why, it is necessary to surpass the simple Bragg plane, real space picture, and to employ the reciprocal space construction. The key to the understanding of reciprocal space geometry is the Ewald construction given by Ewald's sphere [Fig. 3.5, p. 53].

Every reciprocal space lattice point corresponds to a real space plane set, the normal of which is the reciprocal lattice vector given by Eq. (2.14) on p. 16. Hence, reciprocal space is a three dimensional space containing as many lattice points as the real space lattice offers sets of planes. For this discussion, let the c -axis of the hexagonal lattice be perpendicular to the sample surface, and the perpendicular a -axis be parallel to the sample surface. This setting defines the usual growth direction for GaN hexagonal thin films, and is valid for all samples to be discussed in the next chapter. Then \vec{G}_{\parallel} defines the reciprocal space direction parallel to the sample surface, along the crystallographic c -axis, and \vec{G}_{\perp} is the direction perpendicular to the sample surface, (compare Fig. 2.5, p. 17).

In Chap. 2, was shown that each reciprocal lattice vector \vec{G} fulfills the diffraction condition for a different set of planes [Eq. (2.16), p. 18]. Let us name each reciprocal space vector by this set of planes (hkl). This means, each reciprocal lattice point is indexed by the integers h , k and l . Ewald's construction is completed by applying the von Laue diffraction condition shown in Fig. 2.3 on p. 14 to reciprocal space with $\vec{G} = \vec{K}$. The Ewald sphere has the radius $|\vec{k}| = |\vec{k}'|$. The tip of \vec{k} is fixed at the origin. Every point on the surface of the Ewald sphere can be interpreted as one possible scattering vector $\vec{K} = \vec{k}' - \vec{k}$. During a scan, the Ewald sphere is rolled about the origin. Whenever the point of the shell defined by $\vec{G} = \vec{K}$ intersects a point of the reciprocal space lattice, defined by \vec{G}_{hkl} , the diffraction condition, $\vec{G} = \vec{G}_{hkl}$, is fulfilled for the respective set of Bragg planes.

Now the angles of the experimental setup have to be considered. The angle between \vec{k} and \vec{k}' must be 2θ ; this is the diffraction condition. The angle between the

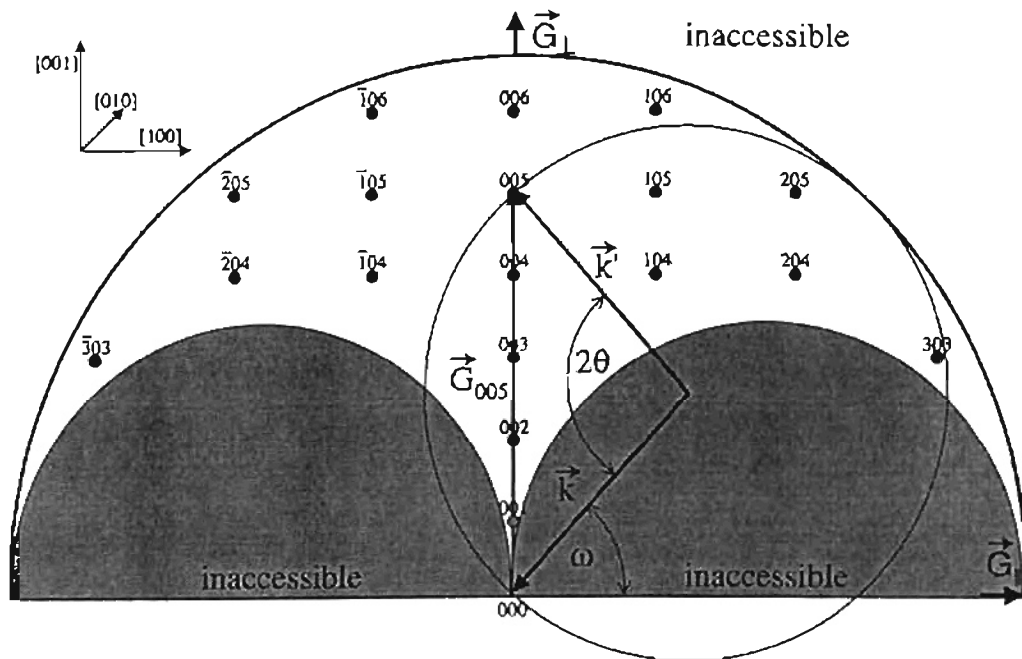


Figure 3.5. *Ewald Sphere and Instrumental Scan Limits:* The Ewald sphere intersects reciprocal lattice point (005). The detector will receive the Bragg reflection of the set of planes (005). The instrumental scan limits defined by the angular ranges of ω , 2θ , and $|\vec{k}|$ are shown for hexagonal GaN with the marked orientation.

incident beam and the planes parallel to the sample surface is ω [Fig. 3.3, p. 48]. This must be the angle between \vec{k} and \vec{G}_{\parallel} . A change in tilt ψ of the waferstage gives an offset between the directions of \vec{G} and \vec{G}_{\perp} . The plane containing the reciprocal lattice points as shown in Fig. 3.5 on p. 53 is rotated about \vec{G}_{\parallel} . Lastly, turning the waferstage about its z -axis changes ϕ and results in a rotation about \vec{G}_{\perp} in reciprocal space. During the mentioned rotations the Ewald sphere is not affected - its movements in reciprocal space only depend on the X-ray beam.

The experimental setup dictates boundaries for sets of planes accessible to the experimenter. In Fig. 3.5 on p. 53 available GaN reciprocal lattice points for the Philips MRD system are shown for the plane spanned by the [001] and [100] crystal lattice directions.⁴⁷ The two half circles are due to the fact that the range of the instrumental angle ω is limited to 90 degrees on either side of the symmetry axis [001]. The radius of the outer half circle is given by the used X-ray wavelength. Bragg's equation states that if the wavelength λ is greater than twice the plane spacing d_{hkl} no reflection is possible. The opening angle of the outer half circle is the instrumental range of 2θ (≈ 170 degrees).

In reality the shell of the Ewald sphere is of finite thickness $\delta(2\pi/\lambda)$ [Fig. 3.6, p. 55]. The deviation $\Delta\lambda/\lambda$ of the incident X-ray beam causes a deviation of the Ewald sphere radius. The acceptance angle of the detector allows for a section of the intersecting Ewald sphere's shell to be sampled. It follows that instead of an intersecting point, there is a sampling volume in reciprocal space defined by the instrumental resolution. By choosing the triple axis optics instead of the slit optics the sampling area is reduced significantly compared to the slit optics.

3.4 BASIC SCAN TYPES

So far only a motionless description of experimental hardware has been given. In order to take a scan, a scan-axis has to be defined, and motion of the apparatus along this axis has to be introduced. Despite having 7 degrees of freedom to choose from, only two of these are commonly used for scans.^{26,27,22,25} While x , y , z , ϕ , and ψ are held fixed, a scan is taken along the ω and/or 2θ scan axis. All the other variables are used

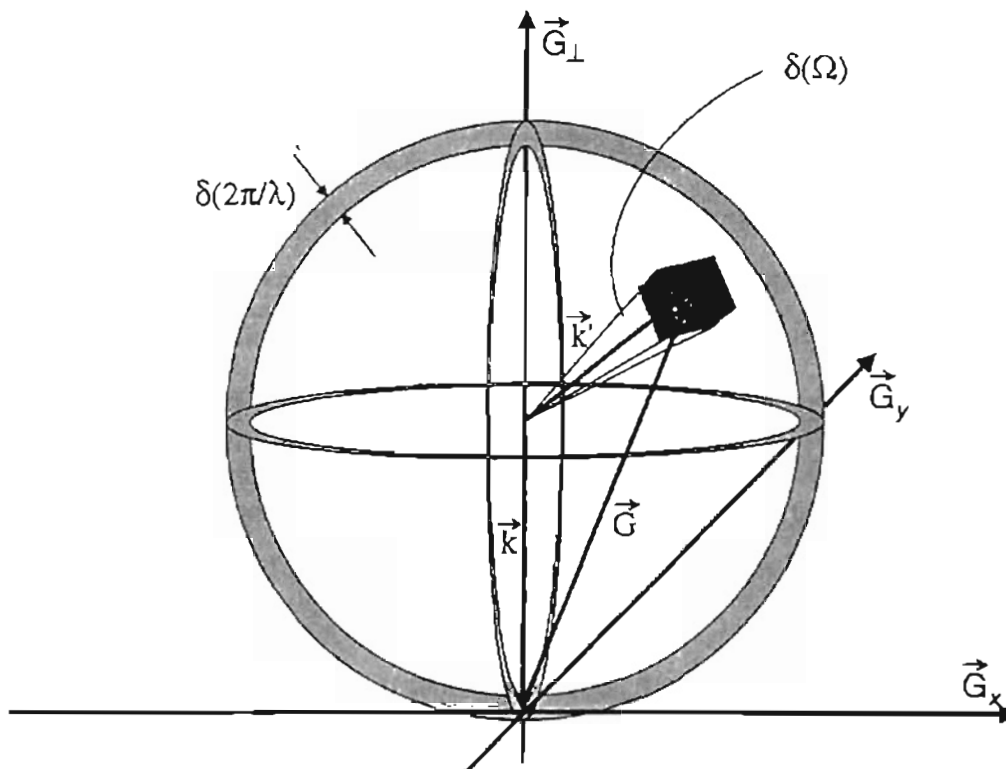


Figure 3.6. *Reciprocal Space Sample Volume*: Within the sample volume the diffraction condition is fulfilled. Incident beam wavelength dispersion causes a length deviation of the Ewald sphere's radius $|\vec{k}| = 2\pi/\lambda$. Angular dispersion causes a directional variation of \vec{k}' . Additionally, the acceptance angle of the detector limits the "seen" solid angle $\delta(\Omega)$.

to arrange the sample's initial orientation and to position it correctly for a scan. With x and y a position on the sample (wafer) is chosen. The angle ψ may be used to correct a mounting tilt offset. For asymmetrical plane sets (hkl) the angle ϕ has to be adjusted.

3.4.1 ω -SCAN

From the earliest publications, so called rocking curves have been used to determine the epitaxial thin film quality of a sample.^{26,22,23} The FWHM of this scan still is the first indicator of the crystalline quality of a grown film.

The real space geometry of the scan is shown in Fig. 3.7 on p. 57. The detector arm is positioned at twice the Bragg angle 2θ , according to the set of planes (hkl) to be scanned. Then the angle ω between sample surface and incident beam is linearly changed — the sample is rotated, it is “rocked” through the incident beam. All the while the detector angle 2θ is held fixed. If the Bragg condition is fulfilled a signal will be recorded.

For a perfect crystal structure the FWHM of the recorded signal should only depend on the thickness of the layer considered. However, in reality a number of defects even within the relatively thin epitaxial films influence the shape of recorded peaks. The ω -scan in particular reveals Bragg plane orientation variations. Since the Bragg condition is held fixed, the rocking of the sample only changes the orientation of a set of planes (hkl) relative to the incident beam. For this set of planes, a certain ω yields constructive interference. If several crystal grains are present in the sample studied, the normal of the set of planes under consideration for each grain will vary. The Bragg condition will be fulfilled for different grains at different angles ω . The recorded peak of the ω scan effectively shows the variation in plane set orientation relative to the sample surface and the respective intensities. The FWHM of this scan is a measure for mosaicity.^{26,27}

The reciprocal space geometry of the scan is shown in Fig. 3.8 on p. 60. The position of the sample volume at the tip of the reciprocal space vector \vec{G}_{hkl} is fixed within the shell of the Ewald sphere relative to the Ewald sphere. Its position is defined by the angle 2θ . Changing the scan angle ω will rotate the Ewald sphere about the origin. The tip of vector \vec{G}_{hkl} describes a circle within a plane defined by the waferstage

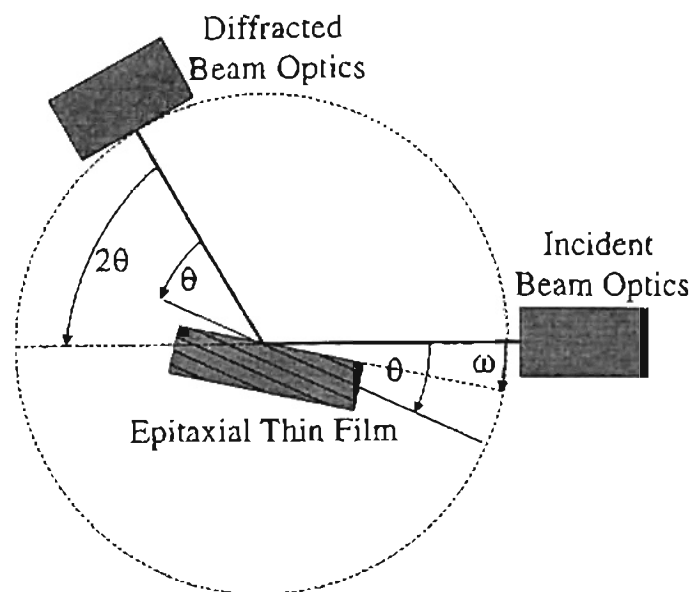


Figure 3.7. ω and $\omega/2\theta$ Scan in Real Space: For an ω -scan 2θ is held fixed according to the Bragg condition for the set of planes under consideration. Then ω is changed in order to find lateral lattice plane misorientations. For the $\omega/2\theta$ -scan again a Bragg condition is chosen, but this time both angles are changed. The detector turns twice as fast as the sample to “tune” through different diffraction conditions for the same plane orientation. Information about plane spacing variation is obtained.

orientation angles ϕ and ψ . The tail of \vec{G}_{hkl} is fixed at the origin. The length and position of the section of the circle to be sampled depends on the range and position of the scan angle ω . If a reciprocal lattice point is encountered on this circle section, a diffracted signal is recorded by the detector.

For an ideal, infinite crystal every reciprocal lattice point is a point. For a non-ideal crystal the reciprocal lattice points become reciprocal lattice features of finite size. For a real crystal, the ideal point has to be convolved with a Fourier transform describing the finite thickness of the sample and a Fourier transform describing the mosaicity of the sample. Further convolutions would include plane spacing variations and for multilayered samples convolutions describing the sample structure (as indicated for a superlattice below in Sect. 3.5). The shape of the reciprocal lattice features then depends on the various transformations. If the sample under study shows mosaicity, an elongation of the reciprocal lattice feature (hkl) allows for a number of reciprocal space vectors to fulfill the diffraction condition while the scan proceeds along the ω -scan-axis (a circle centered at the origin). Hence, the width of a reciprocal lattice feature along the ω -scan-axis is a measure of the mosaicity of the sample with respect to the according set of Bragg planes.

3.4.2 $\omega/2\theta$ -SCAN

The second scan important to epitaxial thin film characterization is the $\omega/2\theta$ - or, for symmetrical scan-axis, $\theta/2\theta$ -scan. If the set of planes under consideration is parallel to the sample surface the angles ω and θ must be identical to fulfill the diffraction condition.

For the $\omega/2\theta$ -scan it is necessary to have a small reception angle at the detector in order to obtain meaningful results. Thus, a fine slit or the triple axis setup is appropriate. The real space geometry of the scan setup is given again by Fig. 3.7 on p. 57. For this scan the sample and the detector are moved at the same time. The angular velocity of the detector arm is twice the angular velocity of the sample. The diffraction angle θ within the Bragg condition $\lambda = 2d \sin \theta$ then changes evenly for a chosen set of planes. The diffraction condition is “tuned” through different plane spacings d .

The sample is tested for the diffraction condition for a range of potential Bragg angles. The intensity reflected for a “tuned” d is proportional to the number of planes featuring this spacing. The FWHM of the resulting curve is a measure of the variation of planar spacing for the planes (hkl) considered.

The reciprocal space geometry for the $\omega/2\theta$ -scan is shown again by Fig. 3.8 on p. 60. If the angle 2θ changes twice as fast as ω does, the tip of the scattering vector \vec{G} will move along a straight line through the origin. In other words, the length of \vec{G} varies. Reciprocal lattice features are sampled by the sampling volume of the Ewald sphere along a radial beam.

Let us inspect the diffraction condition for the scattering vector, $\exp(i\vec{G} \cdot \vec{d}) = 1$ [Eq. (2.10), p. 13], where \vec{d} denotes the orientation and spacing of a chosen set of planes. In order to keep the diffraction condition fulfilled, a change in $|\vec{G}|$ has to be compensated by an appropriate change in $|\vec{d}|$, thereby proving that the $\omega/2\theta$ -scan probes a chosen set of planes (hkl) for its spacing deviation Δd_{hkl} . It can be concluded that the radial elongation of reciprocal lattice points is directly related to the distribution of interplanar spacings.^{26,27}

3.4.3 ϕ -SCAN

One last single scan-axis experiment shall be introduced here. The ϕ -scan is useful to determine the in-plane lattice orientation of an epitaxial layer relative to the substrate, or relative to a second epitaxial layer. C. Lee et al. presented the according scan for GaN on sapphire.⁵⁶

During a ϕ -scan the sample is rotated about the z -axis, perpendicular to the sample surface [Fig. 3.3, p. 48]. Let us consider a hexagonal epitaxial layer where the crystallographic (001)-direction coincides with the axis of ϕ rotation. For a symmetric reflection, the positioning of ϕ is irrelevant. This is not so for off-axis scans concerning asymmetrical plane sets.

To further elucidate the situation let us consider the set of planes with Miller indices $(hkl)=(100)$. A glance at the unit cell for a material with a one atom basis [Fig. 2.5, p. 17] shows a six-fold symmetry for this set of planes. Equivalent sets are

(110), (010), ($\bar{1}00$), ($\bar{1}\bar{1}0$), and (0 $\bar{1}0$). If the Bragg condition for one of these plane sets is fulfilled, a ϕ -scan can be performed. If ϕ goes through its full 360 degree range six peaks for six equivalent plane sets should show up 60 degrees apart from one another. Now a second 360 degree scan may be performed, only this time the Bragg condition for the corresponding substrate diffractions is fulfilled. If the substrate is hexagonal, as it is for the samples considered in this thesis, the substrate peak positions relative to the film peak positions reveal a rotational in-plane fit or misfit between the different layers and so gives a valuable hint if or if not the epitaxial layer continues the substrate lattice structure.

3.5 RECIPROCAL SPACE MAPS

By virtue of combining the basic ω and $\omega/2\theta$ scans a two-dimensional reciprocal space map can be obtained. Such a reciprocal space intensity contour plot gives a much more complete picture of sample properties than either one-dimensional scan could provide. Information about strain and mosaicity, and, in case of a superlattice, interface roughness and period fluctuation can easily be extracted from a reciprocal space map.

3.5.1 SINGLE LAYER RECIPROCAL SPACE MAP

A reciprocal space map is obtained by executing a series of $\omega/2\theta$ -scans, where in-between each run an offset $\Delta\omega$ is added to ω , thus the $\omega/2\theta$ and ω scans are performed simultaneously, covering a predetermined area in reciprocal space as shown in Fig. 3.9 on p. 62. The plane containing the sampled area is defined by the waferstage angles ϕ and ψ . With $|\bar{k}| = 2\pi/\lambda$ the translation from scan angles to reciprocal space coordinates can be obtained from Fig. 3.9 as

$$|G_{\parallel}| = \frac{4\pi}{\lambda} \sin \theta \sin(\theta - \omega) \quad \text{and} \quad |G_{\perp}| = \frac{4\pi}{\lambda} \sin \theta \cos(\theta - \omega). \quad (3.1)$$

Taking a two-dimensional scan is quite time consuming. Mapping of only one reciprocal lattice point with a reasonable resolution (triple axis optics is a necessity) can

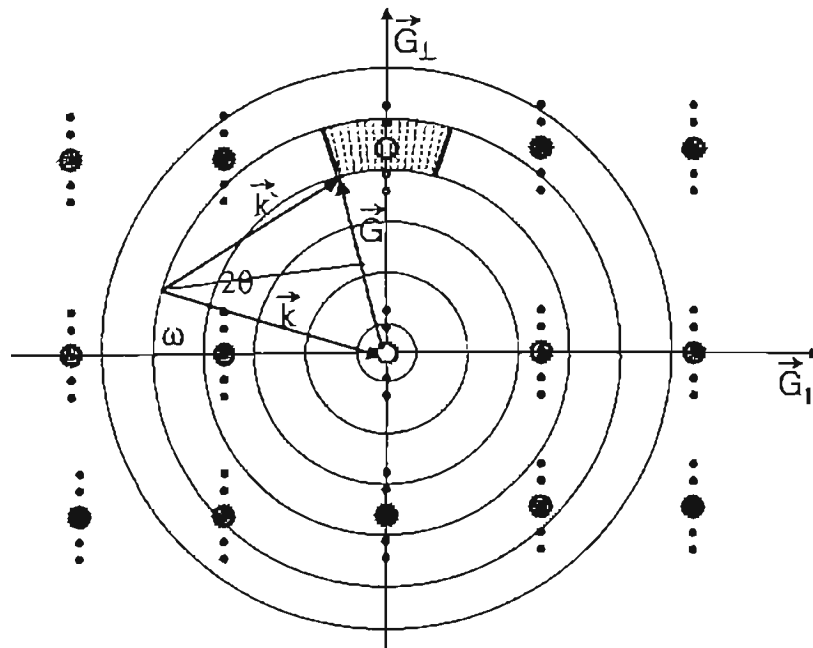


Figure 3.9. *Reciprocal Space Map Scan:* The RSM-scan consists of a number of $\omega/2\theta$ -scans along a radial line originating at the origin, successive increments in ω , which introduces a circular movement. In this manner the indicated area is “mapped”.

take up to 24 hours, even more if substrate and epitaxial layer, or superlattice peaks, have to be considered.*

The reciprocal space map of a single material sample shows one reciprocal lattice feature for each set of planes. As shown in the previous section, elongation along the ω -scan direction is related lateral tilt, and elongation along the $\omega/2\theta$ -scan direction is related to a variation of the planar spacing. The reciprocal space map of a substrate plus epitaxial layer, for similar lattice constants of substrate material and film material (such as ZnO and GaN), will show two reciprocal lattice features per set of planes (hkl). The reciprocal lattice coordinates $|\vec{G}_{\perp hkl}|$ and $|\vec{G}_{\parallel hkl}|$ of a given reciprocal lattice point (hkl) are inversely proportional to the lattice constants c and a of the hexagonal lattice,

$$|\vec{G}_{\perp hkl}| = \frac{2\pi}{c} l \quad \text{and} \quad |\vec{G}_{\parallel hkl}| = \frac{4\pi}{\sqrt{3}a} \sqrt{h^2 + hk + k^2}, \quad (3.2)$$

derived from Eq. (2.17) on p. 18 using $|\vec{G}|^2 = |\vec{G}_{\perp}|^2 + |\vec{G}_{\parallel}|^2$, and $2\pi/|\vec{G}_{hkl}| = d_{hkl}$. The absolute values for the \vec{G} 's above are known from the scan. The strain state of the epitaxial layer now can be determined considering the equations derived in Chap. 2. Shown in Fig. 3.10 on p. 64 is the effect of strain on reciprocal space points. In the fully strained case, the points line up vertically because their in-plane lattice parameters are identical. The distance between points belonging to the same reflection (hkl) increases with increasing l because an inverse multiple of lattice parameter c is added from point to point. For the relaxed case points belonging to the same reflection line up in $\omega/2\theta$ -scan direction. This is due to the fact that the lined up points represent the same Miller indices (hkl) for slightly mismatched lattices. The difference is a variation in the respective plane spacing d . The same principle applied before to the elongation of single reciprocal space points.

3.5.2 SUPERLATTICE RECIPROCAL SPACE MAP

Let us now consider a superlattice diffraction pattern, scanned and processed to yield a two-dimensional reciprocal space intensity contour map. All scan interpretations

*Superlattice reciprocal space scans taken for this thesis took between 20 and 72 hours.

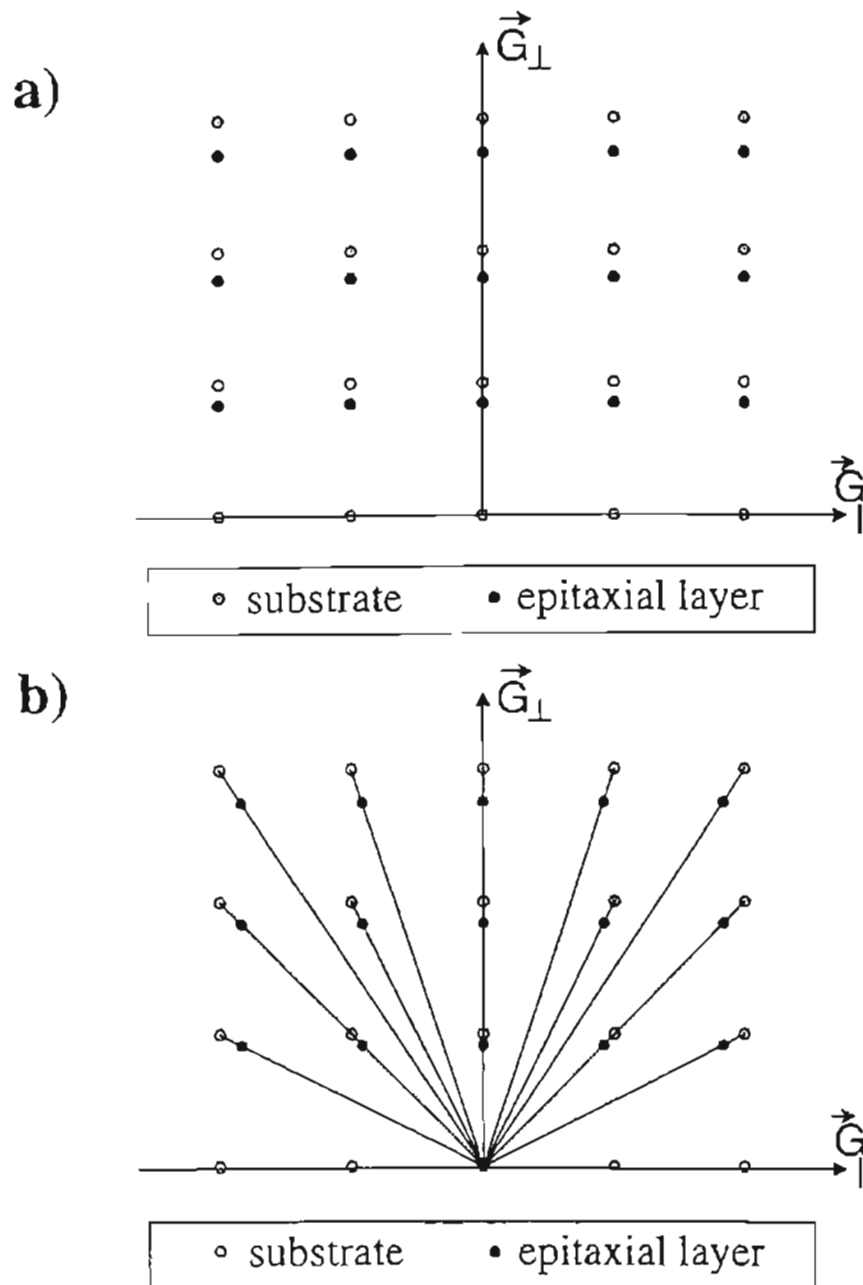


Figure 3.10. *Strain in Reciprocal Space*: The shown example assumes that the lattice parameters for the epitaxial thin film are bigger than those for the substrate. a) Fully strained case: Film and substrate have the same in-plane lattice parameter $a_{\text{substrate}} = a_{\text{film}}$. b) Relaxed case: Neither lattice parameter matches. The points are lined up in radial direction because the substrate and layer points represent the same set of planes (hkl).

mentioned so far may be applied to such a map. The zeroth order peak of the superlattice diffraction pattern takes on the role of a single material reciprocal lattice point. Its satellite peaks can be interpreted similarly to the epitaxial layer discussed above.

Interface roughness between the layers of the superlattice is similar to mosaicity in a bulk crystal. There is no one "smooth" atomic layer of one material and then one atomic layer of the next separating the layers. Instead, there are mosaic like areas of "smooth" contact next to each other, with breaks between them. This makes the superlattice peaks behave like they were experiencing mosaicity. The satellites are broadened horizontally [Fig. 3.11 (a) on p. 66]. The more so, the higher the superlattice peak order. Because interface roughness is not an effect originating from the lattice planes (hkl), the zeroth order peak is not affected.

Lattice parameter deviation within the superlattice affect the various plane spacings for different reciprocal lattice points. All peaks of a superlattice diffraction pattern show the same behavior as a single material reciprocal lattice point would. The peaks are elongated along the $\omega/2\theta$ -scan direction by an amount related to the distance from the origin [Fig. 3.11 (c) on p. 66].

The effect on the superlattice peaks is different when the period of the superlattice fluctuates. Now only the satellite peaks are affected. The satellite peaks for all reciprocal lattice points appear elongated along the \tilde{G}_{\perp} -direction. The higher the superlattice peak order, the broader the peak. This is shown in Fig. 3.11 (b) on p. 66.

If inter-diffusion occurs the intensities of satellite peaks decrease with increasing superlattice peak order. The superlattice period remains well defined as layer interfaces smear out. The zeroth order peak remains unaffected.

In analogy to a single point, mosaicity of the crystal structure is seen as an elongation of all superlattice reciprocal lattice points in ω -scan direction. This is shown in Fig. 3.11 (d) on p. 66. The further out the reciprocal lattice point, the stronger is the ω -spread effect since not the absolute width of the diffracted signal, but the angular density of the diffracted beam, as seen by the Ewald sphere, is concerned.

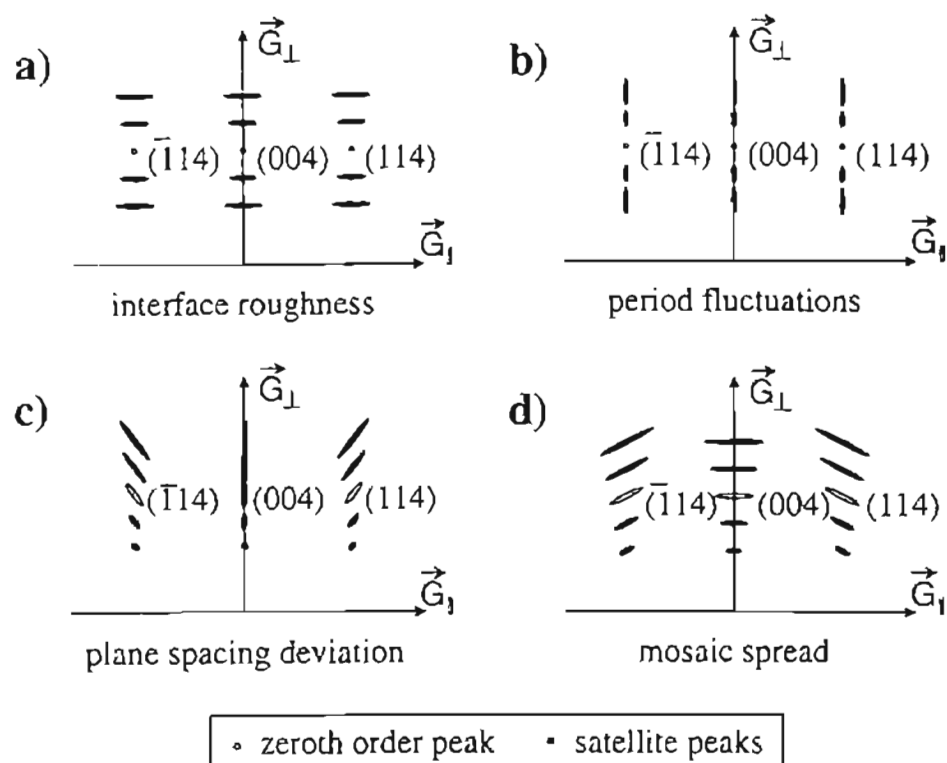


Figure 3.11. *Superlattice in Reciprocal Space*: Shown are superlattice diffraction peaks from zeroth to \pm second order in reciprocal space for the three plane sets $(\bar{1}14)$, (004) , and (114) . No substrate reciprocal lattice point is shown. The diffraction pattern is affected differently by underlying physical effects. In a real reciprocal space map a superposition of all effects shown will occur.

3.6 SUMMARY

The experimental X-ray diffraction geometry has been introduced. The Philips MRD system has been described and its applicability for the studies at hand has been shown. Furthermore, the important concept of the Ewald construction has been explained and applied to standardized scans, such as the ω -scan (rocking curve) and the $\omega/2\theta$ -scan. The last part of the chapter has dealt with the interpretation of reciprocal map scans. In particular, it has been explained what information can be gained from superlattice reciprocal map scans.

The experiment and the underlying theory are now explained to an extent that X-ray diffraction results obtained by different scans of a variety of different samples can now be presented and interpreted; this will be done in the next chapter.

CHAPTER 4

HRXRD APPLIED TO THE STUDY OF GaN-BASED HETEROSTRUCTURES

4.1 OVERVIEW

The previous chapters built the theoretical and experimental foundation needed for the studies conducted on various GaN and InGaN semiconductor samples. All scans performed with these semiconductor samples are commonly used today throughout the scientific community working on the characterization of epitaxial thin films.

Epitaxial thin films can be produced by a number of techniques, such as chemical vapor deposition (CVD), molecular beam epitaxy (MBE), and liquid phase epitaxy (LPE). The latter technique, LPE, has been applied successfully to the growth of GaAs laser diodes.⁵⁰ However, for GaN structures, variations of MBE and CVD techniques have been more successful so far. The samples studied here have been grown using radio frequency plasma assisted molecular beam epitaxy (RF-MBE) and metal organic chemical vapor deposition (MOCVD).

Fig. 4.1 shows the physical structures of the samples studied. In the subsequent sections of this chapter experiments performed, and results found on each sample species are given. The first kind of epitaxial thin film investigated is a single GaN layer on an Al₂O₃ (sapphire) substrate. The samples of this set were grown by RF-MBE at the Oklahoma State University by M. L. O'Steen and R. J. Hauenstein. The GaN on sapphire single layer samples have been produced using an exhaustive variety of growth parameters. The GaN layer quality dependence on different growth parameters will be shown. A small number of GaN on ZnO samples, also grown by M. L. O'Steen and R. J. Hauenstein, have been studied as well. The GaN film exhibits a tilt relative to its ZnO substrate. It will be seen that ZnO is an inferior substrate compared to sapphire at this time. The general layout of the samples is shown in Fig. 4.1 (a).

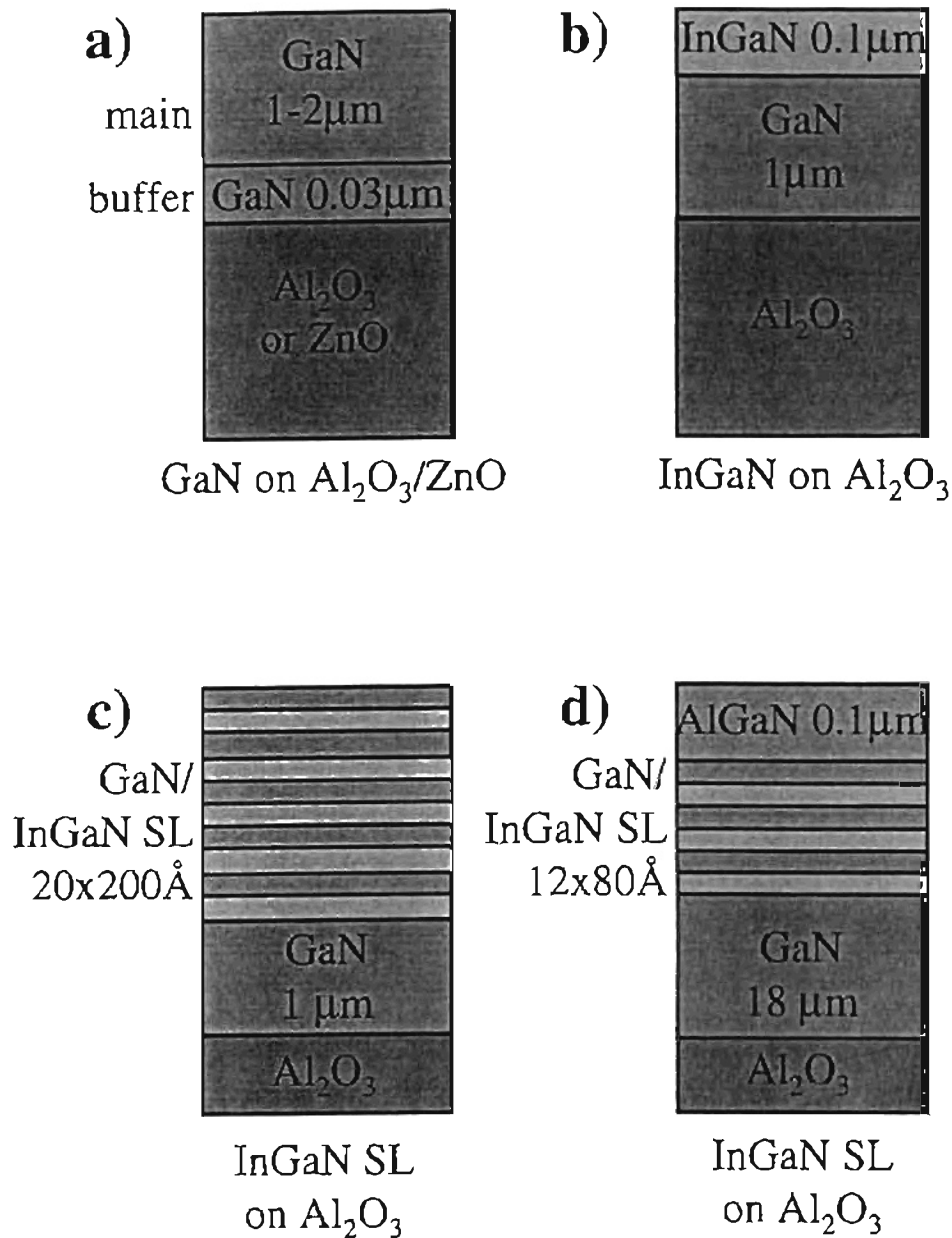


Figure 4.1. *Structure of Samples Studied:* Five different sets of samples have been investigated; a) MBE grown single layer GaN on sapphire or ZnO with GaN buffer layer from OSU, b) MOCVD-grown single layer InGaN on sapphire with GaN buffer layer from EMCORE, c) MBE-grown InGaN superlattice on sapphire with GaN buffer layer, and d) MOCVD-grown InGaN superlattice on sapphire with GaN buffer layer and AlGaN capping layer.

A set of InGaN samples grown using the MOCVD technique by Z. C. Feng at EMCORE corporation shows varying alloy composition. The InGaN Bragg peak shift due to a change in chemical composition is readily observed. The general structure can be reviewed in Fig. 4.1 (b).

From the University of California, Santa Barbara, a set of InGaN/GaN superlattice samples grown utilizing MOCVD by S. Keller, U. K. Mishra, and S. P. DenBaars has been studied. These samples differ in the amount of Si doping given during superlattice growth [Fig. 4.1 (c)]. The results obtained for HRXRD studies on these samples are among the very first to confirm that the superlattice interface quality depends on the amount of a dopant.

Finally, another set of InGaN/GaN superlattices, these without any dopant, has been investigated. These samples, again, were grown by RF-MBE at the Oklahoma State University by M. L. O'Steen and R. J. Hauenstein [Fig. 4.1 (d)]. For the first time InGaN superlattices have been grown successfully at the Oklahoma State University.

Table 4.1 on p. 71 shows a summary of samples studied. The data on MBE-grown GaN single layer samples is presented in table 4.1 (a). The three MOCVD-grown InGaN samples are summarized with table 4.1 (c), and finally, data on MOCVD-grown MQW samples is shown in table 4.1 (b). Each set of samples will be described independently with cross-references to another set where suitable. The order of discussion is given by the chronological development of the HRXRD studies conducted. It will become clear during the presentation of the findings of this study that HRXRD is one of the most useful tools available for studying epitaxial thin films.

4.2 MBE-GROWN GaN ON Al_2O_3

A large number of GaN on Al_2O_3 samples has been grown, and a lot has been learned about the influence of different growth parameters on structural, epitaxial film quality and the respective growth kinetics. We shall focus here on the information ascertainable by HRXRD. Findings from other experiments performed on the same set of samples, such as reflection high energy electron diffraction (RHEED) and photo luminescence (PL), will be reported elsewhere.⁵¹

a)

Sample no.	Growth Parameters							Film	XRD		
	Substrate	Buffer T [C]	Layer T [C]	RF Power [W]	Press N2 (1e-5 Torr)	T_Ga [C]	Dep Time (h)	Thickness [μm]	FWHM_z (arcsec)	FWHM_x (arcsec)	
os96.033	Al ₂ O ₃	482	754	500.0	5.0	1120	1.53	1.21	246	1192	
os97.001	Al ₂ O ₃	585	754	500.0	5.0	1120	1.58	1.35	254	825	
os97.003	Al ₂ O ₃	679	754	500.0	5.0	1120	1.5	1.3	225	360	
os97.004	Al ₂ O ₃	732	754	500.0	5.0	1120	1.5	1.26	93 (36)	104 (97)	
os97.005	Al ₂ O ₃	734	—	400.0	2.0	920	1.08	—	—	—	
os97.028	ZnO	—	490	670	500.0	5.0	1025	2.83	1.69	251	1670
os98.002	Al ₂ O ₃	N/A	730	500.0	5.0	1078	1.4	—	(23)	100 (63)	

b)

Sample no.	Si doping (cm ⁻³)	In Comp. (%)	GaN FWHM_z (arcsec)	SL 0 FWHM_z (arcsec)	SL -1 FWHM_z (arcsec)	SL -2 FWHM_z (arcsec)	SL-period (Å)
961126IA	1 10 ¹⁷	5.08	168	219	312	589	86
9611211C	2 10 ¹⁸	5.00	173	229	276	335	80
9611281D	3 10 ¹⁹	4.70	166	227	212	234	85

c)

Sample no.	Film Thickness (μm)	In Comp. (%)	GaN FWHM_z (arcsec)
N703	1.1	6.3	211
N800	1.3	11.0	208
N813	1.4	17.3	251

TABLE 4.1. *Sample Overview:* The different sets of samples studied are categorized as a) MBE-grown single layer GaN on sapphire or ZnO with GaN buffer layer from OSU, b) MOCVD-grown InGaN/GaN MQW with GaN buffer layer and AlGaIn capping layer from UCSB, and c) MOCVD-grown single layer InGaIn on sapphire with GaN buffer layer from EMCORE. The FWHM z data refers to an $\omega/2\theta$ -scan, while the FWHM x data refers to ω -scans. Values in brackets represent triple axis scans. All other scans have been taken using slit optics.

4.2.1 MBE GROWTH PROCESS

Let us briefly visit the basic ideas and principles concerning MBE growth. This will yield an understanding regarding which growth parameters are important to epitaxial material quality in general, and to GaN growth in particular. The next subsection then will relate growth parameters and HRXRD experimental results.

The single layer GaN samples considered in this thesis have been grown in a Perkin-Elmer 433R MBE system. In a simplified description the system consists of an ultra high vacuum (UHV) chamber with attached conventional effusion (Knudsen) cells containing the source materials, such as Ga and In. The cells are fitted with heater coils, which heat up the source materials and create a material flux out of the Knudsen cells according to the material's vapor pressure. A radio-frequency (RF) plasma source ionizes N_2 gas and so supplies a steady nitrogen flux into the UHV-chamber. Remotely controlled shutters may or may not block the line-of-sight between the source openings and the wafer, thereby allowing only the intended elements to be incident on the heated substrate wafer.

On the surface of the substrate, the atoms of the molecular beams stick with a certain efficiency dependent on the material, the wafer stage temperature, and the kinetic energy of the incoming particles. The wafer heater should provide enough energy for the atoms to roam around the wafer surface, in order to find a reaction partner and the thermodynamically lowest free energy state for the system, but not so much energy as to re-evaporate the incident atoms. Thermodynamics then dictates that the deposited material on the wafer assumes its lowest energy state. If the growth conditions are chosen correctly, the lowest energy state will be the crystal lattice determined by the substrate. Molecules on the surface will minimize their free energy by reconstruction. Their electronic shells will overlap, but in a way which leaves the surface atoms in a higher energy state than bulk atoms. For this reason the surface area is minimized. The epitaxial thin film will grow layer by layer.

From this description, one can see the inter-dependence of various growth parameters. The realization of a perfect lattice without defects certainly depends on the material

ratio and the temperature on the surface of the wafer. In our case, it depends on the Ga to N ratio. The material ratio depends on the incident fluxes and sticking coefficients for each material. The fluxes in turn depend on the source effusion cell temperature. The sticking coefficients depend on the substrate temperature, surface coverage, and material stoichiometry at the surface.

All samples under consideration have been grown on (001) sapphire. The growth direction perpendicular to the sample surface therefore is [001]. Due to the immense lattice mismatch between GaN and sapphire, 67%, the GaN lattice rotates itself by 30 degrees with respect to the underlying sapphire lattice. This has been indicated before in Fig 2.8 (c) on p. 28. With this 'trick' of nature the lattice mismatch is reduced to 16%. This is still a stretch, but during the growth process the mismatch is, at least ideally, minimized due to thermal expansion.

The general layout of all GaN on sapphire samples studied is identical and has been introduced already [Fig 4.1 (a), p. 69]. The samples differ in a number of key growth parameters: buffer layer temperature and main layer temperature, both given by the waferstage temperature during their respective growths, deposition times, and, of course, the fluxes of the source materials. A great variety of samples result. Every single one is contributing to the search for the optimal growth conditions in the MBE UHV-chamber.

4.2.2 ROCKING CURVES

The first scan taken from any given sample is a rocking curve. With this scan in a matter of minutes the experimentator gets a rough idea about the overall epitaxial thin film crystal quality.

It has become customary in recent years to indicate the thin film overall quality by measuring the full width at half maximum (FWHM) of the rocking curve for a certain (material dependent) set of Bragg planes. For GaN epitaxial thin films, this is the (002) plane set. It yields the strongest diffraction peak of the lattice. Fig. 4.2 on p. 75 shows the result of a typical scan from a GaN thin film on sapphire. In the given example the FWHM is 376 arcsec for the ω -scan. The complementary $\omega/2\theta$ scan exhibits a

FWHM of 28 arcsec. Both scans have been executed using the triple axis optics to obtain the highest possible angular accuracy. If the Scherrer approximation for the coherence length [Eq. 2.71, p. 35] is applied to the $\omega/2\theta$ -scan result, one finds the coherence length in growth direction to be $1.1\ \mu\text{m}$. This is on the same order of magnitude as the total thickness of this particular film ($2.6\ \mu\text{m}$). The vertical order of the lattice therefore is excellent.

Note that with these two quick scans the reciprocal space lattice feature, in principle, is already mapped out, if the scan calibration has been done correctly (the two maxima have to coincide to ensure positioning at the center of the reciprocal lattice feature). In the case at hand, since this is a scan of a symmetrical reciprocal lattice feature, we see a pronounced broadening of the reciprocal lattice feature in G_{\parallel} -direction (ω -scan, Fig. 4.2 on p. 75) indicating mosaicity of the film. The very narrow $\omega/2\theta$ -scan on the other hand leads to the conclusion that the stacking of Bragg planes parallel to the surface of the sample is highly homogeneous. The plane spacing d_{002} does not vary much. Both peaks can be called symmetric about their maximum. The intensity distribution about the maximum angle corresponds to a statistical variation in the plane spacing.

The highly organized state of the epitaxial film in growth direction and the in-plane mosaicity of the sample suggest a column growth of GaN on sapphire. We find well defined columns of large coherence length in $[001]$ -direction and a comparatively small diameter in in-plane direction. In order to check the in-plane coherence length directly, a scan of a reciprocal lattice feature on the G_{\parallel} -axis would have to be performed. The broadening of the peak would indicate the diameter of the columns. Unfortunately, this is not an option because of the limited instrumental range [Fig. 3.5, p. 53].

4.2.3 RECIPROCAL SPACE MAPS

The lattice mismatch between GaN and its substrate sapphire is, as mentioned above, 16% in-plane. This difference makes it a very questionable task to find strain relations from a single reciprocal map scan as indicated by Fig. 3.10 on p. 64. The lattice features simply are too far apart. Nevertheless, it is worthwhile to have a look at the shape of the reciprocal lattice features of the epitaxial film and its substrate.

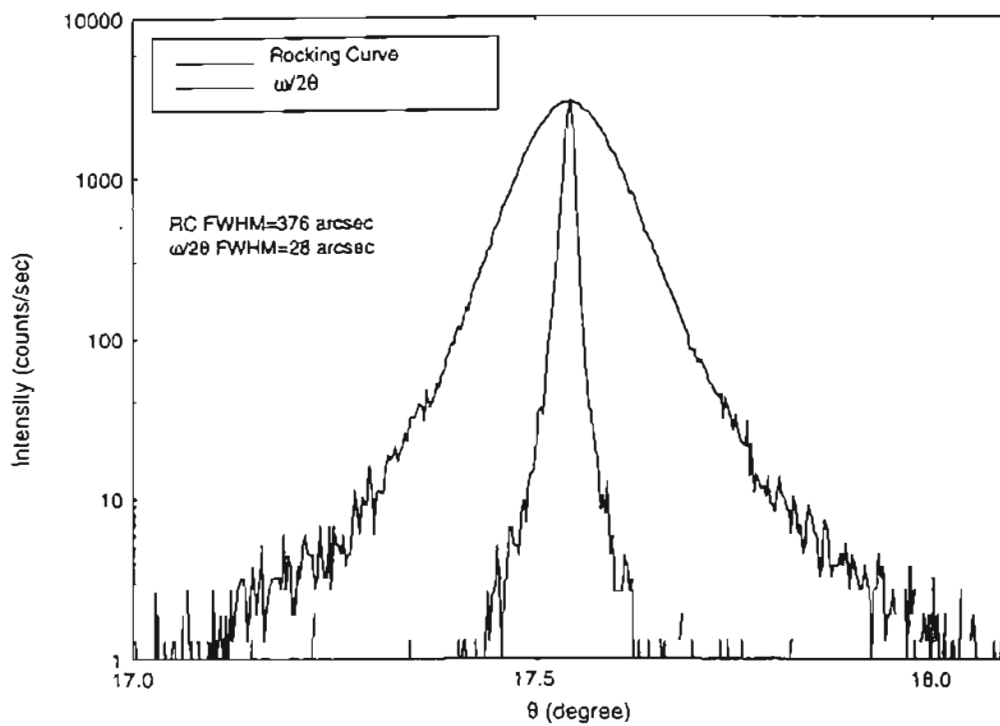


Figure 4.2. *GaN Rocking Curve*: Shown is a typical GaN on sapphire rocking curve of the (002) set of Bragg planes. The broad ω -scan curve suggests in-plane mosaicity. The narrow $\omega/2\theta$ -scan suggests high crystal quality in growth direction.

Let us first consider the base of the epitaxial GaN film: its sapphire substrate. If the substrate itself does not exhibit a very good lattice quality, an epitaxial layer to be grown on top of it will not have a good starting point for the growth. Lattice imperfections apparent on the substrate surface will be incorporated by the layer starting to grow on top because the layer will, given the correct growth conditions, continue the lattice structure of the substrate (in our case rotated by 30 degrees). In order to see the good substrate quality the (006) reciprocal lattice feature of Al_2O_3 has been mapped [Fig. 4.3 (a), p. 77]. The reciprocal map scan reveals the extreme narrowness of the sapphire (006) feature in ω as well as $\omega/2\theta$ -direction. The FWHM of the respective scans is about 10-17 arcsec. This means very good in-plane as well as perpendicular lattice quality and proves the sapphire wafers used to be a sufficient substrate for potentially high quality GaN growth.

In the previous subsection we said that, the general shape of the reciprocal lattice feature is indicated by the ω -scan and the $\omega/2\theta$ -scan. Fig. 4.3 (b) on p. 77 shows the complete reciprocal lattice map of a typical GaN (002) reciprocal lattice feature. A horizontal line intersecting the center of the feature corresponds to the previously described ω -scan while a vertical line intersecting with the center of the feature corresponds to the above $\omega/2\theta$ -scan. The general shape of the GaN (002) feature is an ellipse, confirming the conclusions drawn in the previous subsection concerning the column growth pattern and the statistical intensity variation about the center.

4.2.4 GENERAL FINDINGS

There are a number of general results to be obtained by comparing rocking curves of the different samples of the GaN-on- Al_2O_3 set. The rocking curve is a good indicator of the crystal quality of the epitaxial film grown, and shall be used as such.

In Fig. 4.4 on p. 79 two examples of growth parameter correlation with general crystal quality are shown. Fig. 4.4 (a) displays a graph demonstrating the dependence of the rocking curve FWHM of similar samples on the buffer temperature. It seems that, the higher the buffer temperature, the better the sample quality. There are physical limits, of course. At too low a temperature the sticking coefficient is increased because the

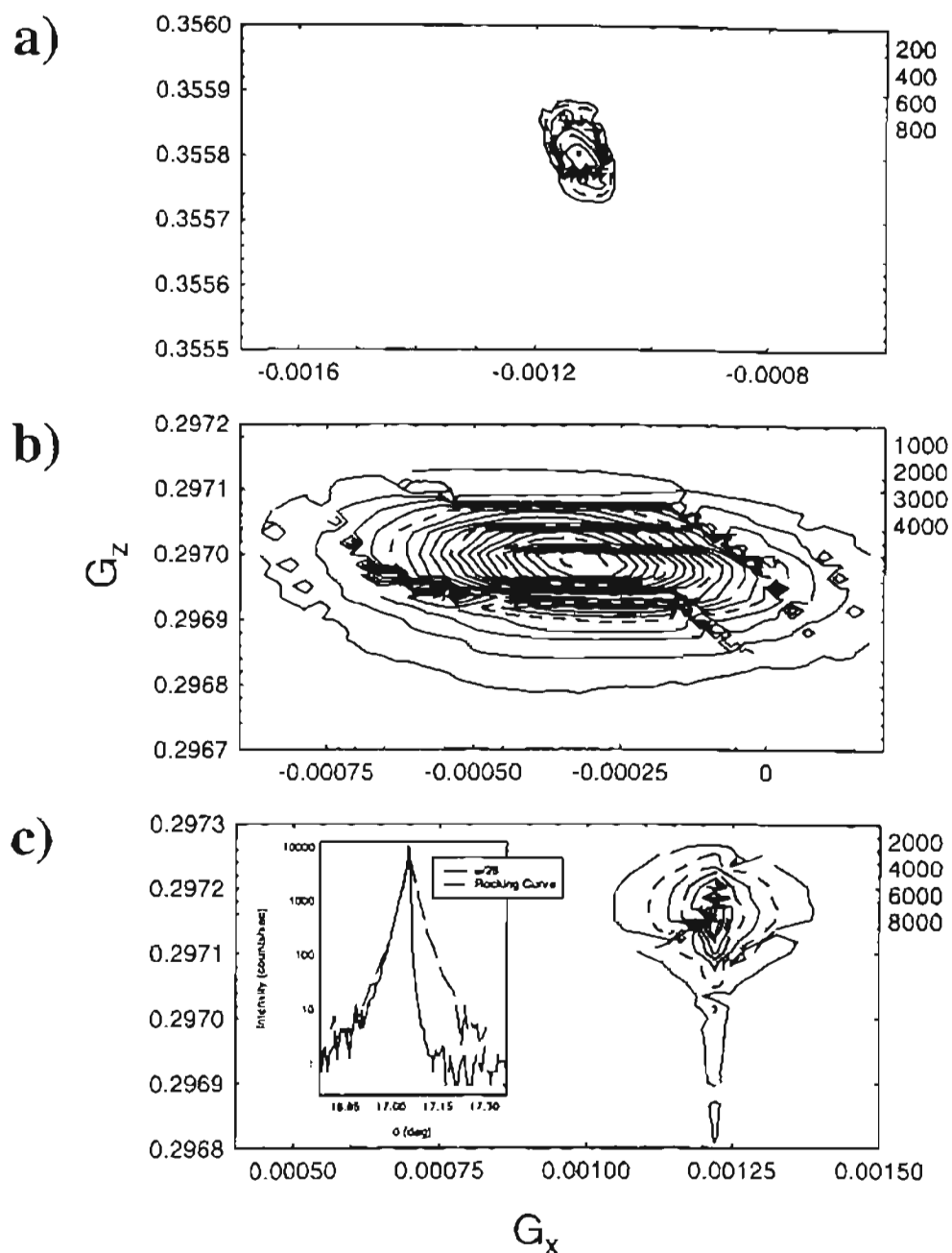


Figure 4.3. *Reciprocal Space Maps of GaN Samples*: The reciprocal space scans show different reciprocal lattice features of the GaN on sapphire sample set: a) Al_2O_3 (006) substrate peak; b) typical GaN (002) layer peak; c) GaN (002) rocking curve and reciprocal space peak of sample OS97.004.

re-evaporation of deposited material ceases. However, limited mobility of the atomic species due to insufficient thermal energy will not allow regular crystal growth. No appreciable single crystal growth will occur. At too high a temperature no deposition would occur because re-evaporation exceeds the sticking coefficient.

Fig. 4.4(c) exhibits a wafermap of a typical GaN on sapphire sample. The wafermap is created from the FWHM of a set of rocking curves. The rocking curves are distributed over a wafer in a matrix of 9×9 scans a distance of 5 mm apart from one another. The wafer disc is fit into the shown square of side length 40 mm. The edges of the square are filled with unrealistically high readings and therefore appear dark. The wafermap explicitly shows the rocking curve FWHM dependence on the flux ratio even on one single wafer. This is possible because the wafer is not rotated within the UHV-chamber of the MBE-system. The circles on the top right and bottom left indicate the positions of the N-plasma source and the Ga effusion cell relative to the waferstage, when one looks at the front side of the wafer. The best region clearly leans toward the N-plasma source. The diagonal wafermap pattern suggests that during a growth-run, the flux ratio is a particularly important parameter for the crystal quality. The influence of, for example, an uneven temperature distribution on the wafer is not to be seen.

By optimizing one growth parameter after another, new optimal growth conditions can be found. Because of the inter-dependence of the growth parameters the process has to be repeated several times.

4.2.5 SPECIFIC FINDINGS

Two samples of the set of GaN films on Al_2O_3 are particularly interesting for two reasons. First, they exhibit the smallest FWHM for the rocking curve of all samples in the set, and second, they show an asymmetry in their respective $\omega/2\theta$ -scan peaks. The small FWHM has been achieved with seemingly different growth conditions for the two samples. The reason for the asymmetry of the $\omega/2\theta$ peak is yet unknown, and only a speculative approach can be taken to answer the question.

Shown in Fig. 4.3(c) on p. 77 is the ω -scan, $\omega/2\theta$ -scan, and the reciprocal space map of the (002) diffraction of the GaN epitaxial thin film of sample OS97.004. This

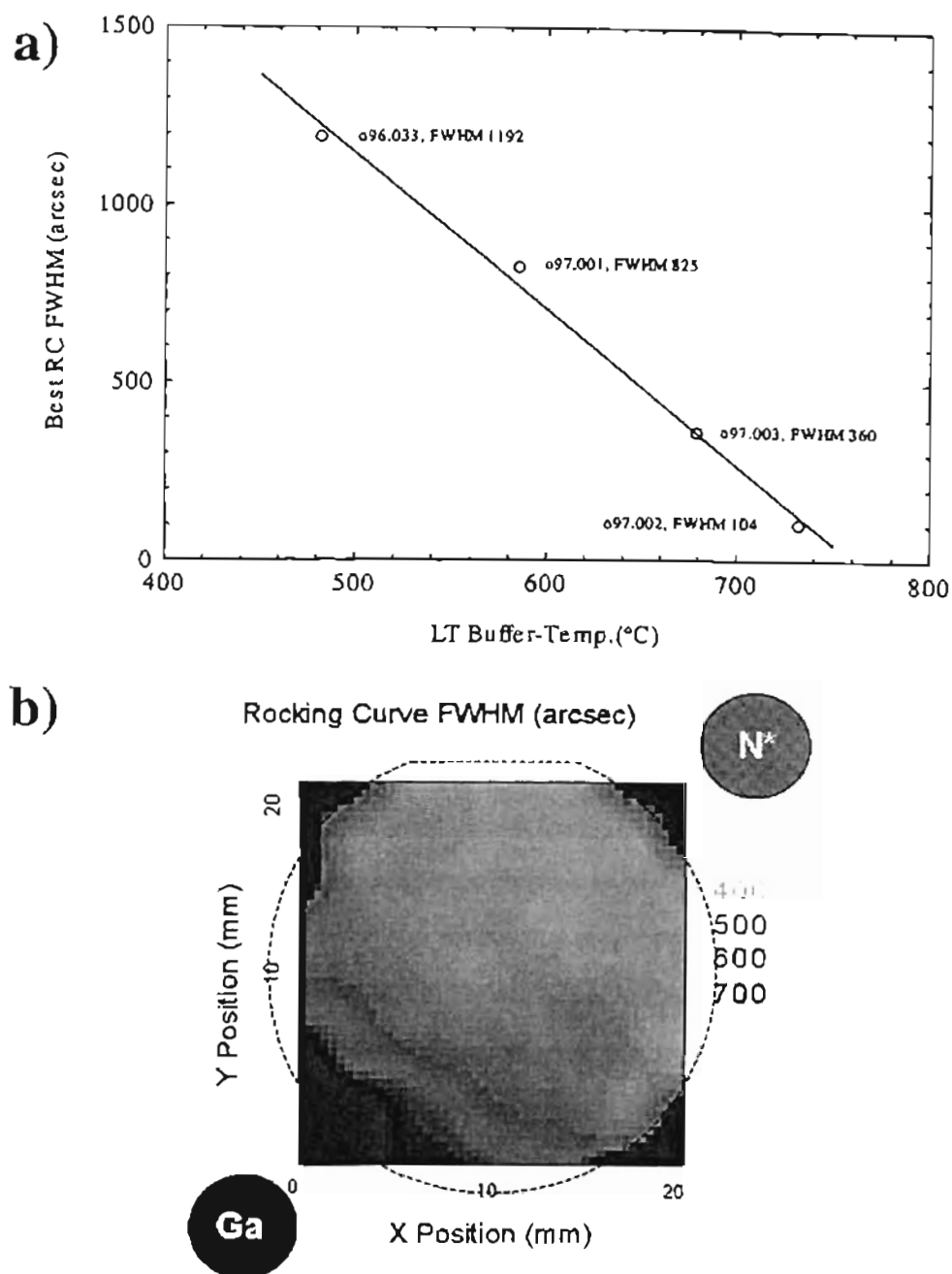


Figure 4.4. *Examples for Rocking Curve Correlation:* Results of different graphs for rocking curve dependencies help improve growth conditions. The GaN epitaxial layer quality depends on a) the GaN buffer temperature, and b) Ga to N* flux ratio shown by a wafermap.

sample originates from a subset of samples grown to for the purpose of studying the effect of the buffer layer growth temperature on crystal quality. For sample OS97.004 the main layer and the buffer layer temperature were identical (730°C). The growth rate of the buffer layer (0.03 $\mu\text{m/hr}$) was smaller than the growth rate of the main layer (0.8 $\mu\text{m/hr}$), due to different source material fluxes applied during the growth run. The buffer layer thickness is 0.03 μm . The total GaN layer thickness as found by optical reflectance is 1.26 μm . The FWHM of the ω -scan curve of sample OS97.004 is recorded with 97 arcsec. The FWHM demonstrated by the $\omega/2\theta$ scan curve is 36 arcsec, according to the Scherrer formula [Eg. (2.71), p. 35] this corresponds to a coherence length of 0.9 μm . This is again on the order of magnitude of the entire sample thickness. The stacking of the atomic planes is extremely good.

In order to find a reason for the extremely good outcome of the HRXRD scans, the next sample was grown under identical conditions, except that the main GaN layer was not deposited. This made it possible to examine an identical GaN buffer layer as the one of sample OS97.004 on a different wafer, sample OS97.005, by means of atomic force microscopy (AFM). The picture shown in Fig. 4.5 on p. 82 was captured by Prof. M. Johnson at the University of Oklahoma, Norman, OK.

The AFM micrograph shows that the buffer layer under the given growth conditions starts to grow in islands on top of the flat sapphire surface. As expected for a hexagonal lattice, the islands take the shape of hexagonal pyramids. The average thickness of the pyramidal "film" is 300 Å. Therefore a number of pyramids are much higher. Because of the outward hexagonal symmetry and the small size of the pyramids, it is safe to assume, that the lattice structure within the pyramids is virtually perfect.

The 16 % lattice mismatch between Al_2O_3 and GaN strains the pyramids. Their perpendicular lattice constant c_{buffer} will be larger than the bulk GaN value. If now a main GaN layer is deposited on top of the pyramids, the gaps between the fully strained pyramids will be closed. Microscopic defects are introduced into the structure. The defects at crystallographic grain borders partially relieve the misfit stress. The lattice constant may assume the bulk value greater than the pyramidal c_{buffer} , resulting in a

lower diffraction angle. Further deposition of material will “grow out” the microscopic defects to some extent and the main layer will be partially strained.

The shape of the $\omega/2\theta$ -scan curve in Fig. 4.3 (c) on p. 77 can be interpreted as a superposition of two peaks: A high angle, sharp main layer peak, and a low angle, somewhat broader peak which is the result of the defect area at the interface of the buffer layer and the main layer. The ω -scan has an almost triangular shape. Again, this may be interpreted as one very sharp peak in the center, due to the nearly parallel stacking of planes within the main layer, and a broader peak, centered around the same angle, indicating the loss of coherency of the plane normal direction in the “grainy” interface area. A similar explanation, has been given by Zhu et al.⁵²

Another sample showing good HRXRD results is sample OS98.002. This sample also exhibits the asymmetry in its $\omega/2\theta$ scan curve. Sample OS98.002 is part of a subset aimed at investigating the influence of the main layer growth temperature on the crystal quality. No buffer layer has been deposited. After growth, the sample has been thermally annealed at a temperature of 900 °C for 10 minutes. The annealing treatment has not been applied to the other samples of the set. It was a preliminary attempt to study the influence of after-growth thermal annealing on the crystal structure. While the other samples of the set showed average crystal quality, the result for the annealed sample is promising and further studies will have to be done.

The thickness of sample OS98.002 has been estimated to be 1.4 μm . An optical measurement was not possible because the annealing process roughened the sample surface. The FWHM of the ω -scan curve of sample OS98.002 is 63 arcsec (scan not shown). The FWHM of the $\omega/2\theta$ -scan is 23 arcsec. The scan curve shapes match the ones seen for sample OS97.004 in every detail [see inset of Fig. 4.3 (c) on p. 77]. The FWHM of the ω -scan yields the impressive coherence length of 1.4 μm , which coincides with the sample thickness. There are virtually no flaws in the vertical plane stacking.

For the scan curve shapes of sample OS98.002 exactly the same double peak description may be given as before for sample OS97.004. Only this time the possible explanation for the two different c lattice parameters is different since there is no buffer layer. The thermal annealing process reorganized the GaN lattice. At the Al_2O_3 -GaN

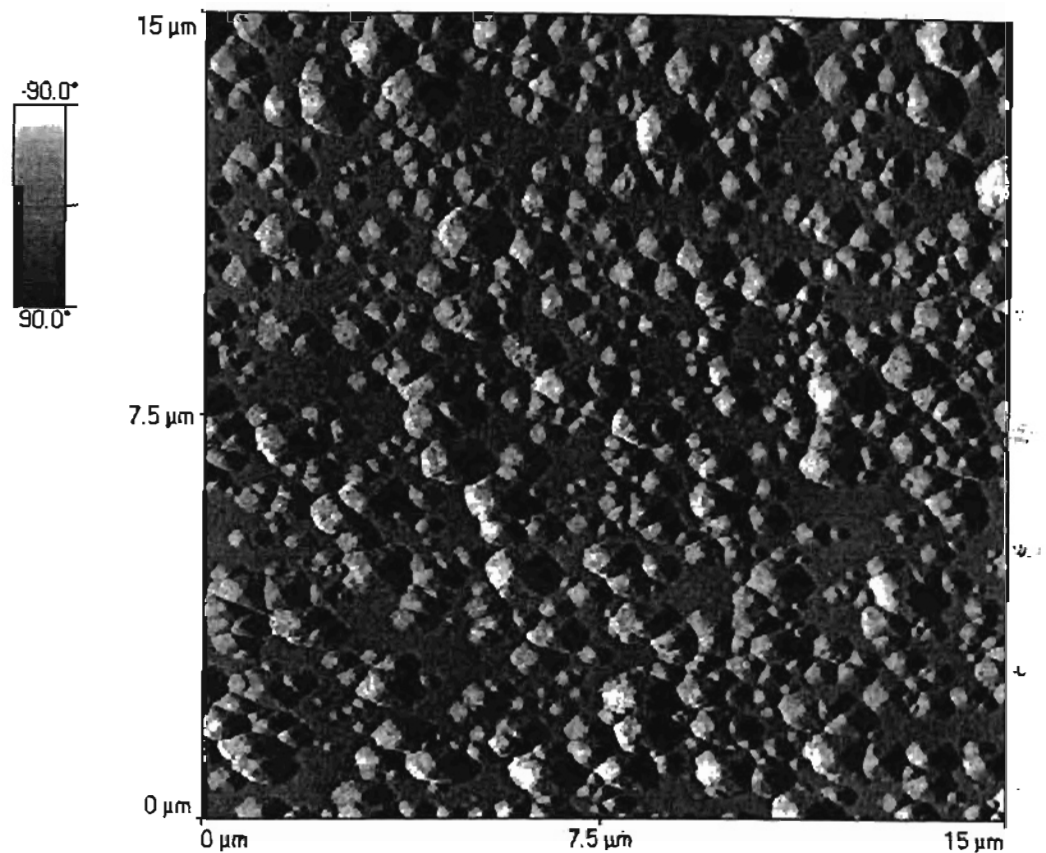


Figure 4.5. *AFM Picture of GaN Buffer Layer of Sample OS97.005:* The picture shows GaN hexagonal pyramids on a flat AlN layer attained by nitriding the surface of the sapphire wafer, with a magnification of about 7500. The gray scale indicates the angular orientation of the pyramidal surfaces relative to the vertical. The average GaN “layer” thickness is 300\AA .

interface the high temperature flash minimized the lattice mismatch between the Al_2O_3 and GaN lattices, and microscopic defects due to strain were eliminated. At the same time re-evaporation of growth materials took place at the sample surface, leaving defects behind. A porous microstructure may establish itself near the surface, because of preferential surface evaporation.⁵³ After cool down the effect leaves a highly homogeneous lattice deep in the layer. Further up defects due to strain appear, worsening the lattice defects introduced by the re-evaporation. A 'grainy' or 'porous' structure near the surface of the sample is the result. This structure will cause the same X-ray diffraction pattern as before.

4.3 MBE-GROWN GaN ON ZnO

There are alternative substrates to sapphire for the growth of wurtzite structured GaN, namely SiC and ZnO. Both have hexagonal lattice structures and lattice mismatches smaller than the one of sapphire when compared to GaN. The ZnO/GaN mismatch is only 1.9%, which makes ZnO a much better fit than sapphire. A small number of GaN on ZnO samples have been grown by RF-MBE at Oklahoma State University as described above. The general sample layout is the same as the one for the already discussed GaN on sapphire samples. A slowly grown $0.03\ \mu\text{m}$ GaN buffer has been deposited first, followed by the $1\text{-}2\ \mu\text{m}$ GaN main layer.

4.3.1 GENERAL FINDINGS

Seven growth runs have been performed to find out if GaN can be grown on ZnO with competitive quality.* The growth conditions have been derived from previous GaN on sapphire growth runs. GaN has been deposited on the Zn face of the ZnO substrate.

In order to find out which site of the substrate (Zn-face or O-face) would be grown on, a pre-growth piezo tester has been devised. When squeezing the ZnO substrate material in (001) direction, an electrical pulse can be measured using a high impedance amplifier. The orientation of the pulse (positive/negative) indicates which face is 'up'

*The number of growth runs was limited to seven because of limited substrate availability.

relative to the squeezing electrodes. This piezo-test is possible because of the ionic nature of the ZnO molecule. Zn is anionic while O is cationic. The double-layer stacking of Zn and O planes within the Wurtzite structure in (001) direction makes it possible to use the piezo effect for a polarization measurement.

It has been chosen to grow on the positive Zn-face because it makes the bonding of a first N layer easier during initial nitridation than a very electronegative O would. Variations in buffer temperature and main layer temperature have been applied during the growth process in order to improve the crystal quality. It should be noted that the ZnO substrate crystal quality is not as good as the sapphire substrate crystal quality. Where the sapphire substrate exhibits a rocking curve FWHM of 10-17 arcsec, ZnO shows 240 arcsec. In all growth runs so far, the epitaxial film quality did not surpass the substrate crystal quality.

The rocking curves of epitaxial GaN layers on ZnO show FWHM between 1300 and 3525 arcsec. The ω -scan of the highest quality GaN film, sample OS97.028, is shown in Fig. 4.6 (a) on p. 86. Due to the small lattice mismatch in in-plane (1.9 %) as well as in growth direction (0.5 %), a minimally strained GaN layer is to be seen. The sharp ZnO peak and the broad GaN peak are very close, as expected. A lattice parameter measurement finds $c_{\text{ZnO}} = 5.205(18) \text{ \AA}$ and $c_{\text{GaN}} = 5.201(6) \text{ \AA}$, which, considering the error, is a negligible difference (0.08 %diff).

The best result for an $\omega/2\theta$ -scan yields a FWHM of 251 arcsec. The vertical coherence length then is $0.125 \mu\text{m}$, which is comparatively small. The GaN film thickness of sample OS97.028 is $1.7 \mu\text{m}$.

The given numbers prove that further research is necessary in order to accomplish the goal of competitive GaN epitaxial film quality on ZnO. At this time sapphire appears to be the better substrate choice, not only because of not yet ideal growth conditions for GaN on ZnO, but also because to date the crystal quality of sapphire substrates is much better than the crystal quality of any ZnO substrate.

4.3.2 SPECIFIC FINDINGS

All GaN on ZnO samples exhibit a tilt. The angle between the zero setting of the Philips MRD waferstage and the ZnO and GaN symmetrical sets of planes has a value of 1–2 degrees. This is more than can be attributed to a present mounting error, as can be seen by comparison with similar GaN on sapphire samples.

The tilt of a set of planes relative to the sample mounting is found by a set of rocking curves with different ϕ angles. Fig. 4.6 (a) on p. 86 shows two ω -scans 180 degrees in ϕ apart, which show the two extreme Bragg angles. The two ω -scans at $\phi = \pm 90$ degrees coincide in the ZnO Bragg angle. The shown angular difference between the Bragg angles for $\phi=0$ degree and $\phi=180$ degree is twice the tilt angle (3.354 degrees) of the ZnO (002) planes with respect to the sample mounting. The same scans can be taken again, only this time centered on the GaN peak. A different tilt angle results (3.738 degree). The difference between the two tilt angles eliminates the mounting error and yields the tilt $\delta=0.192$ degree, for sample OS97.028, between the substrate and the epitaxial layer.

The same conclusions can be drawn from the reciprocal space map of the (002) reciprocal lattice feature shown in Fig. 4.6 (b). The relative angles between sample orientation on the waferstage, substrate, and epitaxial layer are the same angles as the ones between the respective reciprocal lattice vectors. The reciprocal space map shows no lineup of substrate and layer peak in $\omega/2\theta$ direction (otherwise δ would be zero), hinting towards a relaxed layer growth. This conclusion has to be drawn carefully since both peaks are slightly off axis (see Nagai model below). What can be seen without a doubt is the great broadness of both, the ZnO substrate as well as the GaN layer peak.

Given the fact that the ZnO-(002)-plane-to-mounting-tilt can not be accounted for solely by a mounting error, there has to be a tilt angle between the sample surface and the set of (001)-ZnO-planes of the sample. In order to find out about the interface structure between ZnO substrate and GaN layer let us consider Nagai's construction for a tilted substrate as seen in Fig. 4.7 on p. 88.^{54,55} If we had a perfect crystal, cut slightly off axis,

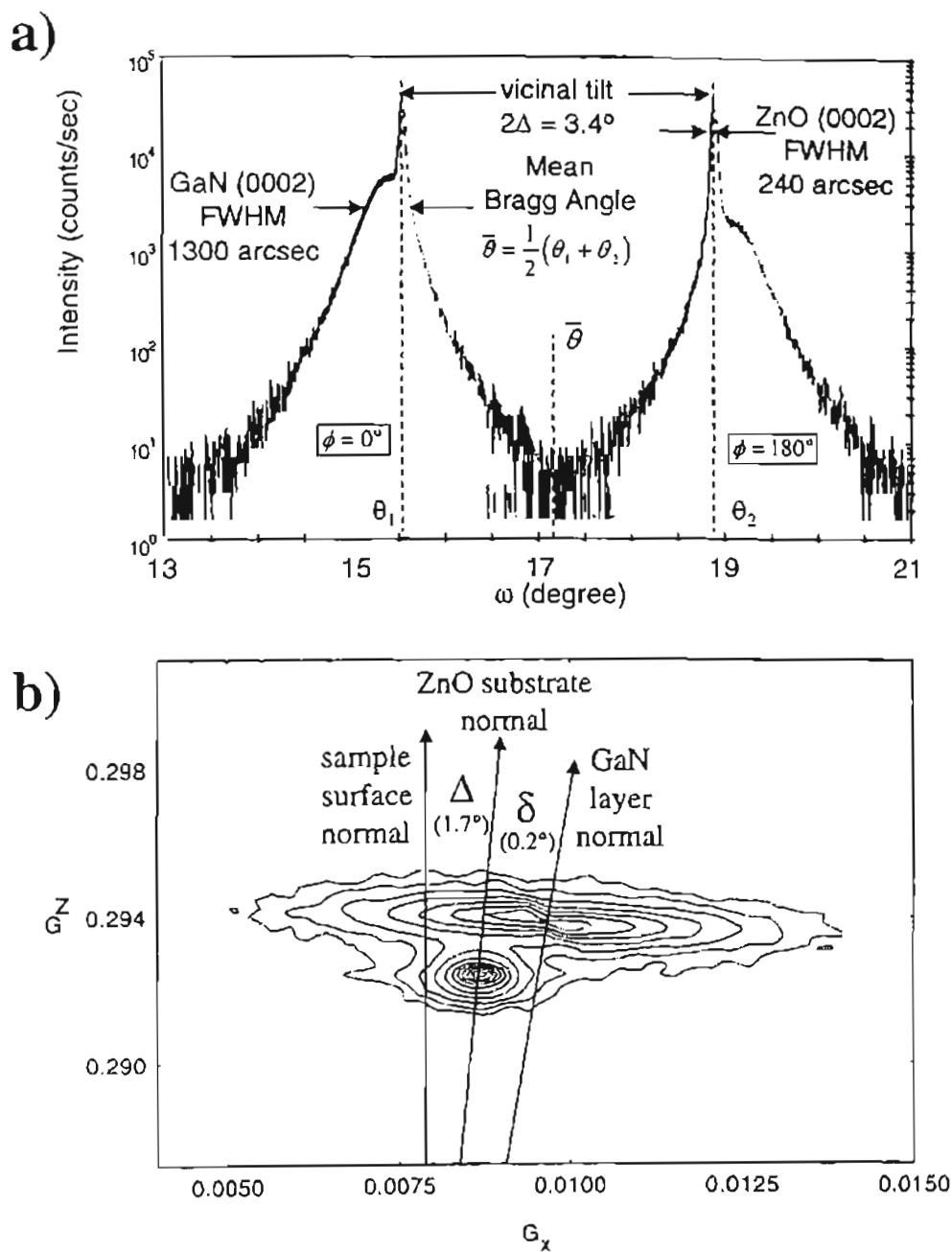


Figure 4.6. *GaN on ZnO Tilt Measurement*: Shown are scans from sample OS97.028, a) two rocking curves for extremum waferstage angles ϕ , b) reciprocal space map of the (002) feature at $\phi=180$ degree.

and then grew an epitaxial thin film with slightly bigger unit cell fully strained on top of the cut, we would have the depicted situation.

Shown are the angle Δ between sample surface and substrate, and the angle δ between substrate and epitaxial layer. The common in-plane lattice parameter is $a_{\text{substrate}}$, the perpendicular lattice parameters are $c_{\text{substrate}}$ and c_{layer} , respectively. The equation

$$\frac{\Delta c}{n a_{\text{substrate}}} = \frac{\Delta c}{c_{\text{substrate}}} \cdot \frac{c_{\text{substrate}}}{n a_{\text{substrate}}}, \quad (4.1)$$

where $\Delta c = c_{\text{layer}} - c_{\text{substrate}}$ denotes the perpendicular lattice parameter difference, is certainly valid. The integer n is the number of unit cells in one "tooth" of the miscleaved substrate surface [Fig. 4.7]. Inspecting the bold set of lines within Fig. 4.7 reveals the equivalent expression

$$\tan \delta = \frac{\Delta c}{c_{\text{substrate}}} \tan \Delta. \quad (4.2)$$

This means that if the lattice structure is ideal and the tilt is only due to a miscut of the substrate crystal, the angle Δ between sample surface and, in our case, the ZnO (002) planes can be predicted. The appropriate calculation using Eq. (2.53) on p. 29 with $\epsilon_t = 1.53$ for GaN yields $\Delta = 5.63$ degree. This clearly can not be the case for the sample under consideration since the measured tilt, mounting error included, is only 1.7 degree.

The conclusion has to be that the Nagai model is not valid for the interface between the ZnO substrate and its GaN layer studied here. This is not surprising since the FWHM of rocking curves cited earlier, indicated relatively poor substrate quality. The angle between the GaN and the ZnO crystal lattice orientation is 0.2 degree. There is a tilt between the ZnO lattice orientation and sample surface, and there is a tilt between the GaN lattice orientation and the sample surface. The ideal Nagai model does not allow us to correlate the two, which means there is a high density of crystal imperfections in the interface area, partly accounting for the very broad scan results obtained.

4.4 MOCVD-GROWN InGaN ON Al_2O_3

So far MBE-grown samples have been discussed. Another common growth technique is metal-organic chemical vapor deposition (MOCVD). A number of InGaN on

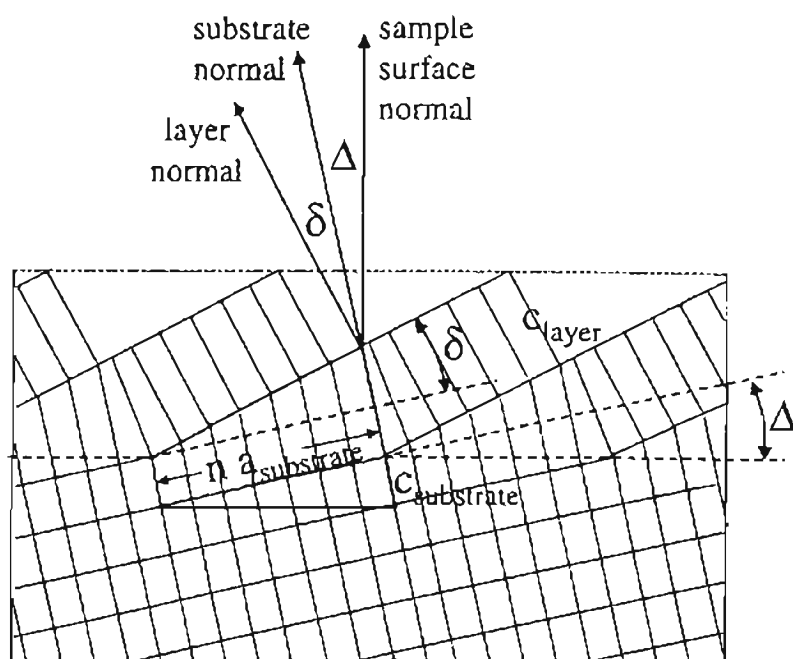


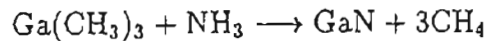
Figure 4.7. *Single Layer Tilt*: Model suggested by Nagai for tilted layers on misoriented substrates.^{54,55} Every box represents one unit cell. The angle Δ is the substrate miscut, and δ is the angle between substrate and epitaxial layer.

sapphire epitaxial thin films have been investigated. The intermediate GaN buffer layer was of roughly the same quality as a typical MBE-grown GaN on sapphire sample, as described earlier. The $\omega/2\theta$ -scans performed applied the slit-optics of the MRD system.

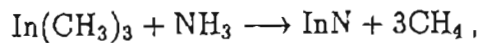
4.4.1 MOCVD-GROWTH PROCESS

A simplified description of the MOCVD-growth process appears similar to the MBE-growth technique. Within a growth chamber a substrate wafer is heated to provide the necessary chemical reaction temperature. Source gases, such as trimethylgallium [$\text{Ga}(\text{CH}_3)_3$] to provide Ga, trimethylindium [$\text{In}(\text{CH}_3)_3$] to provide In, and ammonia [NH_3] to provide N are flowed over the substrate wafer.

On the wafer surface heat activated chemical reactions set free the elements, which are then incorporated into the epitaxial thin film to be grown. For the growth of GaN and InN, which is what we are interested in, the chemical reactions are



and



where GaN and InN are deposited on the wafer, and methane is a chemically inert gaseous by-product. Compared to a typical MBE system, the gasflows, and therefore the corresponding element fluxes, are orders of magnitude higher in a typical MOCVD system. This yields much higher growth rates. At the same time, however, the ability to control the growth atomic layer by atomic layer is lost. As was the case for the MBE-growth, the critical growth parameters are the gas flowrates and the wafer temperature (growth temperature).

4.4.2 GENERAL FINDINGS

A set of InGaN epitaxial thin films grown by MOCVD has been investigated. The general sample structure is shown in Fig. 4.1 (b) on p. 69. A $1\ \mu\text{m}$ thick GaN buffer layer has been grown on a sapphire substrate. Then the $0.1\ \mu\text{m}$ InGaN film with varying In composition has been deposited.

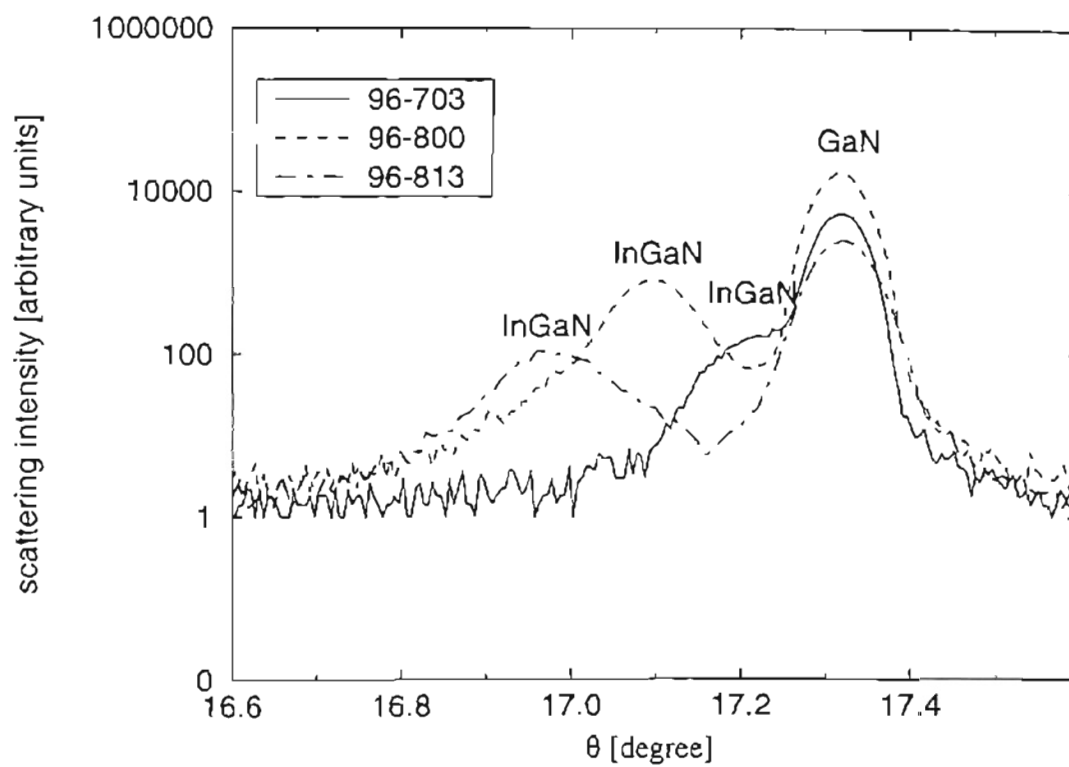


Figure 4.8. *MOCDV-Grown Single InGaN Thin Films*: Shown are $\omega/2\theta$ -scans of three InGaN thin films on a GaN buffer layer on sapphire. These films illustrate Vegard's law for relaxed layers.

Fig. 4.8 shows three $\omega/2\theta$ scans of three InGaN thin film samples. The three samples confirm Vegard's law for a relaxed layer on a substrate. We see a InGaN layer on a GaN "virtual substrate". The angular distance between the InGaN alloy peak and the GaN "substrate" peak only depends on the In content in the InGaN layer. The angular distances, 466 arcsec, 797 arcsec, and 1233 arcsec, yield 6.3 %, 11.0 %, and 17.3 % In content for samples 96-701, 96-800, and 96-813 respectively, according to Eq. (2.65) on p. 34. The planar spacings d in the equation have been calculated from the peak angles using Bragg's equation [Eq. (2.1) on p. 7].

The resulting In contents are close to the target compositions of the grower, which were 13 %, 14 %, and 24 %, respectively. A strained simulation does not yield a similar agreement. It is safe to assume that the InGaN layers are relaxed since a strained simulation results in In compositions about 50 % less than what Vegard's law predicts. Phase segregation has not been observed. No separate InN peak has been found.

4.5 MOCVD-GROWN GaN/InGaN SUPERLATTICES

This section will present results on MOCVD-grown InGaN/GaN/AlGaN multiple quantum wells (MQW), which also will be reported elsewhere.⁵⁷ The sample layout is shown in Fig. 4.1 (c) on p. 69. A 12-period 45 Å GaN barrier plus 30 Å InGaN well structure has been deposited on a 1.8 μm GaN buffer layer. The superlattice structure is sealed with a 0.1 μm Al_{0.07}Ga_{0.93}N capping layer. The growth was initiated on a c-plane sapphire substrate. Gas sources used were trimethylgallium [Ga(CH₃)₃], trimethylindium [In(CH₃)₃], trimethylaluminum [Al(CH₃)₃] and ammonia (NH₃). Disilane [Si₂H₆] provided the *n*-type dopant. The growth temperatures of the GaN buffer, the superlattice, and the AlGaN capping layer were 1050 °C, 790 °C, and 1040 °C, respectively. The fluxes applied during the superlattice growth were 5 μmol/min for Ga(CH₃)₃ and 14 μmol/min for In(CH₃)₃. The ammonia flow was held at a steady 0.35 mol/min. The samples under study differ only in the amount of Si-doping, ranging from 1 × 10¹⁷ to 1 × 10¹⁹ cm⁻³ in the GaN barriers of the MQW. This was achieved by varying the disilane doping precursor flux from 0 to 4 nmol/min during the GaN barrier growth. The doping concentrations have been confirmed by Hall measurements and

secondary ion mass spectroscopy (SIMS). These experiments and others, such as optical property experiments, are reported elsewhere.⁵⁸⁻⁶⁰

4.5.1 Si-DOPING

Figure 4.9 on p. 93 shows three (002)- $\omega/2\theta$ -scans of MQW samples with different Si doping levels n within the GaN barrier layer of the superlattice. The slit optics has been used to investigate the influence of Si doping of $n < 1 \times 10^{17}$ to $n = 3 \times 10^{19} \text{ cm}^{-3}$ on the diffraction pattern.

All layers produce reflected intensity peaks. The strongest peak is due to the GaN buffer layer, and its high-angle shoulder is due to the AlGaIn capping layer. Four superlattice peaks can be seen. The “virtual substrate” of the superlattice, the GaN buffer layer, is of good quality. All samples offer rocking curves with a FWHM < 100 arcsec and an $\omega/2\theta$ scan FWHM < 30 arcsec for the GaN buffer layer. For all samples the figure shows a number of superlattice satellite peaks, indicative of good superlattice quality. The nominally undoped sample ($n < 1 \times 10^{17} \text{ cm}^{-3}$) exhibits superlattice peaks with an asymmetric lineshape, as opposed to the two doped samples, which show a symmetric broadening in their respective superlattice peaks, indicating that the doped samples more closely resemble the ideal model of the structure. The simulation of the diffracted intensity does not show asymmetric peaks. The “mirror-image” resemblance between the ± 1 superlattice peaks shows that the broadening is, at least partially, due to superlattice period fluctuations. The fluctuations may be caused by interface roughness and/or intermixing at the GaN/InGaIn interfaces.

The angular distance between the superlattice peaks has been used to find the superlattice period. Small variations in the superlattice period occur (80 Å to 86 Å), but no correlation with the Si doping is to be seen. A clear dependence on the Si doping level is to be found in the higher-order satellite peak FWHM. The inset of Fig. 4.9 shows the variation of FWHM of higher-order superlattice peaks as a function of Si doping. With increasing Si doping-level the FWHM of the higher-order peaks become smaller. This suggests an improved interface quality within the superlattice with increased Si doping within the GaN barrier layer. The ratio of integrated intensities of the various

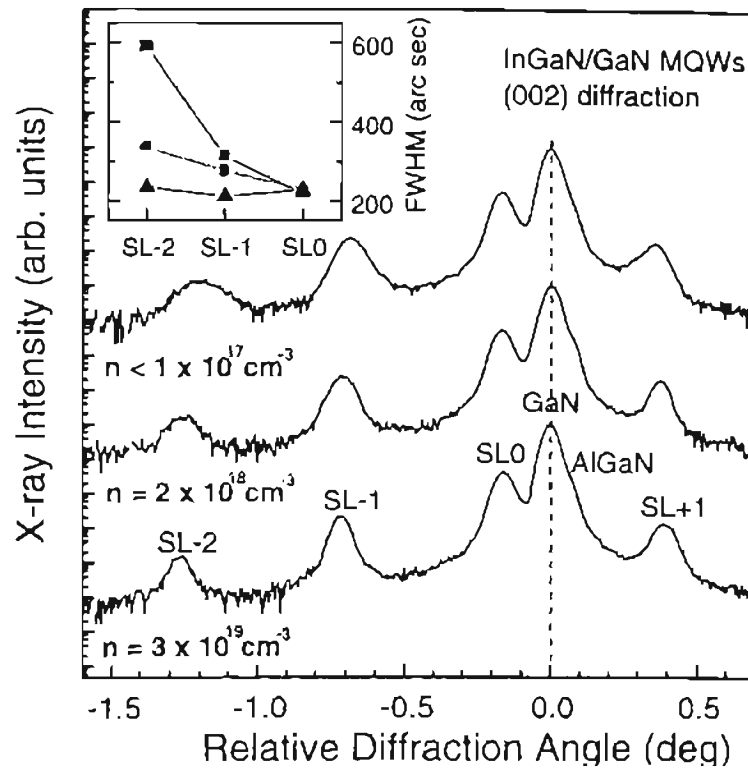


Figure 4.9. *MOCVD Superlattice Dependence on Si Doping*: Shown are the (002) reflection HRXRD curves of 12-period InGaN/GaN/AlGaN MQW samples with different Si doping levels n in the GaN barrier layers. The variation of the FWHM of the higher-order superlattice peaks is shown in the inset as a function of Si-doping level.

peaks of every one sample are almost identical, when compared to the respective ratio of another sample. This is expected because the samples should differ only in their structural perfection.

Si doping clearly affects the structural quality of the GaN/InGaN superlattice. It has been speculated that the quality of the GaN barrier and its surface free energy are changed.⁶¹ This then would affect the growth condition, or growth mode, of the InGaN well deposited on the Si doped GaN barrier.^{62,63} Further investigations are needed to confirm these claims.

4.5.2 KINEMATICAL SIMULATION

A more detailed approach reveals a better picture of the broadening and lineshape of the MQW sample superlattice. The triple-axis optics setup has been used to increase instrumental resolution. Comparison with the kinematical simulation of the scanned MQW structure shows very good agreement.

For the heavily doped sample ($n = 3 \times 10^{19} \text{ cm}^{-3}$), Fig. 4.10 on p.95 shows a receiving slit scan (curve a), a triple axis scan (curve b), and the computed simulation (curve c). When changing the HRXRD instrument optics from slit-optics to the triple axis setup, the detailed Pendellösung fringes characteristic of a high crystalline quality of the layers are revealed. The Pendellösung fringes are due to interference of coherent X-ray waves, reflected from the layer upper/lower planar boundaries.⁶⁴ Interface imperfections or compositional inhomogeneity would decrease phase coherency, and Pendellösung fringes would not arise. The presence of Pendellösung fringes and the narrow FWHM of the superlattice peaks suggest very good interface quality.

Figure 4.10 shows an excellent agreement between the triple axis optics scan and the simulated data. The simulation assumes a fully strained InGaN/GaN superlattice on a GaN substrate with (curve c) and without (curve d) an AlGaN capping layer, according to the general sample layout. The Si doping is not accounted for in the simulation. The excellent agreement hints to a near perfect crystal structure of the sample.

The triple axis scan shows a modulation of the Pendellösung fringes. This is due to interference of coherent X-ray waves caused by reflections of the AlGaN capping

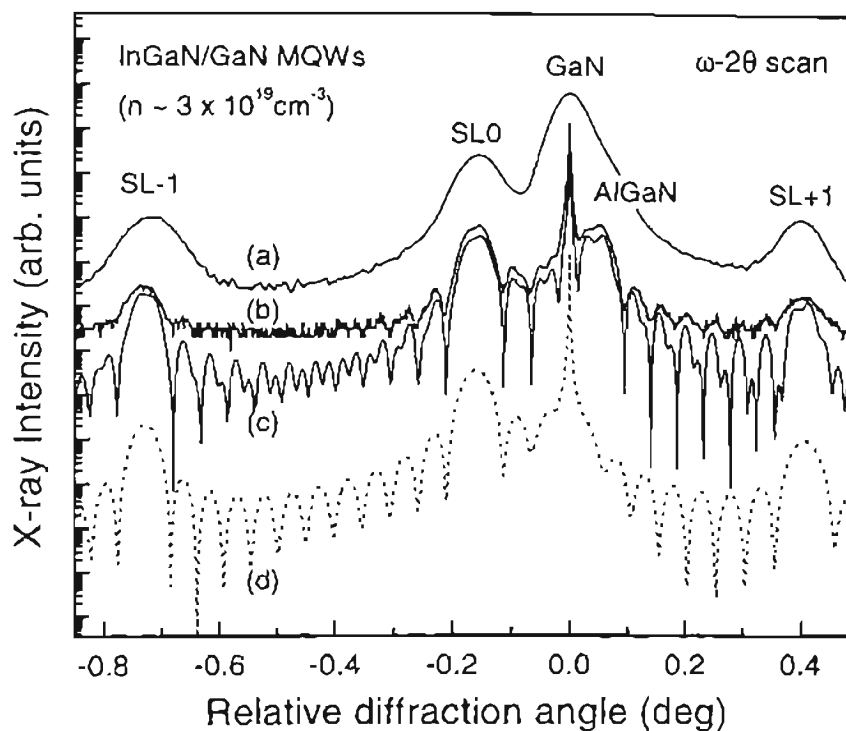


Figure 4.10. *MOCVD Superlattice $\omega/2\theta$ -Scan and Kinematical Simulation*: Shown are $\omega/2\theta$ diffraction curves obtained by a) slit-optics XRD, b) triple axis optics HRXRD, c) kinematical simulation. Curve d) shows a kinematical simulation without AlGaN capping layer. The curves are displaced vertically for clarity.

layer, as can be seen by comparing the two simulated curves. In effect, the fringes are due to both, the superlattice and the capping layer.

A comparison of a triple axis optics scan of the undoped sample with the simulation shows that, although Pendellösung fringes are still observed between the zeroth order superlattice peak and the GaN buffer layer peak, further outward the fringes cease to be resolvable, and the higher-order superlattice peak shapes differ significantly from the ideal crystal simulation.

The conclusion is that Si doping in the GaN barrier layer of the superlattice influences the interface quality of the superlattice. The highest Si doping level ($n = 3 \times 10^{19} \text{ cm}^{-3}$) enhances the overall crystal quality the most.

4.5.3 RECIPROCAL SPACE MAPS

With the help of reciprocal space maps we can identify the contributions to X-ray diffraction peak broadening due to strain, mosaicity, and microdefects separately, and draw refined conclusions about the crystal quality of the MQW structures under study.

Figure 4.11 on p. 97 shows the reciprocal lattice features defined by the Miller indices (002), (004), and (114). The diffraction pattern of plane set (114) has been found to yield the highest intensity of all experimentally accessible asymmetrical reciprocal lattice features. All reciprocal lattice maps show the high intensity GaN “virtual substrate” peak, the AlGaIn capping layer peak, and the zeroth order InGaIn/GaN superlattice peak. Additionally, the very strong (002) reflection reveals two Pendellösung fringes above the AlGaIn peak, as well as in between the GaN peak and the zeroth order superlattice peak. The (002) reflection also allows for the -1 superlattice peak to be resolved.

The main broadening direction of the GaN peak is the lateral \vec{G}_x direction, suggesting a finite in-plane coherence length or grain size for the “virtual substrate” layer. Inspection of the symmetrical reciprocal lattice features seems to indicate the same for the overlying epitaxial structure. Only the asymmetrical scan reveals the mosaic nature of the superlattice peak broadening in ω -scan direction, as indicated by the lines in the (114) reciprocal space map of Fig. 4.11. Additionally, it is clear by considering

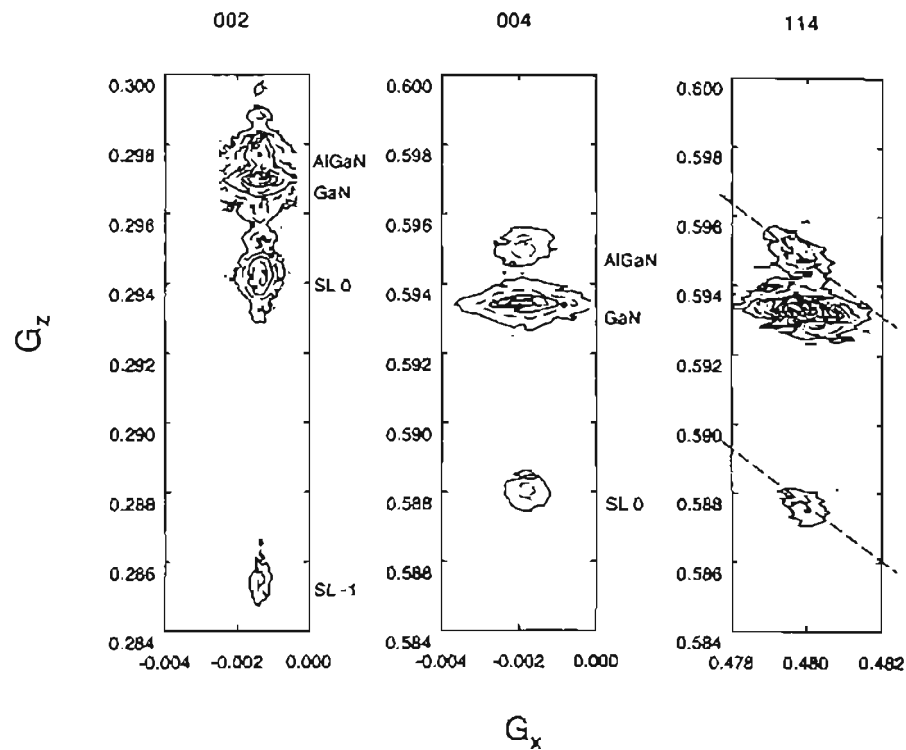


Figure 4.11. *MOCVD Superlattice Reciprocal Space Map*: Shown are reciprocal space maps of the (002), (004), and (114) reflections for the InGaIn/GaN/AlGaIn MQW sample with the highest Si-doping level ($n = 3 \times 10^{19}$). The isointensity contours (solid lines) correspond to 1, 10, 100, and 1000 counts/sec, respectively.

the asymmetrical reciprocal lattice feature that, the superlattice as well as the capping layer, are coherently strained with respect to the GaN buffer layer. All peaks, the GaN buffer layer, the InGaN superlattice peak, and the AlGaIn capping layer peak, line up in \vec{G}_z direction, hence all layers have to have the same in-plane lattice constant a . All samples under study show the same reciprocal lattice map features. Different levels of silicon doping have no effect on the strain state of the epitaxial structure of a sample. All samples exhibit coherently strained superlattice and capping layer.

The given evidence supports the thesis that Si-doping enhances the interfacial quality of the superlattice while at the same time no relaxation of the lattice-mismatch strain can be observed.

4.6 MBE-GROWN GaN/InGaN SUPERLATTICES

The growth kinetics concerning MBE-grown superlattices are little understood. This, and the successful growth of InGaIn/GaN superlattices by MOCVD, motivates a similar attempt utilizing MBE.

The set of MBE-grown superlattice samples comprises samples consisting of a 2.4 μm GaN buffer layer on sapphire on top of which a 20 period, 0.4 μm thick InGaIn/GaN superlattice has been grown. This structure has been chosen because simulations (Append. A) have shown a very strong superlattice diffraction pattern for this particular superlattice. The chosen structure would make it easy to assess whether a superlattice has been grown at all in the crucial first attempts of doing so.

The physical properties of the superlattice will be discussed below. There is no capping layer. Let us consider two examples of the grown set, sample OS98.020 and sample OS98.022.* Despite the fact that the buffer layers of both samples have been grown at different temperatures, 750 °C and 780 °C, respectively, all X-ray data indicates nearly identical buffer layer properties, so that we can concentrate on the superlattice growth. The only varied parameter for the superlattice growth is the N-plasma flux. The atomic flux depends on plasma power and gas flow. At a plasma power of 400 Watts the

*A vastly more complete discussion of the set of MBE-grown InGaIn/GaN superlattice samples will be presented in M. L. O'Steen's PhD. thesis.⁵¹

N partial pressure in the MBE chamber was 3×10^{-5} Torr for sample OS98.020, and at 320 Watts plasma power it was 4×10^{-5} Torr for sample OS98.022.

4.6.1 GENERAL FINDINGS

Four scans in particular shall be considered to give a qualitative description of the two samples. These are the standardized $\omega/2\theta$ -scans of the (002) set of planes for both samples, OS98.020 and OS98.022, and reciprocal space maps of reciprocal lattice features (002) and (114) for sample OS98.022. Fig. 4.12 on p. 100 shows the mentioned scans.

Both $\omega/2\theta$ -scans show the high intensity buffer layer peak, and up to five superlattice peaks on the low angle side of the zeroth order superlattice peak. The first superlattice peak on the high angle side, SL1, can be seen as a slight shoulder on the right of the GaN buffer layer peak. Clearly visible again is the second peak on the right side, SL2. Higher order peaks are of extremely low intensity and are therefore not detected. On the high angle side the kinematical simulation shows that the sample geometry does not allow for peaks SL3 and SL4 — these superlattice peaks are effectively diminished by destructive interference.

The integrated superlattice peak intensities decrease with increasing peak index. This is evidence for interdiffusion — more so in sample OS98.020 than in OS98.022. The peakshapes reveal an increasing FWHM with increasing superlattice peak index. This has been seen before in the undoped MOCVD-grown superlattice sample. Fluctuations in the superlattice period is the main reason for this behavior. Because of the low-resolution-scan grading cannot be ruled out (see Sect. 2.6.3). A vertical temperature gradient along the growth direction, as is likely to occur in the MBE system used, may have activated interdiffusion differently throughout the superlattice, and therefore may have caused different well to barrier ratios within the subsequent periods of the superlattice. This point could not be clarified since the overall crystal quality does not allow detailed high resolution scans.

Figure 4.12 also shows symmetrical and asymmetrical reciprocal space maps of sample OS98.022. The qualitative results of these maps may be applied to both, sample

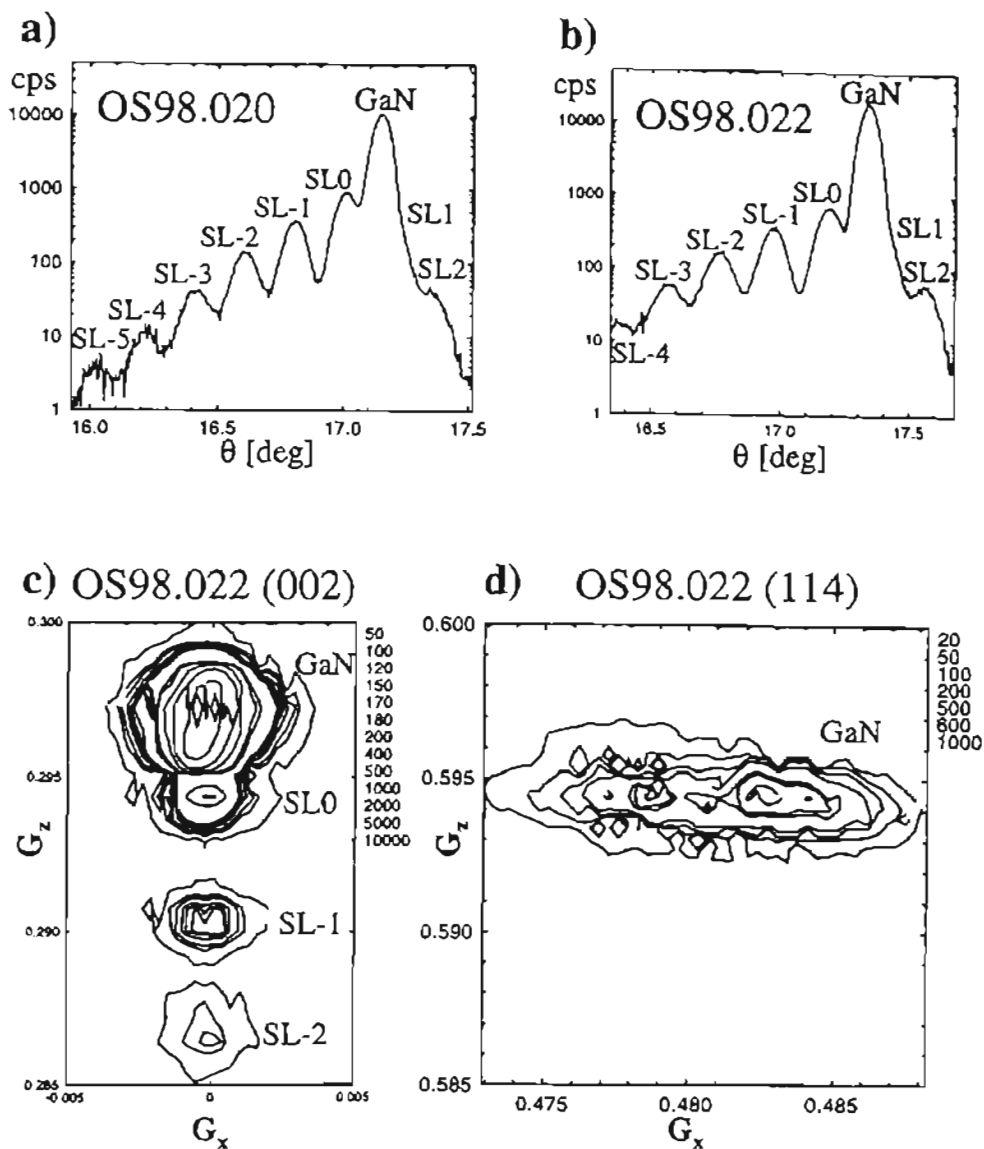


Figure 4.12. *MBE Grown Superlattices*: Scans taken from MBE-grown superlattice samples, a) $\omega/2\theta$ -scan of sample OS98.020, b) $\omega/2\theta$ -scan of sample OS98.022, c) reciprocal space map of the (002) feature of sample OS98.022, and d) reciprocal space map of the (114) feature of sample OS98.022

OS98.022 and sample OS98.020 because of their evident similarities. Both reciprocal space maps have been obtained using slit-optics, which means that sharp peaks, such as the GaN buffer peak, are displayed significantly smeared out in all directions. Only broad features will be portrayed on the correct scale.

The symmetrical (002) reciprocal space map shown in Fig. 4.12 (c) reveals no preferred broadening direction for the superlattice peaks. Lattice dislocations, mosaicity and finite coherence lengths seem to contribute to broadening in every direction. The GaN buffer layer peak is not resolved. The low intensity contours around the GaN peak show no preferred broadening direction either, but that is because of the contributions of the SL1 and SL0 peaks to the diffracted signal.

Figure 4.12 (d) shows the asymmetrical (114) reciprocal lattice feature of sample OS98.022. The reciprocal lattice feature is further away from the origin of reciprocal space. It is enlarged compared to the symmetrical scan. The contribution of the superlattice peaks to the (114) diffraction intensity is so low, that the finite lateral coherence length as the main reason for the broadening of the buffer layer peak becomes apparent. The superlattice peaks do not show up at all. This means no statement about the strain state of the superlattice with respect to the buffer layer can be made. However, fully strained kinematical simulations show a much better agreement than relaxed simulations with the In-composition as given by the growth parameters.

4.6.2 SPECIFIC FINDINGS

It has been shown in Chap. 2 that a wealth of information can be obtained about a superlattice, by simply inspecting the $\omega/2\theta$ diffraction curve as shown in Fig. 4.12 (a) and (b) for samples OS98.020 and OS98.022, respectively. Both scans were taken applying the slit optics of the MRD system to the (002) set of planes of the samples.

Considering only the superlattice and buffer peak positions, the superlattice analyzer program (see Append.) utilizes equations given in Chap. 2 to obtain growth rates, superlattice periods, and In compositions shown in Fig. 4.13 on p. 102. Each sample wafer has been scanned on seven equidistant locations along a diagonal with the end points ($x = -15$ mm, $y = -15$ mm), and ($x = 15$ mm, $y = 15$ mm), where ($x = 0$ mm,

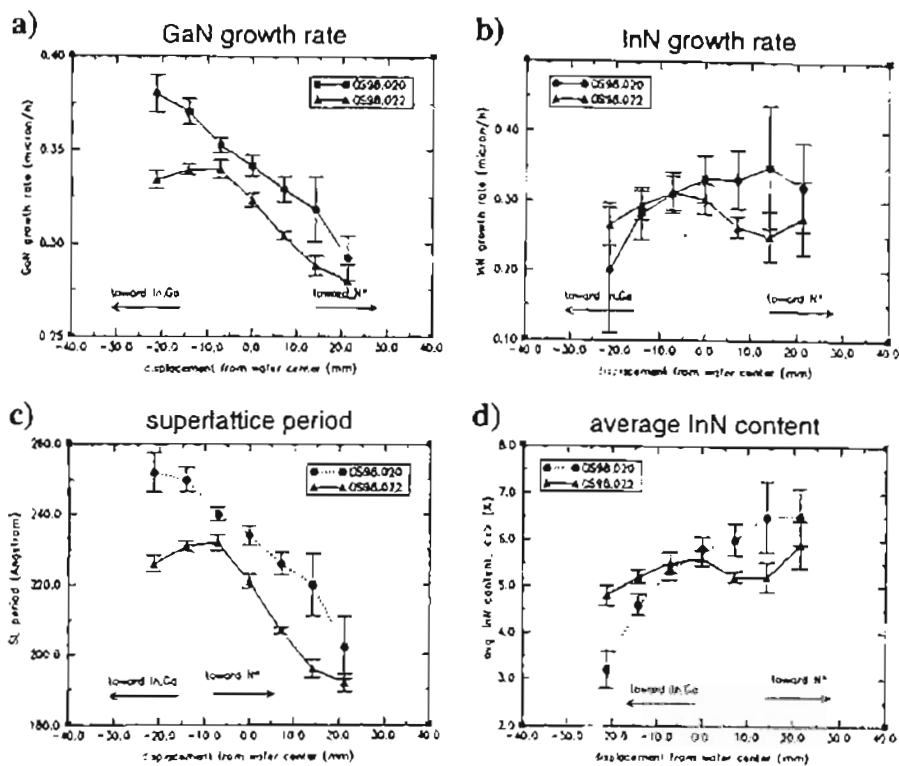


Figure 4.13. *Superlattice Growth Analysis*: The lateral variation of, a) the GaN growth rate, b) the InN growth rate, c) the superlattice period, and d) the average In content of the superlattice in MBE-grown samples OS98.020 and OS98.022 is shown. The data has been calculated using the peak positions of superlattice and substrate in $\omega/2\theta$ -scans along the wafer diagonal, defined by the metal to N flux ratio gradient.

$y = 0$ mm) designates the center of the two-inch sapphire wafer. Along this diagonal the flux ratios of N to Ga and N to In vary. During growth in the MBE system the In and Ga sources are located at the bottom left of the wafer, whereas the N-plasma source is located at the top right, as indicated by Fig. 4.4(b) on p. 79. The wafer does not rotate during growth, so that a spatial analysis may be carried out.

Fig. 4.13 (a) shows the GaN growth along the wafer diagonal during the deposition of the superlattice. For sample OS98.020 GaN assembles itself on the wafer fastest close to the Ga source, and slowest close to the nitrogen source. This behavior strongly suggests a metal-limited growth mode. The higher the metal-flux, the higher the growth rate. For the growth of sample OS98.022 the nitrogen flux has been decreased: Close to the N-source, growth is still metal-limited. However, close to the Ga-source, growth becomes N-limited, as indicated by the lowered growth rate. Despite the higher N gas flow applied during growth of sample OS98.022 (4×10^{-5} Torr) compared to sample OS98.020 (3×10^{-5} Torr), the lowered plasma power (from 400 Watts to 320 Watts) decreases the amount of atomic N. The low plasma power does not break up enough N_2 molecules to yield the same number of N atoms as the lower gas flow with higher plasma power.

One should expect a similar behavior for the InN growth rate depicted in Fig. 4.13 (b), if the metal fluxes were comparable. Sample OS98.020, the one with the higher N-flux, shows a N-limited growth mode close to the In-source, and a metal-limited growth mode close to the N-source, at the same N flux level. The In incorporation of In into the deposited layer should be significantly higher than the Ga incorporation. Looking at the growth rate numbers it is clear that this is not the case. The In atoms have a 60% higher mass than the Ga atoms. Given a steady temperature, the higher mass results in a lowered mobility of In compared to Ga. It takes longer for the In atom to 'find' its place in the crystal lattice, and so the absolute value of the In growth rate does not exceed the Ga growth rate.

If the N-flux is lowered (sample OS98.022), nitrogen-limited growth throughout the wafer should be expected. Considering the big error bars accompanying the data

points obtained from sample OS98.022, this conclusion can neither be confirmed nor disproved by the experimental data.

Fig. 4.13 (c) shows the lateral superlattice variation along the wafer diagonal. Not surprisingly, both curves closely match the GaN growth rates. The time of growth is fixed, so a higher growth rate of the predominant material GaN yields a thicker film. Fig. 4.13 (d) shows the average In content in the superlattice along the wafer diagonal. The average In content curves, of course, match the InN growth rate curves.

In a spatial resolution analysis both, the N-limited, and the metal-limited growth mode, have been seen. 14 data points have been obtained with only two growth runs. X-ray analysis helps to draw valuable conclusions to improve on growth conditions for MBE-grown superlattices.

4.7 SUMMARY

A variety of GaN and InGaN heteroepitaxial thin film samples have been studied. Over the course of the investigation it has become clear that, X-ray diffraction is a very powerful tool in the hands of the semiconductor physicist, who wants to characterize the structural quality and physical properties of epitaxial thin film samples. All samples were grown by MBE or MOCVD. Both growth techniques have been described briefly. Single layer films, GaN on sapphire, GaN on ZnO, and InGaN on sapphire, as well as superlattice structures, InGaN/GaN on sapphire, have been studied.

The first set of samples to be examined were the GaN on sapphire thin films. Rocking curves have been correlated with varying growth parameters, in order to find indications for optimum growth conditions. Two high quality GaN on sapphire samples showed a peculiar, asymmetrical broadening effect in their respective $\omega/2\theta$ -scans, hardly ever reported before. A speculative explanation has been given, considering microscopic defects at layer interfaces, which would partially relieve misfit stress.

Next, GaN single layers on ZnO have been investigated. Due to inferior substrate crystal quality the epitaxial GaN films lack the good quality of the GaN on sapphire samples. Tilt measurements have been performed and a straightforward theory for an ideal tilt has been introduced.

MOCVD-grown InGaN alloy films have undergone a brief study, aimed at the amount of In incorporated within the film. Comparing growth parameters with theoretical models, it has been found that, the InGaN alloy layer grew relaxed on the GaN buffer layer.

High quality MOCVD-grown InGaN/GaN MQW structure samples have been investigated. The intentionally varied parameter during growth was the amount of Si-doping. It has been found that the structural quality of the superlattice depends on the dopant. Reciprocal space mapping proved the coherently strained growth of the superlattice on its buffer layer.

Finally, MBE-grown InGaN/GaN superlattices have been subject to a lateral growth rate variation study, along the wafer diagonal. Results indicate the dependence of growth rates and alloy composition on the flux ratio of the source elements.

CHAPTER 5

SUMMARY AND CONCLUSION

5.1 SUMMARY

In this thesis, a study of epitaxial structure, based on X-ray diffraction, of a number of GaN, InGaN, and related alloys, including both single layers and multilayer heterostructures, has been presented. The fundamentals of X-ray diffraction have been introduced. The XRD experiment has been described. Several different sets of GaN epitaxial heterostructure samples have been investigated, and the respective findings presented. The introductory chapter gave an overview over the current interest in the group III nitride semiconductor materials. There, it has been pointed out that the large, direct bandgaps of the nitrides make them particularly suitable for LED and LD as well as light detector based devices, not only in the visible range of the spectrum, but also into the UV range. A brief research history has been given. Next, Chap. 2 introduced some necessary theoretical background for interpreting the various experimental XRD results which constitute the core work—and unique contributions—of this thesis. Physical effects, occurring within the crystal when an impinging an X-ray beam is present, have been categorized. The kinematical theory has been introduced. To contrast this single scattering approach (kinematical theory), the more rigorous multiscattering approach (dynamical theory) has been briefly described as well. It has been argued that, because of the layer thickness, lattice imperfection, and relative uncertainty of bulk material properties of the samples studied, the kinematical simulation yields a reasonable approximation for the scan data obtained during the investigation. In Chap. 3 the capabilities and limitations of the Philips MRD system have been described. Every scan type employed in this study has been discussed, and interpretations of example scans were

given. Finally, within Chap. 4 the results of the investigation by HRXRD of several sets of GaN and InGaN semiconductor heterostructure samples have been presented.

This work entailed separate studies of several different types of III-N-based samples. An original contribution of this thesis is the conclusive demonstration of improved superlattice interface quality of MOCVD-grown InGaN/GaN structures with increased Si-doping. At present, the physical mechanisms which underlie the interfacial-quality enhancement with Si doping are not understood. One of the first reports on Si-doped InGaN/GaN/AlGaN MQW structures revealed a strict layer interface quality dependence on the amount of n -type Si-doping within the GaN barrier layers of the InGaN/GaN superlattice. The higher the doping concentration (10^{17} to $3 \times 10^{19} \text{ cm}^{-3}$), the better the interface quality. This can be seen by inspecting $\omega/2\theta$ FWHM of higher-order superlattice peaks. The AlGaN capping layer has been shown to have a decisive influence on the peak shape of the diffraction pattern. This has been shown by utilizing the HRXRD simulation program devised for this study. Reciprocal space maps did not show significant differences between the samples studied. All samples exhibit superlattice and capping layers which are coherently strained to the thick GaN buffer layer, which, in turn, appears fully strain-relaxed with respect to the sapphire substrate. The reciprocal space maps suggest a finite in-plane coherence length for the GaN buffer layer, and mosaicity for the superlattice and capping layer peaks as the main effects to cause diffraction signal broadening. In order to gain further insight into the effects of doping within MQWs, the Si-doped MOCVD-grown MQW sample set may be complemented with similar sample sets which utilize, for example, a different n -type dopant species, use of the same (Si) dopant in MBE- rather than MOCVD-grown superlattices, or even a p -type dopant. Such a comparison should prove useful as to which atomic properties are decisive in improving the superlattice quality. Higher doping levels will answer the question of the upper limit on Si doping which still yields a structural quality improvement.

Additionally, MOCVD-grown InGaN-on-sapphire samples have been studied; this sample set appears to exhibit consistency with Vegard's law. The epitaxial films appear to have grown *relaxed* on the substrate. No phase segregation has been observed with In compositions up to 24%.

Recently, the MBE group at Oklahoma State University has successfully grown its first InGaN/GaN superlattices. Two samples in particular have been studied with respect to their different metal (Ga, In)-to-N flux ratios. A lateral growth-rate variation study has been carried out. It has been shown, utilizing a custom-written superlattice analyzer program devised for this purpose, that the growth rates of Ga and In depend critically on the metal-to-N flux ratios during growth. This is a significant phenomenological finding, which remains to be explained. Studies concerning further growth parameters for MBE-grown InGaN/GaN superlattices are in progress and a more complete report will be given elsewhere.⁵¹

Two MBE-grown GaN-on-sapphire samples exhibit an unusual asymmetry in the lineshapes of their (002) $\omega/2\theta$ curves. This has been preliminarily attributed to the contribution of two distinct GaN layers introduced during growth. One sample received a buffer layer before main layer deposition, the other sample has been thermally annealed, and the annealing process may have introduced a 'porous' structure near the surface of the sample due to preferential evaporation. With two distinct layers two diffraction peaks may be seen. The asymmetric peaks can be easily fitted by two Gaussians. The asymmetric peak has rarely been reported, and further investigation is necessary to clarify the origin and physical significance, of this observation. More high-quality single layer GaN samples may be grown to gain conclusive data about a layer separation in single layer GaN samples. A first step would be a thermal annealing study with different after growth flash temperatures for otherwise identical samples.

Yet another set of samples has been investigated: MBE-grown GaN on ZnO epitaxial films. GaN was deposited on the Zn-face of a ZnO substrate. At present, overall quality of the film is not yet comparable to GaN grown on sapphire substrates, due to the necessity for reduced GaN MBE growth temperature, imposed as a consequence of thermal instability of ZnO material at the more typical (high) GaN MBE growth temperatures. A layer-tilt study has been done, and a tilt model for an ideal crystal applied. Results suggest that the present GaN/ZnO samples do not correspond to the simplest,

ideal-tilt case. This conclusion is further supported by the observation of unusually excessive broadening (in comparison to similar GaN on sapphire substrates) in ω and $\omega/2\theta$ scans.

5.2 CONCLUSION

In conclusion, the microstructures of GaN and InGaN semiconductor heterostructures have been investigated through the use of high resolution X-ray diffraction. X-ray diffraction has been shown to be an extremely valuable tool for epitaxial thin film characterization. The methods described yield a wealth of structural information about microstructural characteristics of epitaxial semiconductor multilayers, such as lattice parameters, stress/strain, lattice perfection, and interfacial properties. The original contributions of this thesis have concerned Si-doping dependent structural quality improvements within MOCVD-grown InGaN/GaN/AlGaIn MWQ, and a growth parameter oriented study of MBE-grown InGaN/GaN superlattices. Both investigations concern themselves with structural quality improvement. The findings presented in this thesis could provide a potentially important contribution to the growth of high-structural-quality, device-oriented heteroepitaxial semiconductors. Historically, high microstructural crystal quality yielded high efficiency electronic and optoelectronic devices. Studies of this sort are essential to support continued progress in the area of semiconductor research. Achievable goals—blue LDs and LEDs as well as high-temperature, high-power electronic devices—lie in the near future for the GaN family of materials; such technological advances will have a continued impact on the way electronics continues to change our way of life.

BIBLIOGRAPHY

1. Riordan, M. , Hoddeson, L., "Crystal Fire - The Birth of the Information Age", W. W. Norton and Company, London New York (1997).
2. Orton, J. W., Foxon, C. T., Rep. Prog. Phys. 61 (1998).
3. Nichia Chemical Industries, LTD., "Optoelectronic Product Guide", (10/1996).
4. Nakamura, S., Senoh, M., Iwasa, N., Nagahama, S., Yamada, T., Mukai, T., Jpn. J. Appl. Phys. 34, L1332 (1995).
5. Nakamura, S., Senoh, M., Nagahama, S., Iwasa, M., Yamada, T., Matsushita, T., Sugimoto, Y., Kiyoku, H., Appl. Phys. Lett. 69, 4056 (1996).
6. Lim, B. W., Chen, Q. C., Yang, J. Y., Khan, M. A., Appl. Phys. Lett. 68, 3761 (1996).
7. Wu, Y. F., Keller, B. P., Keller, S., Kapolnek, D., Kozodoy, P., DenBaars S. P., Mishra, U. K., Appl. Phys. Lett. 69, 1438 (1996).
8. Yang, X. H., Schmidt, T. J., Shan, W., Song, J. J., Goldenberg, B., Appl. Phys. Lett. 66, 1 (1995).
9. Metzger, R. A., Compound Semicond. 1, 26 (1995).
10. Goldenberg, B., Zook, J. D., Ulmer, R. J., "Topical Workshop on III-V Nitrides", Abstract E-3, Nagoya, Japan (09/1995).
11. Madelung, O., "Physics of III-V Compounds", Wiley, New York (1964).
12. Edgar, J. H., (ed), "Properties of Group III Nitrides" (EMIS Data Review Series 11), London, INSPEC IEE (1994).
13. Grzegory, I., Jun, J., Bockowski, M., Krukowski, S. T., Wroblewski, M., Lucznik, B., Porowski, S., J. Phys. Chem. Solids, 56, 639 (1995).
14. Ilegems, M., Montgomery, H. C., J. Phys. Chem. Solids 34, 885 (1973).
15. van de Walle, C. G., Neugebauer, J., Mat. Res. Soc. Symp.Proc. 449, 861 (1997).
16. Akasaki, I., Amano, H., Koide, Y, Hiramatsu, K., Sawaki, N., J. Cryst. Growth 98, 209 (1989).

17. Nakamura, S., Senoh, M., Mukai, T., Japan J. Appl. Phys. 30, L1708 (1991).
18. Amano, H., Kito, M., Hiramatsu, K., Akasaki, I., Japan. J. Appl. Phys. 28, L2112 (1989).
19. Nakamura, S., Iwasa, N., Senoh, M., Mukai, T., Japan. J. Appl. Phys. 31, 1258 (1992).
20. Moustakas, T. D., Molnar, R. J., Mater. Res. Soc. Conf. Proc. 281, 753 (1993).
21. von Laue, M., Fridrich, W., Knipping, P., "Münchener Sitzungsberichte" 303 (1912) and Ann. Physik 41, 971 (1913).
22. Kittel, C "Introduction to Solid State Physics", John Wiley & Sons, Inc., New York, sixth edition (1986).
23. Ashcroft, N. W., Mermin, N. D. "Solid State Physics", Holt, Rinehart, and Winston, New York (1976).
24. Zachariasen, W. H., "Theory of X-Ray Diffractions in Crystals", Wiley, New York (1945).
25. Pinsker, Z. G., "Dynamical Scattering of X-Rays in Crystals", Springer Verlag, Berlin Heidelberg New York (1978).
26. Cullity, B. D., "Elements of X-Ray Diffraction", Addison-Wesley, London Amsterdam Sidney (1956).
27. Bauer, G., Richter, W., "Optical Characterization of Epitaxial Semiconductor Layers", Springer Verlag, Berlin Heidelberg New York (1996).
28. Bartels, W. J., J. Vac. Sci. Technol. B1 338 (1983).
29. Landolt, Börnstein, "New Series".
30. Lipson, H., Taylor, C. A., "Fourier Transforms and X-Ray Diffraction", Bell and Sons, London (1958).
31. International Union of Crystallography, "International Tables for X-Ray Crystallography, Vol.3", Kynoch, Birmingham England, (1962).
32. Darwin, C. J., Philos. Mag. 28, 315 and 675 (1914).
33. Ewald, P. P., Ann. Physik 54, 519 (1917).
34. von Laue, M., "Ergebnisse d. exakt. Naturwiss. 10, 133 (1931).
35. Prins, J. A., Zeit. f. Physik 63, 477 (1930).
36. Takagi, S., Acta Cryst. 15, 1311 (1962).

37. Takagi, S., *J. Phys. Soc. Japan* 26, 1239 (1969).
38. Taupin, D., *Bull. Soc. Fr. Mineral. Crystallogr.* 87, 469 (1964).
39. Chen, Y. C., Bhattacharya, P. K., *J. Appl. Phys.* 73, 7389 (1993).
40. Philips HRS Manual.
41. Kervarac, J., Baudet, M., Caulet, J., Auvray, P., Emery, Y. Y., Regreny, A., *J. Appl. Cryst.* 17, 196 (1984).
42. Fewster, P. F., *Philips J. Res.* 41, 268 (1986).
43. Fleming, R. M., Mc Whan, D. B., Gossard, A. C., Wiegemann, W., Logan, R. A., *J. Appl. Phys.* 51, 357 (1980).
44. Philips PC-MRD Manual.
45. DuMond, W. M., *Phys. Rev.* 52, 872 (1937).
46. Beaumont, J. H., Hart, M., *J. Phys. E7*, 823 (1974).
47. Philips MRD System Software.
48. Philips MRD Installation Manual.
49. Warren, B. E., "X-Ray Diffraction", Addison-Wesley, Reading, MA (1969).
50. Yu, P. Y., Cardona, M., "Fundamentals of Semiconductors", Springer Verlag, Berlin Heidelberg New York (1996).
51. O'Steen, M. L., Ph.D. Dissertation, OSU (1999)
52. Zhu, Q., *Appl. Phys. Lett.* 68 (8), 1141 (1996).
53. Guha, S., Bojarczuk, N. A., Kisker, D. W., *Appl. Phys. Lett.* 69 (19), 2879 (1996).
54. Nagai, H., *J. Appl. Phys.* 43, 4254 (1972).
55. Nagai, H., *J. Appl. Phys.* 45, 3789 (1974).
56. Lee, C., Chi, G. C., Lin, C. F., Feng, M. S., Guo, J. D., *Appl. Phys. Lett.* 68 (24), 3440 (1996).
57. Cho, Y. H., Fedler, F., Hauenstein, R. J., Park, G. H., Song, J. J., Keller, S., Mishra, U.K., DenBaars, S. P., *J. A. P. Communications* (submitted).
58. Bidnyk, S., Schmidt, T. J., Cho, Y. H., Gainer, G. H., Song, J. J., Keller, S., Mishra, U.K., DenBaars, S. P., *Appl. Phys. Lett.* 72, 1623 (1998).
59. Keller, B. P., Keller, S., Kapolnek, D., Jiang, W. -N., Wu, Y. -F., Masui, H., Wu, X. H., Heying, B., Speck, J. S., Mishra, U.K., DenBaars, S. P., *J. Electron. Matter* 24, 1707 (1995).

60. Keller, B. P., Abare, A. C., Minsky, M. S., Wu, X. H., Mack, M. P., Speck, J. S., Hu, E., Coldren, L. A., Mishra, U.K., DenBaars, S. P., "Proceedings of the 7th International Conference of Silicon Carbide, III-Nitrides and Related Materials", Stockholm, Sweden (1997); Materials Science Forum 264-268, 1157 (1998) 114
61. Ruvimov, S., Liliental-Weber, Z., Suski, T., Ager III, J. W., Washburn, J., Krueger, J., Kisielowski, C., Weber, E. R., Amano, H. Akasaki, I., Appl. Phys. Lett. 69, 990 (1996).
62. Osten, H. J., Klatt, J., Lippert, G., Dietrich, B., Bugiel, E., Phys. Rev. Lett. 69, 450 (1992).
63. Eaglesham, D. J., Unterwald, F. C., Jacobson, D. C., Phys. Rev. Lett. 70, 966 (1993).
64. Tapfer, L., Stolz, W., Ploog, K., J. Appl. Phys. 66, 3217 (1989).

APPENDICES

APPENDIX A

HRXRD SIMULATION MANUAL

A.1 INTRODUCTION

A.1.1 ACKNOWLEDGMENTS

I would like to thank my advisor Dr.R.J.Hauenstein and my fellow student Mark.L.O'Steen, for encouragement and insights into the underlying theory. Without them, this work would not have been accomplished.

Though I have never met him, thanks to P.J.Turner for giving the world xvgr. I use it a lot. The same goes for T.C. Zhao and Mark Overmars. These guys created the forms library which makes all the fine looking X -windows windows possible. Long live the Linux community!

A.1.2 INTRODUCTION

This program came into existence because there was no other like it. I was working on X-ray characterization of GaN epitaxial thin films, when I realized, that all simulation software out there only could handle cubic structures. So I was stuck with my hexagonal crystal and a cubic simulation. What is the way out? Do it yourself (Fig. A.1)!

The second section will give an insight into the internal file management of the program. Section A.3 gives a few hints about using the X-windows interface. The program code is to be found in Section A.4.

A.1.3 WHAT THIS PROGRAM CAN DO

Fritz's High Resolution X-Ray Diffraction supplies an easy to use Linux X-Windows based user interface, which allows for a fast change of sample and/or scan setup parameters. The kinematical approach allows very fast computation of X-ray diffraction intensities of hexagonal lattice structures with - at least in my experience - no lack of accuracy compared to dynamical theory within experimental constraints.

The program provides forms which collect the necessary data: material properties, sample structure and scan setup. Given this, a simulated intensity depending on the Bragg angle is produced and shown. In a second step you can compare experimental and theoretical data directly and print out the result.

Any reflection of a Miller plane (hkl) may be simulated. For off axis scans it is assumed that the growth direction (perpendicular to the sample surface) coincides with the crystallographic [001] or *c* direction.

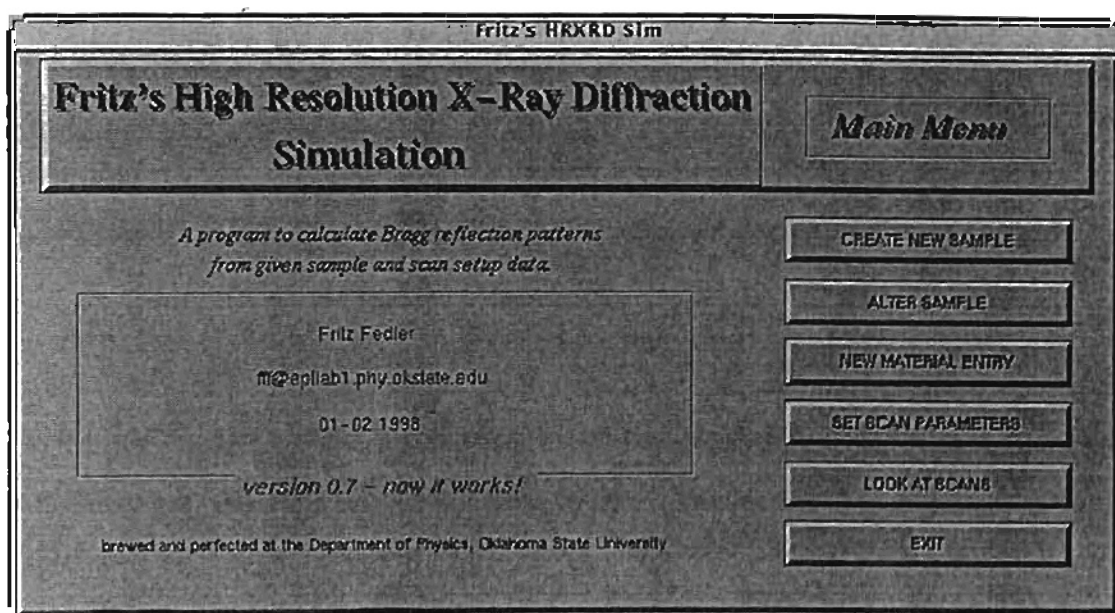


Figure A.1. *Startup Window: Let the simulations begin...*

A.2 PROGRAM DETAILS

A.2.1 INSTALLATION

Put the file `XRDsim08.tgz` in your home directory. Expand it with

```
tar -xvzf XRDsim08.tgz
```

This will create the subdirectory *XRDsim*. It contains all necessary files and a few data file subdirectories. That's it! Change into *XRDsim* and start the program with **XRDsim**.

Note: To use the graphical capabilities of the program you will have to have **xvgr** installed on your system.

A.2.2 DATA FILES

All data files used are easy to manipulate *ASCII* files. Usually the X-windows interface should be sufficient to do the job. However, situations may occur where you want direct control. When naming the files be sure to not exceed 50 characters for path+filename. That means the filename must be smaller than 40 characters (this restraint may be changed in a later version).

After installation, you will notice the following subdirectories in your *XRDsim* directory:

A.2.2.1 THE 'INDATA' DIRECTORY. This directory contains all necessary data for the simulation process.

MATERIAL FILES

.mat files contain material specific data. Here material means an element or compound, which has a hexagonal crystal structure. It is the smallest building block for your sample to be. All parameters describing the material in effect describe properties of its lattice.

Example: **GaN.mat**

```

3.189      : lattice parameter a
5.185      : lattice parameter c
1.2962     : atomic basis offset for N with respect to Ga
31.534     : atomic form factor parameters for Ga
-49.1962
35.2891
-9.61512
7.020234   : atomic form factor parameters for N
-19.4321
22.0819
-8.53549
19000      : penetration depth in Angstroms if used as substrate
11.4       : stiffness constants C13
36.5       : C33

```

This is the file as you find it on your harddrive. The colon as comment sign is arbitrary. The program will read data in every line until it hits a space character. From there on the rest of the line is dismissed. All lengths you might come across are given in Ångstroms. This includes the here shown lattice parameters, basis offset and X-ray penetration depth.

Following usual convention the hexagonal lattice parameter a is the one in plane, and the c lattice parameter is the one in (001) direction.

The atomic basis offset is the distance u between the two basis atoms of the Wurzite structure.

The atomic formfactors (given in $\sin[\text{Bragg angle}] / \text{X-ray wavelength}$) are fitted with a third grade polynome. The numbers shown are the coefficients for x^0, x^1, x^2, x^3 respectively*

*Data points for curve fitting are taken from the book by Cullity .²⁶

The X-ray penetration depth is given in Ångstroms. This is important to calculate the reflected intensity if the material is used as a substrate. Epitaxial layers are assumed thin, such that every atomic layer reflects the same intensity.

The material specific stiffness constants are taken from up to date literature. The units are not important, since only the quotient enters the computation.

SAMPLE FILES

Another kind of files you find in the *indata* directory are the *.sam* files. These describe the samples from which a scan is to be simulated. The following example has been created by the program.

Example: **InGaN_SL.sam**

```

GaN      : substrate material
2        : # of super lattices
1.000000 : # of layers in SL
1.000000 : # of repetitions of this SL
GaN      : material 1
AlN      : material 2
0.049000 : composition coefficient for material 2
1055.000000 : thickness
2.000000 : # of layers in SL
12.000000 : # of repetitions of this SL
GaN      : material 1
InN      : material 2
0.099000 : composition coefficient for material 2
40.000000 : thickness
GaN      : material 1
          : material 2
0.000000 : composition coefficient for material 2
40.000000 : thickness

```

The first line tells you the substrate material. The remaining structure of the sample is described by a series of superlattices, which are subdivided in a number of layers. The layers are specified with their respective material and thickness. Lastly, each superlattice is given a number of repetitions.

For the above example, you see a GaN substrate, on top of which you have two superlattices. The first superlattice consists of one layer of $\text{Al}_{0.049}\text{Ga}_{1-0.049}\text{N}$ with a thickness of 1055 Ångstroms. This one layer superlattice is repeated only once - you just have defined a single layer as superlattice.

Similar, the second superlattice has two layers, one of which is $\text{In}_{0.099}\text{Ga}_{1-0.099}\text{N}$ with a thickness of 40 Ångstroms. The second layer of the second superlattice is pure GaN, likewise 40 Ångstroms thick. This superlattice is repeated 12 times.

Only AB compounds can be used as sample layers. That is why the third material 2 line is empty, but still there. Three or more materials in one layer are not possible. Also, note that the composition coefficient x in A_xB_{1-x} is given in parts of 1, not in per cent.

SCAN FILES

The third kind of files in the indata directory are the **.dat** files. These contain the final scan setup, which is then handed over to the **XRDsim_core** program, which does the simulation computation. Thus, it is possible to run the simulation without the X-windows user interface. It is as easily readable as the others are.

Example: **InGaN_SL.dat**

```

1.540597      : x-ray wavelength [Angstrom]
17.285000     : theta angle about which to scan [deg]
5.000000     : scan range [deg]
0.001000     : stepsize [deg]
0.000000     : h
0.000000     : k
2.000000     : l
GaN          : substrate material

```

2.000000 : # of SL's
 1.000000 : # of repetitions of 1st SL
 1.000000 : # of layers in 1st SL
 AlN49GaN : temporary material file
 1055.000000 : thickness of 1st layer in 1st SL
 2.000000 : # of layers in 2nd SL
 12.000000 : # of repetitions of 2nd SL
 InN99GaN : material of 1st layer in 2nd SL
 40.000000 : thickness of 1st layer in 2nd SL
 GaN : material of 2nd layer in 2nd SL
 40.000000 : thickness of 2nd layer in 2nd SL

The first seven lines of this scan file contain the scan setup including the Miller indices of the Bragg planes aimed at. Only reflections from these planes are considered in the simulation. You notice that the second part of this file only contains data already given in the sample file. For 'historical reasons' the core program only understands single material layers. The temporary files **AlN49GaN.tmp** and **InN99GaN.tmp** contain linearly extrapolated material data calculated from the original material files. If strained simulation in the X-windows user interface is chosen, changes in lattice parameters are introduced in these temporary files. Temporary files are saved in the *indata* directory and deleted immediately after the calculation.

A.2.2.2 THE 'OUTDATA' DIRECTORY. The *outdata* directory contains only **.out** files. These contain the generated intensity distribution depending on the Bragg angle. The first column holds the angle in degrees, the second, set apart by a space character, holds an arbitrary X-ray intensity counts per second for that angle*. For easier further data processing, the *outdata* file does not contain any comments. It therefore is

*The output is normalized to 340,000 cps, which is the unreflected count rate of my XRD system.

a good habit to name the **.out** files similar to the scan files (**.dat**), which contain all necessary information. For example, **InGaN_SL.dat** should correspond to **InGaN_SL.out**.

A.2.2.3 THE 'XRDCANS' DIRECTORY. It is suggested to put experimental scan data in this directory. *Fritz's XR/RD Simulation* allows for direct comparison of experimental and theoretical data. The program will by default first look into this directory.

The data files should be readable by **xvgr** with the same format as the simulated file. For details about comments within the data file, see the **xvgr** documentation.

A.2.2.4 THE 'XVGR' DIRECTORY. This directory is intended for saving final graphs formatted with **xvgr**.

A.3 USING THE X-WINDOWS INTERFACE

A.3.1 INTRODUCTION

The X-Window interface is an assembly of forms, which make it easy to create all the necessary files, discussed in the previous section. The window environment coordinates the execution of simulations and pipes the resulting data into the graphical data processing program *xvgr*.

A.3.2 MAIN MENU

After starting *Fritz's HRXRD Simulation* with the command **XRDSim**, the main menu will pop up. It is pretty much self-explanatory. I will discuss every menu item by itself.

A.3.2.1 CREATE NEW SAMPLE. Before you can simulate anything, a sample entry has to be made. The program has to know what sample structure you intend to shoot your X-rays at.

As described in Section A.2.2.1.2, each sample is described as a series of superlattices put on top of a substrate material.

After choosing Create New Sample in the main menu the window *Sample Structure Input* appears. Type in the substrate material for your sample. The Check button allows you to see the materials you can choose from. Do only use the first part of the shown file names (*GaN* not *GaN.mat*).

Next, enter the number of superlattices. Note that even a single layer has to be assigned to one superlattice (see 2.2.1.2). Hit [Return] or use the Enter Layers button to open the *Superlattice* window. Now you can define the number of layers for the first superlattice and the number of repetitions of these layer(s). For a single layer, it is 1 and 1. Hit [Return].

The next window takes the data for every layer of the superlattice. The material 2 entry is optional. The compositional factor x refers to material 2 and is to be given in parts of 1, not in per cent (e.g. for an *AB* material compound with 22.2% *B* \Rightarrow

$x=0.222$). Leave x blank if you do not have a second material. The layer thickness must be provided in Ångstroms. Hit the Done button. Windows keep popping up until all superlattices are filled with life.

The last step is to give your sample a name (again, *sample* not **sample.sam**). With Check, you can find out which sample names are already taken.

Note: The Check button file selectors do not select files or names. Here they just show filenames.

A.3.2.2 ALTER SAMPLE. With Alter Sample, you get the sample structure with one view. Select the sample you want to edit or review. The *Sample Structure* window appears. You may edit any field. The same conventions as before apply.

Note: For some reason sometimes weird characters appear in one or more boxes appended to the numbers shown. This bug may be limited to my computer only, however, be sure to delete these since the sample structure is saved as seen when you close the window.

A.3.2.3 NEW MATERIAL ENTRY. The *Material Input Form* window takes all necessary data to describe a material. The conventions mentioned in 2.2.1.1 apply.

The material name again is the filename without extension.

A.3.2.4 SET SCAN PARAMETERS. After all these preparations, it is now time for the scan simulation. The *Scan Setup Form* asks you for the X-ray wavelength to be used as well as for the angle about which to center the scan, the scan range, and the angular step width. Finally, the Miller indices of the planes you want to look at are needed.

Since I work on *GaN* epitaxial layers in my lab, the form is preset for a symmetric 5-degree sweep over the according Bragg angle for (002) planes.

If the Strain button is highlighted (green) the simulation considers the epitaxial layers fully strained with respect to the given substrate material. With the green light off, a fully relaxed Superlattice is assumed.

Choose a sample (you may pick one with the *Check* file selector) and name the scan output file.

Hit the *EXECUTE* button. After the calculation is finished, *xvgr* will pop up with a graph of the scan.

A.3.2.5 LOOK AT SCANS. Two file selectors let you choose an experimental data file and a simulated data file. By default, the experimental file is looked for in the *xrdscans* directory. *xvgr* will now show both curves. From here you can manipulate and print or save graphs. Refer to the *xvgr* manual for details. An example is shown in the figure.

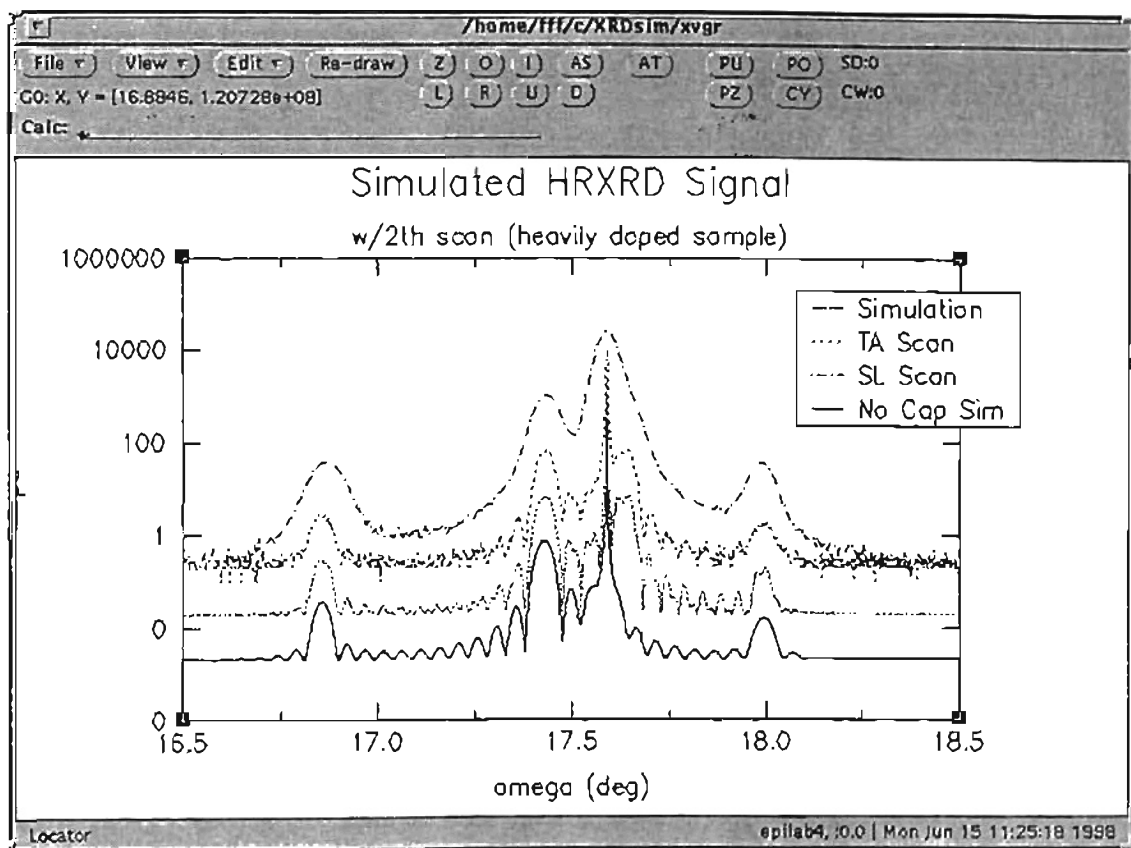


Figure A.2. An example for a simulation presentation with xvgr.

A.4 HRXRD SIMULATION PROGRAM CODE

The program is subdivided into several code files. Only three of them are of technical significance to the simulation process and will be listed here.

A.4.1 MAIN CODE FILE

The file printed below is **XRDSim.c**. It links all code files and handles the last main menu item *Look at Scans*.

```
/*  
This is the main file of the hcp XRD simulation project.  
This segment combines the core program with the X-Forms  
interface.  
The package will calculate the diffraction pattern for a  
fully relaxed or fully strained heteroepitaxial super-  
lattice with given despadding, theta (range), phi, lamda,  
lattice constants (a,c), formfactors, lattice basis and  
layer thicknesses for n materials in m periods. [001] is  
considered the plane parallel to the surface. Input of  
material, sample and scan setup parameters as well data to  
simulation comparison is facilitated.  
  
ver0.1 (12/97)  
ver0.2 (01/98) main menu crash while looking at data  
eliminated  
ver0.3 (01/98) added fileselectors for looking at files and  
scan input  
ver0.4 (02/98) added "alter sample" subroutine  
ver0.5 (02/98) looking at data crash eliminated,
```

comparing sim and mrd data enabled
ver0.6 (02/98) added fully strained sim. capability and
toggle switch fully strained/fully relaxed
ver0.7 (02/98) removed long sample name crash;

known problems: noisy signal for repetition of very thick
layers (core problem)

Fritz Fedler

02/25/98

*/

```
#include "forms.h"
#include <stdio.h>
#include <stdlib.h>
#include <string.h>

#include "include/material_INCLUDE.h"
#include "include/sample_INCLUDE.h"
#include "include/scan_INCLUDE.h"
#include "include/start_INCLUDE.h"
#include "include/alter_sample_INCLUDE.h"

int show_data_file()
{
char
path_sim[100], file_sim[100], path_sc[100], file_sc[100], sysarg[200];

if(fl_show_fselector("Existing Output Files",
                    "outdata/", "*.out", "") != NULL)
```

```

    {
        sprintf(path_sim, "%s/", fl_get_directory());
        sprintf(file_sim, "%s", fl_get_filename());
        strcat(path_sim, file_sim);
        if(fl_show_fselector("Scan to compare
to", "xrdscans/", "*.x*", "") != NULL)
    {
        sprintf(path_sc, "%s/", fl_get_directory());
        sprintf(file_sc, "%s", fl_get_filename());
        strcat(path_sc, file_sc);
        sprintf(sysarg, "xvgr %s %s -p
xvgr/param", path_sim, path_sc);
        system(sysarg);
    };
    };
};

int main (int argc, char *argv[])
{
    FD_start *form;          /* holds above start form definition*/
    FL_OBJECT *action;
    char sysarg[200];
    char dummy[100];
    char outfile[100]="outdata/";
    int i=0;

    fl_initialize(&argc, argv, "FormDemo", 0, 0);
    form = create_form_start();
    fl_show_form(form-
>start, FL_PLACE_CENTER|FL_FREE_SIZE, FL_TRANSIENT,

```

```

        "Fritz's HRXRD Sim");
while (form->done != (action=fl_check_forms())){
    if(action == form->xvgr){
        show_data_file();
    };
    if(action == form->sample){
sample_in();};
    if(action == form->alter_sample){
        alter_sample("single");};
    if(action == form->mat){
create_material_file();};
    if(action == form->scan){
create_control_file(outfile);};
};

}

```

A.4.2 SCAN SETUP CODE

The `scan_INCLUDE.c` file processes all input data to make a file readable by the core program. Note the linear calculation of a mixed material file if the strained simulation flag is set.

The first two functions are left out. They consist of code specific to the *forms* library (window programming).

```

/*
scan_setup include file for XRDsim: This include creates a
combined material file from two given input materials and
builds the control file which is used by the core program.

```

Fritz Fedler

1/16/98

*/

```
#include <stdlib.h>
```

```
#include <stdio.h>
```

```
#include "forms.h"
```

```
#include "scan_setup.h"
```

```
#define EOL '\n'
```

```
#define EOS '\0'
```

```
FILE *fpin;
```

```
FILE *fpcompin;
```

```
FILE *fpout;
```

```
FILE *fpcompout;
```

```
FD_scan_setup *create_form_scan_setup(void)
```

```
{
```

```
CODE INTENTIONALLY LEFT OUT
```

```
}
```

```
FD_working *create_form_working(void)
```

```
{
```

```
CODE INTENTIONALLY LEFT OUT
```

```
}
```

```
char *GetLine(char *receiver) /* read one line out of file at  
fpin */
```

```
{
```

```
/* copy result in given variable
```

```
*/
```

```

char a,temp[100];
int c=0;
temp[c]=fgetc(fpin);
while ((temp[c]!=EOL)&&(temp[c]!=EOF)) { temp[++c]=fgetc(fpin);
}
temp[++c]=100;
strncpy(receiver,temp,16);
}

```

```

/***** read a line from input material file
*****/

```

```

char *GetLineComp(char *receiver)
/* read one line out of file at fpcompin*/
{
/* copy result in given
variable */
char a,temp[100];
int c=0;
temp[c]=fgetc(fpcompin);
while ((temp[c]!=EOL)&&(temp[c]!=EOF))
{ temp[++c]=fgetc(fpcompin); }
temp[++c]=100;
strncpy(receiver,temp,16);
}

```

```

/***** read data from material data files using GetLine
*****/

```

```

int read_mat(char material[20],float *line)

```



```

{
int n,i,j=0;
char filename[20] = "indata/";
char receiver[16];
    strcat(strcat(filename,material),".mat");
    fpcompin = fopen(filename,"r");
    for (i=0; i<=22; i++) {
        GetLineComp(receiver);
        if (isdigit(receiver[0]) || receiver[0]=='-')
            line[i] = atof(receiver);
    }
fclose(fpcompin);
}

/***** calculate and save mixed material file
*****/

char *create_compound(char *substrate,char *mat1, char *mat2,
float x, int strain_flag) {
char filename[30] = "indata/";
char xvalue[4];
float substrate_data[14], material_data[3][14];
float a_layer,a_sub,c_layer,c_sub,C13,C33;
int i=0;

printf("\nENTER create_compound\n");

read_mat(mat1,material_data[1]);

```

```

read_mat(mat2,material_data[2]);

for(i=0;i<=13;i++){
    material_data[0][i] = (1-
x)*material_data[1][i]+x*material_data[2][i];
};

if(strain_flag==1){
printf("\nSUBSTRATE: %s\n",substrate);
read_mat(substrate,substrate_data);
for(i=0;i<=13;i++){
    printf("%f\t\n",substrate_data[i]);
};
a_layer=material_data[0][0]; c_layer=material_data[0][1];
C13=material_data[0][12]; C33=material_data[0][13];
a_sub=substrate_data[0]; c_sub=substrate_data[1];
material_data[0][0]=a_sub;
/** define new a and c for layer */
material_data[0][1]=c_layer*(1-2*C13/C33*(a_sub-
a_layer)/a_layer);
printf("\nexecuted option FULLY STRAINED\n");
};

if(x>0){ /** for 2 material compound */
i=(int)1000*x; sprintf(xvalue,"%d",i);
strcat(strcat(strcat(strcat(filename,mat2),xvalue),mat1),
".tmp");
fpcompout = fopen(filename,"w");
for(i=0;i<=13;i++){
    fprintf(fpcompout,"%f\t\n",material_data[0][i]);
};
};

```

```

};
fclose(fpcompout);
strcpy(mat1, strcat(strcat(mat2, xvalue), mat1));
};
if(x==0){
strcat(strcat(filename, mat1), ".tmp");
    fpcompout = fopen(filename, "w");
    for(i=0; i<=13; i++){
        fprintf(fpcompout, "%f\t\n", material_data[0][i]);
    };
    fclose(fpcompout);
};
return(mat1);
}

/***** build control file to process the scan
*****/

char *create_control_file(char *outdata_file)
{
FD_scan_setup *form; /* holds above scan_setup form definition
*/
FD_working *form1;
FL_OBJECT *action;
char filein[100]="indata/";
char fileout[100]="indata/";
char dummy[100];

```

```

char sample_materials[100][10];
char sysarg[200];
float sample_data[300];
int strain_flag, cancel, n, i, j=0;
char receiver[16]="1";
char mat1[100], mat2[100], substrate[100];
float xvalue;

form = create_form_scan_setup();
form1 = create_form_working();

fl_set_input(form->lambda, "1.540597");
fl_set_input(form->theta, "17.285");
fl_set_input(form->range, "5");
fl_set_input(form->step, "0.001");
fl_set_input(form->h, "0");
fl_set_input(form->k, "0");
fl_set_input(form->l, "2");

fl_show_form(form->scan_setup, FL_PLACE_MOUSE, FL_TRANSIENT,
             "Fritz's HRXRD Sim");

/***** read data from interface and store scan file
*****/

cancel=0; strain_flag=1;
while (cancel!=1){
    action=fl_do_forms();
    if(action == form->cancel){
fl_hide_form(form->scan_setup);

```

```

cancel=1;});
    if(action == form->check_sample_files) {
if(fl_show_fselector("Existing Sample Files",
                    "indata/", "*.sam", "") != NULL)
    {
        sprintf(dummy, "%s", fl_get_filename());
dummy[strlen(dummy)-4] = '\0';
        fl_set_input(form->sample_file, dummy);
    };
};
    if(action == form->check_scan_files) {
        if(fl_show_fselector("Existing Scan Files",
                            "outdata/", "*.out", "") != NULL)
            {
                sprintf(dummy, "%s", fl_get_filename());
dummy[strlen(dummy)-4] = '\0';
                fl_set_input(form->scan_file, dummy);
            };
};
    if(action == form->strain){
if(strain_flag==0) strain_flag=1; else strain_flag=0;
    };
    if(action == form->done){
fl_hide_form(form->scan_setup);
fl_show_form(form1->working, FL_PLACE_CENTER, FL_TRANSIENT,
            "Fritz's HRXRD Sim");

strcat(strcat(filein, fl_get_input(form->sample_file)), ".sam");
fpin = fopen(filein, "r");
strcat(strcat(fileout, fl_get_input(form->scan_file)), ".dat");

```

```

fpout = fopen(fileout, "w");

fprintf(fpout, "%f \t\t", atof(fl_get_input(form->lambda)));
fprintf(fpout, ": x-ray wavelength [Angstrom]\n");
fprintf(fpout, "%f \t\t", atof(fl_get_input(form->theta)));
fprintf(fpout, ": theta angle about which to scan [deg]\n");
fprintf(fpout, "%f \t\t", atof(fl_get_input(form->range)));
fprintf(fpout, ": scan range [deg]\n");
fprintf(fpout, "%f \t\t", atof(fl_get_input(form->step)));
fprintf(fpout, ": stepsize [deg]\n");
fprintf(fpout, "%f \t\t", atof(fl_get_input(form->h)));
fprintf(fpout, ": h\n");
fprintf(fpout, "%f \t\t", atof(fl_get_input(form->k)));
fprintf(fpout, ": k\n");
fprintf(fpout, "%f \t\t", atof(fl_get_input(form->l)));
fprintf(fpout, ": l\n");

/***** paste data from sample file *****/

GetLine(receiver);

n=((int) index(receiver, ' '))-((int)receiver);
strncpy(substrate,receiver,n); substrate[n] = '\0'; mat2[0] =
'\0';
fprintf(fpout, "%s
\t\t\n", create_compound(substrate, substrate, mat2, 0, 0));

while(receiver[0]!=EOF && receiver[0]!=EOL && receiver[0]!=EOS) {
GetLine(receiver);
    if (isdigit(receiver[0]) || receiver[0]=='-')

```

```

        { fprintf(fpout, "%f \t\t\n", atof(receiver)); };
    if (isalpha(receiver[0]))
        { n=((int) index(receiver, ' '))-((int)receiver);
    strncpy(mat1,receiver,n);
    mat1[n] = '\0';
    GetLine(receiver);
    n=((int) index(receiver, ' '))-((int)receiver);
    strncpy(mat2,receiver,n);
    mat2[n]='\0';
    GetLine(receiver);
    xvalue = atof(receiver);
    fprintf(fpout, "%s \t\t\n", create_compound(substrate,
mat1,mat2,xvalue, strain_flag));
    printf("\nIN create_compound: SUBSTRATE: %s\n",substrate);
};

    }

fclose(fpin);
fclose(fpout);

/***** process scan file and show result
*****/

for(i=0;i<=23;i++){
fileout[i]=fileout[i+7];};
strcat(strcat(strcpy(outdata_file, "outdata/"),
fl_get_input(form->scan_file)), ".out");
sprintf(sysarg, "XRDSim_core %s > %s", fileout, outdata_file);
system(sysarg);

```

```
system("rm indata/*.tmp");
sprintf(sysarg, "xvgr -log y %s", outdata_file);
fl_hide_form(form1->working);
system(sysarg);

return(outdata_file);

}; /*end of while statement */
}; /*end (read data) while*/
}
```


A.4.3 SIMULATION COMPUTATION CODE

This is the `XRDSim_core.c` listing. It includes all necessary computational code for kinematical theory scattering simulation.

```
/*
This is the CORE program of the hcp XRD simulation project.
This segment will calculate the diffraction pattern for a
super lattice with given despadding, theta (range), phi,
lamda, lattice constants (a,c), formfactors, lattice basis
and layer thicknesses for n materials in m periods.
[001] is considered the plane parallel to the surface.

ver0.1   11/97
ver0.3   12/97 eliminate crashing for certain scan angles
ver0.9   12/97 add substrate simulation
ver0.91  01/98 eliminate wrong outcome for pure substrate
simulation
ver0.93  01/98 eliminate crash for certain multilayer
samples
ver0.94  02/98 eliminate wrong outcome for single
material samples, add small cps safety
routine
ver0.95  02/98 enable long input filenames (avoids crash
for long sample file names)

known problems: "noisy" outcome for repetitions of very
    thick layers

Fritz Fedler
```

02/23/98

*/

#include <stdio.h>

#include <stdlib.h>

#include <string.h>

#include <math.h>

#include "complex.h"

#include "hkl_INCLUDE.h"

#define EOL '\n'

#define EOS '\0'

FILE *fpin;

FILE *fpout;

/* functions */

double super_lattice_reflection(char *scanfile, double *theta_dat,
double

*intensity, int *dat_pts);

int read_indata(char file[100], double *line, char
material_file[30][100]);

char *GetLine();

double absmod(double x, double y);

int get_substrate_amplitude(char file[100], int h, int k, int l,
double

lamda, double theta, double range, double step, fcomplex
*amplitude);

fcomplex get_amplitude(double theta, fcomplex strfct, double
thickness,

double despacing, double alpha, double lamda);

```

int single_layer_reflection(int h,int k,int l,double lamda,double
material_data[],double theta,
double range,double step,double
thickness,
fcomplex *amplitude);

```

```

double pi=3.14159265358979323;

```

```

/* MAIN PROGRAM

```

```

*****/

```

```

int main (int argc, char *argv[])
{
double intensity[100000], theta_dat[100000];
int i, dat_pts;
if(argv[1]!='\0') printf("\nneed argument: XRDsim
controlfile.dat\n\n");
super_lattice_reflection(argv[1],theta_dat, intensity, &dat_pts);

for (i=0; i<=dat_pts; i++)
    { printf("%f %f\n",theta_dat[i],
intensity[i]);
}
}

```

```

/* FUNCTIONS

```

```

*****/

```

```

double super_lattice_reflection(char *scanfile, double *theta_dat,
double
*intensity,int *dat_pts)
{
/* Variable declarations *****/

double in_cps=340000; /* machine cps without sample */
double running_theta; /* theta used in loops */
double range; /* theta range of simulated scan */
double step; /* theta step size */
static double cd[50]; /* control data: [1]-theta
*/
char material_file[50][100]; /* [2]-range,[3]-step,[4-6]
hkl */
char dummy[50][100]; /* [7] substr,[8] SL
cycles,etc.*/
char filename[100];
static double material_data[11]; /* a,c,u,form
parameters,p.depth*/
static fcomplex amplitude[20][30][100000];
int
repetition,n,file_offset,sl,i,layer,material_file_pointer,layernum
ber=0;
double total_d,d; /* thickness of SL,sample,monolayer */
double K,alpha; /* scattering wavevektor,angle of
planes*/
/* with sample surface */

/* Command Block *****/

```

```

read_indata(scanfile,cd,material_file);

range=cd[2]; /* initializations */
step=cd[3];
file_offset=9;
layernumber=-1;
total_d=0;

for (sl=1;sl<=cd[8];sl++) /* loop through stack of SL's
******/
{
/*
printf("%d %d\n",sl,file_offset);
*/
material_file_pointer += layernumber;
file_offset += 2*(layernumber+1);
layernumber = cd[ file_offset ];

for(repetition=1;repetition<=cd[file_offset+1];repetition++)
{

    for (layer=1;layer<=layernumber;layer++) /* sum all layer and
SL */
    { /* amplitudes */
/*
printf("%d %d %d %d\n",file_offset,sl,repetition,layer);
*/
strcat(strcpy(filename,material_file[material_file_pointer+l
ayer+1]),

```

```

        ".tmp");
/*
printf("%s %s\n",material_file[3],filename);
*/
read_indata(filename,material_data,dummy);
single_layer_reflection(cd[4],cd[5],cd[6],cd[0],material_data,

cd[1],cd[2],cd[3],cd[file_offset+2*layer+1],
amplitude[s1][layer]);

running_theta = cd[1]-0.5*range; i=0;
while (running_theta < cd[1]+0.5*range){
K = 4*pi/cd[0]*sin(running_theta*pi/180);
amplitude[0][0][i] = Cadd(amplitude[0][0][i],

Cmul(amplitude[s1][layer][i],
      Cexp(Complex(0,K*total_d))));
running_theta += step;
      i++;
} /* end while running_theta */

d=get_spacing(cd[4],cd[5],cd[6],material_data[0],material_data[1]);
      n = (int)abs(cd[ file_offset + 2*layer+1]) /d ;
total_d += n*d;

} /* end for layer */

} /* end for repetition */

```

```

} /* end for SL */

/* add substrate amplitude
******/

get_substrate_amplitude(material_file[0], cd[4], cd[5], cd[6],
cd[0],
cd[1], cd[2], cd[3], amplitude[0][1]);

running_theta = cd[1]-0.5*range; i=0; /* sum substrate and
epilayer ***/

while (running_theta < cd[1]+0.5*range)
{
    K = 4*pi/cd[0]*sin(running_theta*pi/180);
    amplitude[0][0][i] = Cadd( amplitude[0][0][i],
        Cmul( Cexp( Complex(0,K*total_d)),
            amplitude[0][1][i] ) );

    running_theta += step; i++;
}

/* data output
******/

running_theta = cd[1]-0.5*range; i=0;
while (running_theta < cd[1]+0.5*range)
{
    theta_dat[i] = running_theta;
    intensity[i] =

```

```

Cabs (Cmul (amplitude[0][0][i], amplitude[0][0][i]))
      /60926*(in_cps/340000);
                                /* normalize cps to maschine intensity
******/
      running_theta += step;
      i++;
}
*dat_pts = i-1;
}

/***** get substrate amplitude
******/

int get_substrate_amplitude(char file[100], int h, int k, int l,
double
lamda, double theta, double range, double step, fcomplex
*amplitude)
{
char dummy[30][100];
double material_data[12];
int i = 0;
double running_theta = theta-0.5*range;
double form1, form2;
fcomplex phase[4];      /* atomic formfactors and phases */
double x;               /* variable for formfactor calc. */
fcomplex strfct; /* structure factor */
double u, a, c, d, alpha;

strcat(file, ".tmp");

```



```

read_indata(file,material_data,dummy);

a = material_data[0];
c = material_data[1];
u = material_data[2];
d = get_spacing(h,k,l,a,c);
alpha = get_alpha(h,k,l,0,0,1,a,c);

/* read_indata(file,material_data,dummy); */

/* Ga-sites atomic phases, the last two N-sites phases for the */
/* atomic formfactor of primitive basis of the hcp lattice */
*/
phase[0] = Cexp(Complex(0,2*pi*( h*1./3 + k*2./3 + l*0.)));
phase[1] = Cexp(Complex(0,2*pi*( h*2./3 + k*1./3 + l*1./2)));
phase[2] = Cexp(Complex(0,2*pi*( h*1./3 + k*2./3 + l*u)));
phase[3] = Cexp(Complex(0,2*pi*( h*2./3 + k*1./3 + l*(1./2+u))));

while (running_theta < theta+0.5*range) /* get atomic
formfactors for */
/* the two basis atoms */
{
    x = sin(running_theta*pi/180)/lamda;
    form1 = material_data[3] + material_data[4]*x +
material_data[5]*x*x +
        material_data[6]*x*x*x;
    form2 = material_data[7] + material_data[8]*x
+material_data[9]*x*x +
        material_data[10]*x*x*x;
    /* get structure factor for primitive hcp basis

```

```

*****/
        strfct=Cadd(RCmul(form1,Cadd(phase[0],phase[1])),
                    RCmul(form2,Cadd(phase[2],phase[3])));

        amplitude[i] = Cmul(strfct,/* substrate
amplitude */*/
Cdiv( Complex(1,0) ,
Csub(Complex(1,0),
Cexp(Complex(-d/(material_data[11]*
sin(running_theta)),
4*pi/lamda*sin(running_theta*pi/180)*d)))));

running_theta += step;
        i++;
}
}

/***** get amplitude for a single layer
*****/

int single_layer_reflection(h,k,l,lamda,material_data,theta,
range,step,thickness,amplitude)
int h,k,l;
double lamda, theta, range, step, thickness;
double material_data[11];
fcomplex *amplitude;
{
int i = 0;
double running_theta = theta-0.5*range;

```

```

double form1,form2;
fcomplex phase[4]; /* atomic formfactors and phases */
double x; /* variable for formfactor calc. */
fcomplex strfct; /* structure factor */
double a = material_data[0];
double c = material_data[1];
double u = material_data[2];
double d = get_spacing(h,k,l,a,c);
double alpha = get_alpha(h,k,l,0,0,1,a,c);

/* Ga site, N site phases for the */
/* atomic formfactors of primitive basis of the hcp lattice */
phase[0] = Cexp(Complex(0,2*pi*( h*1./3 + k*2./3 + l*0.)));
phase[1] = Cexp(Complex(0,2*pi*( h*2./3 + k*1./3 + l*1./2)));
phase[2] = Cexp(Complex(0,2*pi*( h*1./3 + k*2./3 + l*u)));
phase[3] = Cexp(Complex(0,2*pi*( h*2./3 + k*1./3 + l*(1./2+u))));

while (running_theta < theta+0.5*range) /* get atomic
formfactors *****/
{
x = sin(running_theta*pi/180)/lamda;
form1 = material_data[3] + material_data[4]*x +
material_data[5]*x*x +
material_data[6]*x*x*x;
form2 = material_data[7] + material_data[8]*x +
material_data[9]*x*x +
material_data[10]*x*x*x;
/* get structure factor for primitive hcp basis
*****/
strfct=Cadd(RCmul(form1,Cadd(phase[0],phase[1])),

```

```

        RCmul(form2,Cadd(phase[2],phase[3])));
    amplitude[i] = get_amplitude(running_theta,strfct,
        thickness,d,alpha,lamda);
    running_theta += step;
    i++;
}
}

/***** read a line from input data file
*****/

char *GetLine(char *receiver) /* read one line out of file
at fpin */
{ /* copy result in given variable */
    char a,temp[100];
    int c=0;
    temp[c]=fgetc(fpin);
    while ((temp[c]!=EOL)&&(temp[c]!=EOF)) { temp[++c]=fgetc(fpin);
}
    temp[++c]=100;
    strncpy(receiver,temp,16);
}

/***** read data from input data files using GetLine
*****/

int read_indata(char material[100],double *line,char
material_file[30][100])

```

```

    {
int n,i,j=0;
char filename[100] = "indata/";
char receiver[16];
    strcat(filename,material);
    fpin = fopen(filename,"r");
i=0; receiver[0]='\1';
while(receiver[0]!=EOF && receiver[0]!=EOL &&
receiver[0]!=EOS) {
GetLine(receiver);
if (isdigit(receiver[0]) || receiver[0]=='-')
line[i] = atof(receiver);
if (isalpha(receiver[0]))
        { n=((int) index(receiver, ' '))-((int)receiver);
    strncpy(material_file[j],receiver,n);j++; };
i++;
}
fclose(fpin);
}

/***** positive modulus of two double variables
*****/
/* gives distance of x to the next integer multiple of y */

double absmod(double x, double y)
{
double rest;
rest = fabs(x/y) - floor(fabs(x/y));
if(rest>.5) rest = fabs(rest-1);

```

```

return(fabs(rest*y));
};

/***** calculate phase sum for a single layer
        (used by single_layer_reflection)
*****/

fcomplex get_amplitude(theta, strfct, thickness, despacing,
alpha, lamda)
double theta, thickness, despacing, alpha, lamda;
fcomplex strfct;
{
fcomplex phase_sum = {0,0}; /* storage variable */
double K = 4*pi/lamda*sin(theta*pi/180); /* scattering vector
*/
double x = K*despacing; /* geom.sum argument */
int n = (int)abs((thickness/cos(alpha))/despacing); /* #of planes
*/

/* printf("theta %f, strfct %f, thick %f, desp %f, alpha %f, lamda
%f\n",
theta, strfct.r, thickness, despacing, alpha, lamda);
*/
if ( absmod(x,2*pi) < 10e-12){
    phase_sum = Complex(n,0.5*n*(n-1)*x);
};
if (absmod(x,2*pi) > 10e-12 ) {
    phase_sum=Cdiv( Csub(Complex(1,0),Cexp(Complex(0,n*x))),
        Csub(Complex(1,0),Cexp(Complex(0,x))) );
    phase_sum = Cmul(phase_sum, strfct);
}
}

```

```
};  
  
    if (n==0) phase_sum=Complex(0,0);  
  
return(phase_sum);  
}
```

```
/****** END OF FILE
```

```
******/
```

APPENDIX B

SUPERLATTICE ANALYZER

B.1 USAGE DESCRIPTION

Unlike the HRXRD simulation this program does not fancy an easy to use window based interface. For this program command line options have to be specified, and only text output is available. The text below is the content of the Linux system manual page created for the program:

B.1.1 MANUAL PAGE

SLAnalyzer, ver.1.0, July 18 1998, Fritz's Utilities: Print superlattice information from Bragg peak position to standard output.

B.1.2 SYNOPSIS

SLAnalyzer [-i peakfile] [-c In composition estimate] [-S d substrate] [-A d alloy] [-t tetragonal distortion] [-p periods] [-s A shutter time] [-a B shutter time] [-f mulstr—mulrel—zerostr—zerorel] [-v sgrowth—agrowth—SLp—acomp]

B.1.3 DESCRIPTION

SLAnalyzer processes peak positions of an AB superlattice on substrate of material A obtained by an omega/2theta scan, and prints selected information about calculated period, Bragg peak offset, Bragg peak index, superlattice d-spacing, biaxial strain and alloy composition. A best fit line for the superlattice equation is given by a least

squares method. If growth-run shutter times are known the alloy composition in layer B and growth rates of layers A and B for each alloy material are calculated.

The program has been created with a 20 period A=GaN, B=InGaN superlattice with 9% overall InN content in mind. Shutter times were known to be 210 sec. for GaN and 20 sec. for InGaN. The substrate was GaN (therefore command line options -s/-S=substrate and -a/-A=alloy for the superlattice materials). All default settings refer to this structure.

When SLAnalyzer is started any option not specified will use default settings. There is no help message.

B.1.4 OPTIONS

All material and sample data must be specified:

-i peakfile

Peakfile is a three column data file. Column one contains flags "c"=commented out, "s"=substrate or none. Column two holds peak intensities. Column three holds peak positions (angle theta in degrees). Columns are separated by tabs. Default: "period.in"

-c In composition estimate

Give your In composition estimate for the entire superlattice in parts of 1, not in per cent. This parameter is crucial for successful data fitting, since it defines the zeroth order peak position. default: "0.09"

-S d substrate

Substrate plane spacing in growth direction in Angstroms. Same as layer A plane spacing constant. Default: GaN 002, "2.5925"

-A d alloy

Layer B second alloy material plane spacing in growth direction in Angstroms. The first alloy material is assumed to be the layer A material. Default: InN 002, "2.88"

-t tetragonal distortion

Layer A material tetragonal distortion coefficient. Default: GaN, "1.53"

-p periods

Number of periods in the superlattice. Default: "20"

-s A shutter time

Deposition time for layer A within one period in seconds. Default: "210"

-a B shutter time

Deposition time for layer B within one period in seconds. Default: "20"

-f mulstr—mulrel—zerostr—zerorel

If the verbose option `-v` is set to something else than "all" a data fitting method has to be specified. The options are multi peak strained fit, multi peak relaxed fit, zeroth order peak strained fit, zeroth order relaxed fit, respectively. Multi peak fit uses the superlattice equation, zeroth order peak fit uses only the position of the zeroth order superlattice peak as data input. Strained and relaxed refer to the status of the superlattice relative to the substrate. Default: "mulstr"

-v sgrowth—agrowth—SLp—acomp

If `-v` is not specified, all fit methods and all results will be printed to standard output. Within a script it is useful to minimize the output data. For each option one three column line will be put out: The first column holds the position on the wafer (square root of $X^2 + Y^2$ as found in "peakfile"). The second column holds the data point (substrate material growth rate in layer A, second alloy material growth rate in layer B, superlattice period, layer B composition coefficient, respectively). The third column contains the calculated error. If shutter times are unknown, only "SLp" is a meaningful option. Default: not specified

B.1.5 REMARKS

All options may be used in random order. The program produces no help output. The alloy composition guess is most likely to be right, if both the strained and relaxed calculation agree on the zeroth order superlattice peaks (at least for reasonably thin layers as the ones the program was written for).

The SLAnalyzer command appears on OSU MBE Lab Linux Systems.

B.2 SUPERLATTICE ANALYZER CODE

All include files listed are standard numerical recipes library files for linear regression. Small changes have been made in the *fit.c* file to calculate errorbars. Hence the new name *fit_mod1.c*.

```
/*
```

```
SLanalyzer ANSI C-code
```

```
SLAnalyzer processes peak positions of an AB superlattice on
substrate of material A obtained by an omega/2theta scan and
prints
```

```
selected information about calculated period, Bragg peak
offset,
```

```
Bragg peak index, superlattice d-spacing, biaxial strain and
alloy
```

```
composition. A best fit line for the superlattice equation
is given. If
```

```
growth run shutter times are known the alloy composition in
layer B and
```

```
growth rates of layers A and B for each material are put
out.
```

```
The program has been created with a 20 period A=GaN, B=InGaN
superlattice with 9% overall InN content in mind. Shutter
times
```

```
were known to be 210 sec. for GaN and 20 sec. for InGaN. The
substrate was GaN (therefore command line options -s/-
```

```
S=substrate
```

```
and -a/-A=alloy for the superlattice materials). All default
```

settings refer to this structure.

When SLAnalyzer is started any option not specified will use default settings.

There is no help message.

original Fortran / MS Excel spreadsheet version
by R. J. Hauenstein, 1991/1998

Functions LoadLine() and GetPeaks() by Mark L. O'Steen

Fritz Fedler

July 18, 1998

*/

```
#define npksmx 50
```

```
#define lambda 1.5405945 /* Cu-Kalpal radiation */
```

```
#define twothstep 0.005
```

```
#define pi 3.141592654
```

```
#define EOL '\n'
```

```
#define EOS '\0'
```

```
#include <stdlib.h>
```

```
#include <stdio.h>
```

```
#include <math.h>
```

```
#include <string.h>
```

```
#include <unistd.h>
```

```
#include "include/nrerror.h"
```

```

#include "include/gammln.h"
#include "include/gser.h"
#include "include/gcf.h"
#include "include/gammq.h"
#include "include/fit_mod1.h"

FILE *fppeaks; /* file pointer for peak and output files. */
FILE *fpout;

struct peak_info /* all peak related information */
{
    char IdString[100];
    int npks;
    double inten[npksmx];
    double twothexp[npksmx], twothth[npksmx];
    double BraggIndex[npksmx], SLordstr[npksmx],
SLordrel[npksmx];
    double fity[npksmx], dfity[npksmx];
    double subtwothexp, subtwothth;
};

struct SL_data /* superlattice data */
{
    double SLper, dSLper, ccoeff, ZeroBragg;
    double SLsp[4], dSLsp[4]; /* 0: multi peak fit
strained */
    double BiStr[4], dBiStr[4]; /* 1: multi peak fit relaxed
*/
    double InC[4], dInC[4]; /* 2: 0th peak fit strained */
    double BraggIndexOffset; /* 3: 0th peak fit

```

```

relaxed */
    double slopestr, sloperel, yintstr, yintrel;
};

struct pSL_data /* processed SL data */
{
    double InCInLayer, dInCInLayer, InGaNthick, dInGaNthick;
    double GaNthick, dGaNthick, GaNrate, dGaNrate;
    double InNrate, dInNrate, GaNtot, dGaNtot, InNtot, dInNtot;
};

struct cmd_line_options /* contains variables given at startup */
{
    double nperiods, InGaNshutter, GaNshutter, dGaN, dInN,
dtetr, InCEst;
    double latt_mismatch;
    char peakfile[50];
    int fitflag, printflag;
};

/***** M A I N *****/
*****/

int main(int argc, char *argv[])
{
    int i;
    double tmp;
    char pfile[30], outfile[30];
    struct peak_info PK;
    struct SL_data SL;

```

```

struct pSL_data pSL;
struct cmd_line_options CO;
int nmlPerstr, nmlPerrel;
/* number of monolayers per period strained, relaxed
*/

    if(!get_options(argc,argv,&CO)){ exit(-1);};
    CO.latt_mismatch = fabs((CO.dInN-CO.dGaN)/CO.dGaN);
/* LOAD PEAKS FROM FILE */
    GetPeaks(CO.peakfile, &PK, CO.printflag);
    double_twotheta_get_offset(&PK,&CO);
    linear_SL_peak_fit(&SL,&PK);
    find_peak_order_str(&PK);
    get_SL_period(&SL,&PK);
/* ESTIMATE # OF MONOLAYERS PER SL PERIOD, STRAINED&RELAXED */
    nmlPerstr=(int)rint( SL.SLper/(CO.dGaN*(1+CO.InCEst*
(CO.dInN/CO.dGaN-1)*CO.dtetr)) );
    nmlPerrel=(int)rint( SL.SLper/(CO.dGaN*(1+CO.InCEst*
(CO.dInN/CO.dGaN-1))) );
/* DO VARIOUS FITS */
    find_from_zeroth_order(nmlPerstr,&SL,&PK,&CO,0);
    find_from_zeroth_order(nmlPerrel,&SL,&PK,&CO,1);
    find_from_multi_order_fit(nmlPerstr,&SL,&PK,&CO,0);
    find_from_multi_order_fit(nmlPerrel,&SL,&PK,&CO,1);

    process_SL_data(&pSL, &SL, &CO, 0);

/* PRINT RESULTS */
    if(CO.printflag==4)
    {

```

```

    print_results(&SL, &PK, nmlPerstr, nmlPerrel);
    print_results_pSL(&pSL);
}

else{

print_single_line(&pSL, &SL, &PK.IdString, CO.printflag, CO.fitflag);
    };
} /* end main */

/***** E N D   M A I N *****/

int get_options(int argc, char *argv[], struct cmd_line_options
*CO)
{
int a=0, end=0, OK=1;
    opterr=0;
/* SET DEFAULTS */
(*CO).nperiods = 20;
(*CO).InGaNshutter = 20;
(*CO).GaNshutter = 210;
(*CO).dGaN = 5.189/2;
(*CO).dInN = 5.760/2;
(*CO).dtetr = 1.53;
(*CO).InCEst = 0.09;
sprintf((*CO).peakfile, "period.in");
(*CO).fitflag = 0;
(*CO).printflag = 4;
/* CATCH CMD LINE OPTIONS */
    while(!end)

```



```

    {
        a=getopt(argc,argv,"p:a:s:S:A:t:c:i:o:f:v:");
        switch(a)
            {
                case 'p':
if(isdigit(optarg[0])){ (*CO).nperiods = atof(optarg);
}
else { printf("\n -p    number of periods    --
%s not a number!\n",optarg); exit(-1);};
                break;
                case 'a':
if(isdigit(optarg[0])){ (*CO).InGaNshutter = atof(optarg);
}
else { printf("\n -a    alloy shutter time (sec)    --
    %s not a number!\n",optarg); exit(-1);};
                break;
                case 's':
if(isdigit(optarg[0])){ (*CO).GaNshutter = atof(optarg);
}
else { printf("\n -s    substrate shutter time (sec)    --
    %s not a number!\n",optarg); exit(-1);};
                break;
                case 'S':
if(isdigit(optarg[0])){ (*CO).dGaN = atof(optarg);
}
else { printf("\n -S    Substrate d-spacing (Angstr)    --
    %s not a number!\n"); exit(-1);};
                break;
                case 'A':
if(isdigit(optarg[0])){ (*CO).dInN = atof(optarg);

```

```

}
else { printf("\n  -A  Alloy material d-spacing (Angstr)
--
  %s not a number!\n",optarg); exit(-1);};
      break;
      case 't':
if(isdigit(optarg[0])){ (*CO).dtetr = atof(optarg);
}
else { printf("\n  -t  tetragonal distortion (C13/C33)  --
  %s not a number!\n",optarg); exit(-1);};
      break;
      case 'c':
if(isdigit(optarg[0])){ (*CO).InCEst = atof(optarg);
}
else { printf("\n  -c  In composition estimate (parts of 1)
--
  %s  not a number!\n",optarg); exit(-1);};
      break;
      case 'i':
sprintf((*CO).peakfile,"%s",optarg);
      break;
      case 'f':
if(!strncmp(optarg,"mulstr",5)){(*CO).fitflag=0;}
else if(!strncmp(optarg,"mulrel",5)){(*CO).fitflag=1;}
else if(!strncmp(optarg,"zerostr",5)){(*CO).fitflag=2;}
else if(!strncmp(optarg,"zerorel",5)){(*CO).fitflag=3;}
else {printf("\n  -f  fitflag, %s not a valid option
(mulstr,
mulrel,zerostr,zerorel)\n",optarg);
      exit(-1);};

```

```

        break;
        case 'v':
if(!strncmp(optarg, "sgrowth", 3)) {(*CO).printflag=0;}
else if(!strncmp(optarg, "agrowth", 3)) {(*CO).printflag=1;}
else if(!strncmp(optarg, "SLp", 3)) {(*CO).printflag=2;}
else if(!strncmp(optarg, "acomp", 3)) {(*CO).printflag=3;}
else {printf("\n -v verbose flag, %s not a valid option
(sgrowth,
agrowth, SLp, acomp)\n", optarg);
        exit(-1);};
        break;
        case -1:
end=1;
        break;
        case '?':
OK=0;
printf("option not understood: %c\n", optopt);
        break;
        };
};
};

int GetPeaks(char *pfile, struct peak_info *PK, int printflag)
{

    int n, j, s, sflag, isub;
    int i=-1;
    int EndOfFile=0;
    char *spot;

```

```

char flg[npksmx],temp[100];
double max,inten[npksmx],twotheta[npksmx];
fppeaks=fopen(pfile,"r");

/* First line of peak-file is assumed to be Id info */
EndOfFile=LoadLine(fppeaks,temp,printf);
strcpy((*PK).IdString,temp);

while(!EndOfFile)
{
    EndOfFile=LoadLine(fppeaks,temp,printf);
    ++i;
    flg[i]=temp[0];
    inten[i]=strtod(temp+1,&spot);
    twotheta[i]=strtod(spot,&spot);
}
close((int)fppeaks);

/* find substate */
max=-1.0;
isub=-1;
sflag=-1;
for(j=0;j<=i-1;++j)
{
    if ((flg[j]!='c')||(flg[j]!='#')||(flg[j]!=';'))
    {
        if (flg[j]=='s') { sflag=j; };
        if (inten[j]>max)
        {
            max=inten[j];
        }
    }
}

```

```

        isub=j;
    }
}
s=sflag;
if (s==-1) { s=isub; }
flg[s]='s';
if(printflag==4){printf("\nsubstrate=%f\n\n",twotheta[s]);};

/* pack data into "peaks" structure */
(*PK).subtwothexp=twotheta[s];
n=0;
for(j=0;j<=i-1;++j)
{
    if
((flg[j]!='c')&&(flg[j]!='#')&&(flg[j]!=';')&&(flg[j]!='s'))
    {
        ++n;
        (*PK).inten[n-1]=inten[j];
        (*PK).twothexp[n-1]=twotheta[j];
    }
}
(*PK).npks=n;
}

int LoadLine(FILE *fp, char *receiver, int printflag)
{
    char a,temp[100];
    int c=-1;
    int EndOfFile=0;

```

```

int EndOfLine=0;
while((!EndOfFile)&&(!EndOfLine))
{
    temp[++c]=fgetc(fp);
    if (temp[c]==EOL) { EndOfLine=1; }
    if (temp[c]==EOF) { EndOfFile=1; }
}
temp[c]=EOS;
strcpy(receiver, temp);
if (printflag==4) {printf("\n%s", temp);};
return(EndOfFile);
}

```

```

/* double the input angles to gain conformity with old formulas
***/
/* compute the offset between exp. and theo. value for thwotheta
substrate ***/
int double_twotheta_get_offset(struct peak_info *PK,
struct cmd_line_options *CO)
{
int i;
double offset;
(*PK).subtwothexp = 2*(*PK).subtwothexp;
(*PK).subtwothth = 2*asin(lambda/(2*(*CO).dGaN))*180/pi;
offset = (*PK).subtwothexp - (*PK).subtwothth;
for(i=0;i<=(*PK).npks-1;i++){
(*PK).twothexp[i] = 2*(*PK).twothexp[i];
(*PK).twothth[i] = (*PK).twothexp[i] - offset;
}
}

```

```

)

/* compute fity for linear fit of SL Bragg peaks ****/

int linear_SL_peak_fit(struct SL_data *SL, struct peak_info *PK)
{
double err2th, theta;
int i;
    if(.01<twothstep/5){
err2th = 0.5*pi*(twothstep/5)/180; } /* est error in peak
positions */
    else {err2th = 0.5*pi*.01/180; } ;
    for(i=0;i<=(*PK).npks-1;i++){
theta=0.5*(*PK).twothth[i]*pi/180;
(*PK).fity[i]=2*sin(theta)/lambda; /*
ordinate for fit */
(*PK).dfity[i]=err2th*cos(theta)/lambda; /* error bars
for each point */
    }
}

/* assign integer offsets (Bragg index) to all unflagged peaks
******/

int find_peak_order_str(struct peak_info *PK)
{
double spcavg, spcmin, spc, mwt, dy;
double n[(*PK).npks];

```

```

int i;
    spcavg=((*PK).fity[(*PK).npks-1]-(*PK).fity[0])/((*PK).npks-1);
/* find avg peak spacing measured in SL orders*/
    spcmin=spcavg;                                /* initialize */
    for(i=0;i<=(*PK).npks-2;i++){
        if(spcmin > ((*PK).fity[i+1]-(*PK).fity[i]))
{ spcmin = ((*PK).fity[i+1]-(*PK).fity[i]);};
    }; /* now have min spacing betw. two peaks measured in Bragg
orders */

    if(spcavg/spcmin < 2){spc=spcmin;}
    else{spc=spcavg;
        printf("\nWARNING: Bragg peak integer offsets are
questionable.\n");
    };
n[0]=0;
(*PK).BraggIndex[0]=0;
    for(i=0;i<=(*PK).npks-2;i++){
        dy=(*PK).fity[i+1]-(*PK).fity[i];
        n[i+1]=n[i] + (int)rint(dy/spc);
        (*PK).BraggIndex[i+1]=n[i+1];
    };
}

/* Do a linear fit: get SL period from slope */

int get_SL_period(struct SL_data *SL, struct peak_info *PK)
{
double

```



```

yint=0.0,slope=0.0,sigint=0.0,sigslo=0.0,chi2=0.0,q=0.0,ccoef=0.0;
double sig=0.0,xint=0.0;
int mwt=0,i,n_zero=0;
(*SL).SLper = 0.0;
(*SL).dSLper = 0.0;

fit((*PK).BraggIndex, (*PK).fity, (*PK).npks, (*PK).dfity, mwt, &yint, &
slope,
&sigint, &sigslo, &chi2, &q, &(*SL).ccoef);
    /*compute unweighted linear least-squares fit*/

    (*SL).SLper=1/slope;                /* superlattice
period*/
    (*SL).dSLper=sigslo*(*SL).SLper/slope;    /* std dev
of SL period*/
    xint = -yint/slope;                /* real x intercept */
    n_zero=(int)rint(xint);            /* offset of Bragg
indices */
    (*SL).BraggIndexOffset=xint-n_zero;
    for(i=0;i<=(*PK).npks-1;i++){
        (*PK).BraggIndex[i] = (*PK).BraggIndex[i] - n_zero; /*
compute Bragg order*/
    };
};

int find_from_zeroth_order(int nml, struct SL_data *SL, struct
peak_info *PK,
    struct cmd_line_options *CO, int relflag)

```

```

{
int i=0, izero=0;
double err2th;
    for(i=0;i<=(*PK).npks-1;i++){ /* search for zeroth
order SL peak */
if( nml == (int)rint( (*PK).BraggIndex[i] ) ) { izero=i; };
    };

    if(!izero){
        if(!relflag){
            printf("\nWARNING: Coherently strained case zeroth order
SL peak not found!\nnml= %d\n",nml);
        }
        else if(relflag){
            printf("\nWARNING: Fully relaxed case zeroth order
SL peak not found!\nnml= %d\n",nml);
        }
    };

/* calculate lattice const. from 0th SL peak */
    (*SL).SLsp[2+relflag] = 1/(*PK).fity[izero];
    if(.01<twothstep/5){
err2th = 0.5*pi*(twothstep/5)/180; } /* est error in peak
positions */
    else {err2th = 0.5*pi*.01/180; } ;
    (*SL).dSLsp[2+relflag] = ((*SL).SLsp[2+relflag]/2)*
err2th/tan(0.5*pi*( *PK).twothth[izero]/180);

/* avg bilayer strain from 0th SL peak */
    (*SL).BiStr[2+relflag] = 100*((*SL).SLsp[2+relflag]/(*CO).dGaN-
```

```

1);
    (*SL).dBiStr[2+reldata] = 100*sqrt(2.)*( (*SL).dSLsp[2+reldata]
/
(*SL).SLsp[2+reldata]);

/* avg In composition from 0th SL peak */
    if(!reldata){
        (*SL).InC[2+reldata] = (*SL).BiStr[2+reldata] / (
(*CO).dInN/(*CO).dGaN-
1)*(*CO).dtetr );
        (*SL).dInC[2+reldata]=(*SL).InC[2+reldata]*sqrt(
(*SL).dBiStr[2+reldata]/(*SL).BiStr[2+reldata]*( (*SL).dBiStr[2+reldata]
lag)/
(*SL).BiStr[2+reldata]
+0.01*0.01/(*CO).dtetr/(*CO).dtetr);
    };
    if(reldata){
        (*SL).InC[2+reldata] = (*SL).BiStr[2+reldata] /
(*CO).dInN/(*CO).dGaN-1);

(*SL).dInC[2+reldata]=(*SL).InC[2+reldata]*( (*SL).dBiStr[2+reldata]
/
(*SL).BiStr[2+reldata]);
    };
};

int find_from_multi_order_fit(int nml,struct SL_data *SL, struct
peak_info *PK,

```

```

    struct cmd_line_options *CO, int relflag)
{
double BraggIndex002[(*PK).npks];
double yint=0.0,slope=0.0,sigint=0.0,sigslo=0.0,
chi2=0.0,q=0.0,ccoef=0.0,sig=0.0;
int mwt=0,i=0;
    for(i=0;i<=(*PK).npks;i++){
        BraggIndex002[i] = (*PK).BraggIndex[i] - nml;
    };

fit(BraggIndex002,(*PK).fity,(*PK).npks,(*PK).dfity,mwt,&yint,&slope,
&sigint,&sigslo,&chi2,&q,&ccoef);
        /*compute unweighted linear least-squares
fit*/

/* calculate lattice const. from multi order SL peaks */
(*SL).SLsp[relflag] = 1/yint;
(*SL).dSLsp[relflag] = sigint*(*SL).SLsp[relflag]/yint;

/* avg bilayer strain from multi order SL peaks */
(*SL).BiStr[relflag] = 100*((*SL).SLsp[relflag]/(*CO).dGaN-1);
(*SL).dBiStr[relflag] = 100*sqrt(2.)*(( *SL).dSLsp[relflag]/
(*SL).SLsp[relflag]);

/* avg In composition from multi order SL peaks */
if(!relflag){
    (*SL).InC[relflag]=(*SL).BiStr[relflag] / (
(( *CO).dInN/( *CO).dGaN-1)
*( *CO).dtetr );

```

```

        (*SL).dInC[reldata] = (*SL).InC[reldata] * sqrt (
(*SL).dBiStr[reldata] / (*SL).BiStr[reldata] * (*SL).dBiStr[reldata] /
(*SL).BiStr[reldata]
        + 0.01 * 0.01 / (*CO).dtetr / (*CO).dtetr);
        (*SL).slopestr = slope; /* save fit parameters */
        (*SL).yintstr = yint;
    };
    if(reldata){
        (*SL).InC[reldata] = (*SL).BiStr[reldata] /
(((*CO).dInN / (*CO).dGaN - 1);
(*SL).dInC[reldata] = (*SL).InC[reldata] * (*SL).dBiStr[reldata] /
(*SL).BiStr[reldata];
        (*SL).sloperel = slope; /* save fit parameters */
        (*SL).yintrel = yint;
    };
};

int print_results(struct SL_data *SL, struct peak_info *PK,
    int nmlstr, int nmlrel)
{
int i=0;
    printf("\n%s\n", (*PK).IdString);
    printf("\nSLPeriod: %f +/- %f\n", (*SL).SLper, (*SL).dSLper);
    printf("Correlation coeff.: %f\n", (*SL).ccoeff);
    printf("Extrapolated zeroth order Bragg peak offset: %f\n",
(*SL).BraggIndexOffset);

```

```

printf("\nZEROTH ORDER SL PEAK FIT, COHERENTLY STRAINED:\n");
printf("SL d-spacing      = %f +/-
%f\n", (*SL).SLsp[2], (*SL).dSLsp[2] );
printf("SL bilinear Strain= %f +/-
%f\n", (*SL).BiStr[2], (*SL).dBiStr[2] );
printf("In composition    = %f +/-
%f\n", (*SL).InC[2], (*SL).dInC[2] );

printf("\nZEROTH ORDER SL PEAK FIT, INDIVIDUALLY RELAXED:\n");
printf("SL d-spacing      = %f +/-
%f\n", (*SL).SLsp[3], (*SL).dSLsp[3] );
printf("SL bilinear Strain= %f +/-
%f\n", (*SL).BiStr[3], (*SL).dBiStr[3] );
printf("In composition    = %f +/-
%f\n", (*SL).InC[3], (*SL).dInC[3] );

printf("\nMULTI SL PEAK FIT, COHERENTLY STRAINED:\n");
printf("SL d-spacing      = %f +/-
%f\n", (*SL).SLsp[0], (*SL).dSLsp[0] );
printf("SL bilinear Strain= %f +/-
%f\n", (*SL).BiStr[0], (*SL).dBiStr[0] );
printf("In composition    = %f +/-
%f\n", (*SL).InC[0], (*SL).dInC[0] );

printf("\nMULTI SL PEAK FIT, INDIVIDUALLY RELAXED:\n");
printf("SL d-spacing      = %f +/-
%f\n", (*SL).SLsp[1], (*SL).dSLsp[1] );
printf("SL bilinear Strain= %f +/-
%f\n", (*SL).BiStr[1], (*SL).dBiStr[1] );
printf("In composition    = %f +/-

```

```

%f\n", (*SL).InC[1], (*SL).dInC[1] );

    printf("\n Bragg index      SL order      SL order
2*sin(theta)/lambda  theta \n");
    for(i=0;i<=(*PK).npks-1;i++){
printf("\n %f      %f      %f      %f      %f ",
(*PK).BraggIndex[i],
(*PK).BraggIndex[i]-nmlstr, (*PK).BraggIndex[i]-nmlrel,
(*PK).fity[i], (*PK).twothexp[i]/2);
    };

    printf("\n\nBest fit line (cohenrently strained):\n");
    printf("y = %f x + %f\n", (*SL).slopestr, (*SL).yintstr);
    printf("\nBest fit line (fully relaxed):\n");
    printf("y = %f x + %f\n", (*SL).sloperel, (*SL).yintrel);

    printf("\n\n");
};

int process_SL_data(struct pSL_data *pSL, struct SL_data *SL,
    struct cmd_line_options *CO, int relflag)
/* relflag=0,1,2,3 use according In composition, see head of file
*/
{
double a,b;
(*pSL).InCInLayer=(*SL).InC[relflag]/100*((*CO).GaNshutter+
(*CO).InGaNshutter)/((*CO).InGaNshutter+(
(*SL).InC[relflag]/100*( (*CO).GaNshutter ));
a = (((*SL).InC[relflag]/100+(*SL).dInC[relflag]/100)*

```

```

(( *CO ).GaNshutter+(*CO).InGaNshutter)/(( *CO ).InGaNshutter
+(( *SL ).InC[reldata]/100+(*SL).dInC[reldata]/100)*
(*CO).GaNshutter));
b =((( *SL ).InC[reldata]/100-
(*SL).dInC[reldata]/100)*(( *CO ).GaNshutter
+(*CO).InGaNshutter)/(( *CO ).InGaNshutter+(( *SL ).InC[reldata]
/
100-(*SL).dInC[reldata]/100)*(*CO).GaNshutter));
(*pSL).dInCInLayer = (a-b)/2;
(*pSL).InGaNthick=( *SL ).SLper*( *SL ).InC[reldata]/
100/( *pSL ).InCInLayer *(1+(*CO).dtetr*( *CO ).latt_mismatch
*( *pSL ).InCInLayer-(*SL).InC[reldata]/100));
(*pSL).dInGaNthick=sqrt( (*SL).dSLper/( *SL ).SLper*( *SL ).dSLper/
(*SL).SLper +(*SL).dInC[reldata]/(*SL).InC[reldata]
*( *SL ).dInC[reldata]/(*SL).InC[reldata]+(*pSL).dInCInLayer/
(*pSL).InCInLayer*( *pSL ).dInCInLayer/( *pSL ).InCInLayer ) *
(*pSL).InGaNthick;
(*pSL).GaNthick=( *SL ).SLper-(*pSL).InGaNthick;
(*pSL).dGaNthick=sqrt( (*pSL).dInGaNthick*( *pSL ).dInGaNthick +
(*SL).dSLper*( *SL ).dSLper );
(*pSL).GaNrate=( *pSL ).GaNthick/( *CO ).GaNshutter*3600/10000;
(*pSL).dGaNrate=( *pSL ).GaNrate*( *pSL ).dGaNthick/( *pSL ).GaNthick;
(*pSL).InNrate=( ( *pSL ).InGaNthick/(
1+(*CO).dtetr*( *pSL ).InCInLayer*( *CO ).latt_mismatch)/
(*CO).InGaNshutter-( *pSL ).GaNrate*10000/3600 )*
(1+(*CO).latt_mismatch)*(1+(*CO).latt_mismatch)*(1+
(*CO).latt_mismatch))*3600/10000;
(*pSL).dInNrate=( sqrt( (*pSL).dInGaNthick*( *pSL ).dInGaNthick +
(*pSL).dGaNrate*10000/3600*( *pSL ).dGaNrate*10000/3600 )
/ (*CO).InGaNshutter )*3600/10000;

```



```

(*pSL).GaNtot=(*pSL).GaNrate*10000/3600*((*CO).GaNshutter+
(*CO).InGaNshutter)*(*CO).nperiods;
(*pSL).dGaNtot=(*pSL).dGaNrate/(*pSL).GaNrate*(*pSL).GaNtot;
(*pSL).InNtot=(*pSL).InNrate*10000/3600*((*CO).GaNshutter+
(*CO).InGaNshutter)*(*CO).nperiods;
(*pSL).dInNtot=(*pSL).dInNrate/(*pSL).InNrate*(*pSL).InNtot; };

```

```

int print_results_pSL(struct pSL_data *pSL)
{
printf("InGaN Layer % InN      : %f +/- %f\n"
, (*pSL).InCInLayer, (*pSL).dInCInLayer);
printf("GaN Layer thickness  : %f +/- %f Angstroms\n"
, (*pSL).GaNthick, (*pSL).dGaNthick);
printf("InGaN Layer thickness: %f +/- %f Angstroms\n"
, (*pSL).InGaNthick, (*pSL).dInGaNthick);
printf("GaN deposit rate      : %f +/- %f micr/hr\n"
, (*pSL).GaNrate, (*pSL).dGaNrate);
printf("InN deposit rate      : %f +/- %f micr/hr\n"
, (*pSL).InNrate, (*pSL).dInNrate);
printf("Total GaN deposited   : %f +/- %f\n"
, (*pSL).GaNtot, (*pSL).dGaNtot);
printf("Total InN deposited   : %f +/- %f\n"
, (*pSL).InNtot, (*pSL).dInNtot);
};

int print_single_line(struct pSL_data *pSL, struct SL_data *SL,
char *idstr, int printflag, int fitflag)
{
double pos;

```

```
char c;
/* parse position on wafer */
/* the last entry in IDString has to be Y='number' */
/* X=Y is assumed */
    sprintf(&c, "Y");
    pos = sqrt(2)*atof(rindex(idstr,c)+2);
    if(!printflag)
    (
printf("%f\t%f\t%f\n", pos, (*pSL).GaNrate, (*pSL).dGaNrate););
        if(printflag==1)

printf("%f\t%f\t%f\n", pos, (*pSL).InNrate, (*pSL).dInNrate););
            if(printflag==2)
                {printf("%f\t%f\t%f\n", pos, (*SL).SLper, (*SL).dSLper);};
            if(printflag==3)

{printf("%f\t%f\t%f\n", pos, (*SL).InC[fitflag], (*SL).dInC[fitflag])
;};
};
```

APPENDIX C

XRD SAMPLE CHARACTERIZATION PROCEDURE

C.1 INTRODUCTION

By utilizing X-ray diffraction it is possible to obtain information about the quality of the crystal structure of a given sample. Scans performed include ω -scans, $\omega/2\theta$ -scans, reciprocal map scans, tilt and lattice parameter measurements and superlattice analysis. The procedures described here will refer to GaN on sapphire and structural related samples. It is assumed that the sample surface coincides with the crystallographic [001] or c-direction. What you need to characterize a sample:

1. Basic knowledge about hexagonal crystal structure in real and reciprocal space (Bragg scattering, Ewald construction etc.).
2. Philips XRD system with wafer stage (incl. monochromator, slit optics, triple axis optics).
3. PC-MRD software.
4. Water cooler for system power supply.
5. Clean environment with rubber gloves, tweezers.
6. Logbook, handbooks that come with the system.
7. A key to room 542 PS II and a sample.

If all of the above is available you are ready to do X-ray diffraction sample characterization.

C.2 PREPARATION

Safety note: NEVER HAVE PARTS OF YOUR BODY IN THE WAY OF THE X-RAY BEAM - THIS MAY CAUSE CANCER! This may happen when the door switches are overridden by the safety-off key. Take EXTREME CARE if disabling the safety circuit!

C.2.1 START OF THE PHILIPS MRD SYSTEM

The following checklist represents my personal procedure. Variations are allowed, as long as they don't hurt the system.

1. Put on the radiation counting tag (do it now, otherwise you'll forget).
2. Make sure the wafer stage can turn freely without hitting any obstacles.
3. Switch on system electronics (initializes wafer stage - takes a couple of minutes).
4. Grab the power supply key from the top of the system (left corner), put the key into the power supply and turn to the right (don't hit the start button yet - it won't work without cooling).
5. Make sure both the voltmeter and the ammeter show ZERO!
6. Flip the switch on the water cooler to turn it on.
7. SLOWLY increase the voltage to 10kV (you will hear a click - a relay enabling current flow).
8. SLOWLY increase the current to 10mA (use lower dial).
9. While the power supply warms up make your entry in the logbook (use 20kV, 35mA for a reasonable signal without overpowering the X-ray tube).

10. Bring up the PC-MRD software on the PC (NOTE: the program changing the optics does not run under Linux DOS emulation - if you want to change optics reboot).
11. SLOWLY increase voltage and current on the power supply to their final settings (20kV, 35mA).
12. The wafer stage initialization should leave the wafer stage without tilt, horizontal x-axis and wafer holder in the center of the disc. Insert the slit you want to use during measurements into the detector.

Now the system should be operative. If errors occur, note them in the logbook. While taking scans frequently check the water cooler by making sure that once in a while the light on its front face labeled cooling is on. The water cables connected to its backside should be cool to the touch.

C.2.2 SHUT DOWN THE PHILIPS MRD SYSTEM

In order to shut down the system you essentially will have to perform the start up tasks in reverse order:

1. Close the X-ray tube shutter.
2. SLOWLY turn down the voltage and current settings on the power supply to an intermediate value (e.g. 10kV, 20mA).
3. Within the PC-MRD program under manual scans reset all angles to zero and move the wafer stage to that position.
4. SLOWLY turn down the current dial to zero; then SLOWLY turn down the voltage to zero.
5. Hit the OFF button on the power supply.
6. Switch off system electronics.
7. Turn off the water cooler.

8. Turn the power supply key to the left and put it back on top of the system.
9. Close all doors (dust protection).
10. Remove your radiation counter tag (don't take it home!).
11. Make sure the PC is in Linux mode for remote data processing.

The XRD system now is completely shut down.

C.2.3 SAMPLE MOUNTING

Samples are assumed clean until proved otherwise. Always use clean tweezers (bathed first in Aceton, then Methanol and finally distilled water) and rubber gloves while handling samples. Be sure you know 'which side is up' before mounting.

Wafers are easily put directly on the wafer stage: adjust the three movable clamps to center the wafer with the 'flat' up.

Smaller samples require a pre-mounting on a metal disc the size of a usual wafer. You will have to put the sample with double sided sticky tape on the disc. Touch the tape several times with a rubber glove before putting a sample on it - it makes removing the piece much easier! You can mount several pieces on one disc. Be sure to label them with a pencil on the metal disc! When mounting several pieces on the same metal disc do it in a way which leaves the X-ray beam unobstructed by the holding clamps on the wafer stage (see beam adjustment!).

If taking very long scans consider a relaxation of the sticky tape mounting due to gravity. This will influence triple axis scans. Let the sample sit on the mounting for a couple of hours before starting the scan. Big samples mounted this way may fall down after some time!

When removing a samples from the wafer stage grab the wafer at its border and slide it to one side. Take it with your second hand (gloves!). To remove pieces from a metal disc use tweezers. Push them sideways and all the time cup the disc with your hand: the sample might suddenly jump away!

Note the names of samples scanned in the logbook.

C.3 SCANNING

C.3.1 BEAM ADJUSTMENT

To obtain accurate results the beam has to be steered across the sample so that the sample cuts the beam in half at all-angles-zero setting. The following procedure is NOT ADVISED by Philips because of safety issues. However, it speeds things up considerably because you do not have to open and close the housing doors all the time and repeatedly open the shutter.

NEVER HAVE PARTS OF YOUR BODY IN THE WAY OF THE X-RAY BEAM
- THIS MAY CAUSE CANCER!

Proceed as follows:

1. Insert a 5mm slit into the detector to limit the total intensity collected.
2. Select (000) as your scan plane in the PC-MRD program. All angles will show zero. Move the stage with hitting the FI key.
3. Position the mounted wafer in x-y-directions to the spot you want to scan (Hint: a ruler to aim the sample between monochromator and detector (x) and the vertical given by the center of the micro-screw(y)).
4. When positioned correctly, pick up the second set of keys and disable the safety circuit.
5. Open shutter 3 of the X-ray tube without timelimit (set dial on infinity symbol).
6. A count rate of ≤ 320.000 cps will appear in the top left corner of the computer monitor. Find the maximum count rate with moving the sample 'backwards' using the micro screw. Then move the sample back into the beam until the program shows half the maximum count rate.

7. If you have a small sample on a metal disc, move the stage in x and y directions and see if the count rate becomes smaller. If so repeat the previous step.

Your sample now is properly adjusted for the first scan.

C.3.2 FINDING THE PEAK

Let's assume you know what peak you want to look at (relative intensity of different plane reflections help to decide which ones are visible and which are not). Choose the sample material and the set of planes (e.g. GaN, 002). The software needs to know your sample's orientation: Be sure the P-vector in the PC-MRD software for your material coincides with the sample surface normal. The S-vector has to be perpendicular - in the sample plane (Example: the sample surface of GaN grown in c-direction is parallel to 002 planes, hence the according vectors are P: 001 and S: 011). These vectors may be changed in SYSTEM PREPARATION/UNIT CELL PARAMETERS within the PC-MRD software. Check reachable sets of planes in RECIPROCAL SPACE MAP. Now that the software is configured you can make your first scan:

1. If the wafer stage is in triple axis mode change to slit optics.
2. Remove any slit from the detector to allow wide θ -angle perception.
3. Choose ω as your scan angle. Select a wide scan range (3-5deg) with a minimum scan time.
4. Hit F2 to take an ω scan.

If you chose a set of planes parallel to your sample surface a peak should show up. Increase the scan range and the scan time to have a better signal to noise ratio if it does not.

For off axis scans (off the sample z-axis) the first scan will or will not show a peak. It is necessary to consider the symmetry of the lattice. For the six fold degeneracy of hexagonal structures a signal is to be found at 60 deg steps in ϕ (angle) around sample

z-axis). Depending on your estimated signal sharpness make the above ω scan with different ϕ angles (5-10 deg steps) over a range of 60 deg. If your signal is not too weak the sought for peak should show up.

C.3.3 OPTIMIZING THE SIGNAL

C.3.3.1 BASIC OPTIMIZATION. NOTE: Do at first use slit or open optics for the following. It is easy to miss your peak with the higher resolution triple-axis optics. Once optimized for the lower resolution optics, repeat the steps for the higher resolution triple-axis optics for optimal results.

All one-dimensional measurements (ω , $\omega/2\theta$ scans etc.) require your having the detector 'sit' on the highest intensity spot of the reciprocal lattice feature.

1. Take alternating ω and $\omega/2\theta$ scans to find the highest intensity spot. Save temporary files and look at both scans in GRAPHICS/SINGLE SCANS. Have SHOW ANGLES IN DEGREES selected. If the peaks of both scans coincide, you have the highest intensity spot.
2. Take a ψ scan to adjust for mounting tilt and plane to sample surface tilt. Set ψ to the value yielding the highest intensity (this does not affect your full width half maximum (FWHM) a great deal, but it may affect the signal to noise ratio a lot).
3. Repeat the first step.
4. Take a ϕ scan and select the angle yielding the highest intensity (this may even make a difference for symmetric scans if the sample has low quality - for high quality sample symmetric scans no change in intensity should be observed).
5. Repeat the first step.

Your sample is now ready for taking FWHM data or reciprocal space maps if the absolute position of the peak is not important to you (standard lab procedure for ω and $\omega/2\theta$ as well as fast rec.space map scans).

C.3.3.2 OPTIMIZE FOR ABSOLUTE ANGLES. NOTE: Do at first use slit or open optics for the following. It is easy to miss your peak with the higher resolution triple-axis optics. Once optimized for the lower resolution optics, repeat the steps for the higher resolution triple-axis optics for optimal results.

For lattice parameter and strain measurements absolute angles have to be known. In order to obtain correct angular readings you have to eliminate the relative tilt between the set of planes in the sample under observation (must be symmetric) and the wafer stage mounting normal. For measurement of asymmetric planes the sample has to be calibrated with a symmetric set of planes.

1. Follow all the steps described in C.3.3.1.
2. Take a set of four measurements 90 deg apart in ϕ . Each time optimize the intensity with changes in ω and $\omega/2\theta$ only. Note the angles for each scan.
3. The arithmetic average of the four angles ω is the absolute Bragg angle (To get both the in plane and perpendicular lattice parameter an asymmetric scan has to be performed).

To make a scan showing the correct angles find the minimum and maximum ω scan angles while changing ϕ . Once found the ideal setup is 90 deg away (in ϕ) from either maximum or minimum.

C.3.4 BASIC SAMPLE CHARACTERIZATION SCANS

C.3.4.1 WAFER MAP. The first scan done should be the wafer map scan. It reveals at a glance 'good' and 'bad' quality areas on a wafer. It consists of a set of 81 fast ω scans with different x-y coordinates spread in a square covering the wafer.

1. Optimize the setup as described under 3.3.1 for the center of the wafer.
2. Run the batch WAFERMAP under DATA COLLECTION/DATA COLLECTION PROGRAMS (this will take <2 hrs)

3. Use the MS Powerpoint form 'Wafer Map' to note all 81 FWHM's measured. Load every file and process it under PATTERN TREATMENT in the PC-MRD software. Start at the top left (scan 1) and finish at the bottom right (scan 81) (the process is not automated yet).
4. Copy the numbers of the 2D number matrix into an ASCII file (yes, by hand) and create a contour plot from that file with Easyplot 2. Then print your plot with Easyplot 3 (better colors, but messes up contour graphs while creating them).

C.3.4.2 ω and $\omega/2\theta$ SCANS. The second scan will make a 'close up' of an interesting spot revealed by the wafer map including the z-axis plane spacing given by the $\omega/2\theta$ scan.

1. Identify a spot on the Wafer you want to have a closer look at (e.g. lowest FWHM).
2. Move the wafer stage to its x-y coordinates. Optimize your signal following the steps in 3.3.1 using triple axis optics.
3. Run the PC-MRD batch called GANSTD. It will take a 15min ω scan and a 20min $\omega/2\theta$ scan.
4. Get the FWHM's from PATTERN TREATMENT/SINGLE SCAN and note them in the MS Excel file Ganrfsum.xls.

You finished the standard scans for single layer sample XRD characterization.

C.3.5 RECIPROCAL SPACE MAPS

For some sample configurations (e.g. GaN on ZnO, superlattices) reciprocal space maps reveal important material properties (strain, mosaicity). No standard batch file can be used. Settings vary too much from one sample to the other. Reciprocal space map scans consume a considerable amount of time. For superlattices scans 'over the

weekend' are nothing out of the ordinary. Since this puts a strain on the machine as well as the operator, preparation counts double. Here are a couple of useful guidelines:

1. Have a pocket calculator ready.
2. Optimize the triple axis optics on your main peak following the steps in C.3.3.1.
3. Know which peaks you need to see and which ones you do not need to see. From this calculate the maximum ω and $\omega/2\theta$ step width (broad peaks - wide steps) and minimum time per step (high intensity - small amount of time; think about your signal to noise ratio).
4. Minimize the scan area. Put the starting point of the scan in the center of your region of interest. This may not be the main peak. Take a fast scan, choose your new center point and under GRAPHICS/AREA SCANS in the PC-MRD software measure the angular distance of the new point to the main peak. Add/subtract the respective differences for ω and $\omega/2\theta$ manually and put the new angles in under DATA COLLECTION/MANUAL MEASUREMENTS and hit F1.
5. Set up an area scan file (manipulate one of the various G-xxxx scan files under EDIT MEASUREMENT PROGRAMS/SCAN FILES).
6. Start the scan and check regularly on the machine (cooling, computer crash etc.). Experience shows it is not advisable to run PS-MRD under MS Windows for long scans. Use Linux DOSemu in order to provide access to other data during the scan.

The above are only pointers. Your mileage may vary.

C.3.6 TILT MEASUREMENT

If you want to know the relative angle between epilayer and substrate you have to do a tilt measurement. Follow the steps in C.3.3.1. and C.3.3.2. to optimize the sample

position for the substrate. Now you have a set of four Bragg angles. Repeat the same procedure for the epilayer. Fill in all eight measured angles in the MS Excel worksheet named TILT.XLS - You will find details about the calculation there.

C.4 PROCESSING SCAN DATA

C.4.1 TWO DIMENSIONAL DATA

When doing a ω or $\omega/2\theta$ scan 2D data is created (angle(deg), intensity(cps)). This data may be exported via the UTILITIES/CONVERT FILES/MRD TO ASCII menu option in the PC-MRD software. The created files are not easily readable. To convert them into 2 column data use the Linux program

```
mrd2ep original.ascii.file 2column.ascii.file
```

Now the data is readable by Easyplot, Sigmaplot, Origin, Mathematica and other software and therefore easily processed. Further details on how to use mrd2ep are found in the respective Linux man-page.

C.4.2 THREE DIMENSIONAL DATA

In order to process reciprocal map scans (angle:angle:intensity) a similar conversion as for two dimensional data has to be performed. Export the scan via UTILITIES/CONVERT FILES/MRD TO ASCII menu option in the PC-MRD software. To convert the data into 3 column files use the Linux program

```
mrd3D original.ascii.file 2column.ascii.file
```

Now the data is readable by Easyplot, Sigmaplot, Origin, Mathematica and other software and therefore easily processed. Further details on how to use mrd3D are found in the respective Linux man-page.

VITA

FRITZ FEDLER

Candidate for the Degree of

Master of Science

Thesis: X-RAY DIFFRACTION STUDIES OF GaN AND InGaN SEMICONDUCTOR HETEROSTRUCTURES

Major Field: Physics

Biographical:

Personal Data: Born in Nienburg, Niedersachsen, Germany, on October 1, 1971, the son of Fritz and Anita Fedler.

Education: Graduated from *Gymnasium Hindenburgschule*, Nienburg, Germany in May 1991; received promotion to *Leutnant d.R.* after 2 years of service in the *Bundeswehr* in July 1994, received the *Vordiplom* in Physics from the *Universität Hannover*, Hannover, Germany in May 1995. Completed the requirements for the Master of Science degree with a major in Physics at Oklahoma State University in December 1998.

Professional Memberships: American Physical Society, Society of Physics Students.